Comparison and Investigation of Solar Spectral Irradiance with Solar Aspect Monitor

(Cissi) Ying-tsen Lin

Dissertation submitted to the faculty of the Virginia Polytechnic Institute and State University in partial fulfillment of the requirements for the degree of

Doctor of Philosophy

in

Electrical Engineering

Scott M. Bailey

Gregory D. Earle

Michael S. Hsiao

Kenneth R. Minschwaner

Wayne A. Scales

August 21, 2014

Blacksburg, Virginia

Keywords: solar irradiance, soft X-ray, image processing, nitric oxide, thermosphere

Comparison and Investigation of Solar Spectral Irradiance with Solar Aspect Monitor

(Cissi) Ying-tsen Lin

ABSTRACT

On-board the International Space Station (ISS), the Remote Atmospheric and Ionospheric Detection System (RAIDS) is a suite of limb-scanning monitors taking measurements from the extreme ultraviolet (EUV) to the near infrared (NIR). A single-scattering Rayleigh model is developed to eliminate the scattered brightness below 90 km and an inversion technique is applied on limb-scanned radiance profiles at 236.5 nm, NO (0,1) gamma band. The ISS orbit allows observations from 7:00 to 16:00 local hours over a one-month period from mid-June to mid-July of 2010 and observation of the local-time variation of NO abundance in the lower thermosphere is derived. The uniquely stable solar activity during 2010 allows the local time variation of NO to be observed with limited influence of solar variability. The comparison with a 1D model shows good agreement at altitude above 120 km, suggesting that most of the local time variation of NO is due to solar illumination, radiation, chemistry, and vertical diffusion.

Solar soft X-ray is the major driver of the variability observed in the ionospheric and thermospheric constituents at the equatorial region. Over the years measurements in these wavelengths are scarce and discrepancies lie among the existing data. The Solar Aspect Monitor (SAM) is a pinhole camera on the Extreme-ultraviolet Variability Experiment (EVE) flying on the Solar Dynamics Observatory (SDO). Every 10 seconds SAM projects the solar disk onto the CCD through a metallic filter designed to allow only solar photons shortward of 7 nm to pass. Contamination from energetic particles and out-of-band irradiance is, however, present. The broadband (BB) technique is developed for isolating the 0.1 to 7 nm integrated irradiance to produce broadband irradiance. The results agree with the zeroth-order product from the EUV SpectroPhotometer (ESP) with 25% regardless of solar activity level. Active regions in the solar atmosphere are tracked by the Apertural Progression Procedure for Light Estimate (APPLE). The photon event detection (PED) algorithm takes both BB and APPLE results as prior information to extract in-band photons. Applications of the PED products, including solar feature studies and spectral resolved irradiance, are demonstrated.

Acknowledgement

It would be impossible (improbable, if trying to make it sound scientifically correct) for me to name every one that I would like to give thanks to without missing any. However, quitting before trying is not what a scientist would do so here I go.

I would like to thank my adviser, Scott Bailey, who had been kind to me and invited me to his group activities since the first day I came to Virginia Tech way before I joined the group. He warmly open his arms to me taking me in when I needed to redirect my research after two years into my PhD career. Thank you, Scott, for questioning my ideas, being willing to accept different opinions, and embracing my wrongs. It is a graduate student's dream to have such an encouraging adviser and I was very lucky to have a mentor like you.

It would not be easy to come to this page if I do not have a supportive committee. I would like to thank Ken Minschwaner from New Mexico Tech, who I started working with in my first year into the RAIDS project and offered to serve in my committee. To this day, I still remembered the New Mexico Piñon coffee you brought to the RAIDS meeting on the 4th floor in Whittemore and the fun trip in Albuquerque. Wayne Scales, thank you for offering your help when I needed advice with my career directions. Greg Earle, your uplifting spirit has been a good example to me. Michael Hsiao – a teacher, friend, and loving brother to me – agreed to jump in as an out-of-field member when I needed to change my committee for the second time. I will miss your guitar lessons. Brent Ledvina, had it not been for the transition, I would not have found the beautiful space out there.

Thanks to the RAIDS and the SDO/EVE teams for the research opportunities. I have benefited a lot from all the meetings. Great friendship was built. As a student, I was inspired, encouraged, yet treated equally. I am also thankful for all the travel funding I have received to go around the world presenting my research.

I would like to thank my family. If not for their love, I would not make it to this stage of my life. Mom, I could never be able to imagine life without you. Thank you for being there for me every time an important decision is being made. Thank you for letting me fall down on my own so I would learn. Thank you for being the most delightful person in my life. You are the perfect person to road trip with! Dad, thanks for driving me to school every day growing up. Yu-hsien (仙兒), my baby sister, you are the best musician to me – so talented to a point that you did not grow up locking yourself to the practice room but still excellent as the way you are!

Thanks to all my moms in Blacksburg: Nizhou Han, Hinghar Lo, Melody Bizzell, Tammy Oliver, Tish Glosh, Kay Luttrell, Linda Olin… No one can be as blessed as me to have so much love from so many people who care for and pray for me. You are all in my mind and I may have to copy and paste the entire church directory here (and that would likely be as thick as my dissertation) so that I do not miss anyone. Thanks to Blacksburg Baptist Church, providing such a warm spiritual family. Thanks to all the smiley faces and positive energy that I got to experience all these years.

I could be one of the luckiest persons in the world to have a fun research group at Space@VT. There are times when we joked about the confusing situation to have two Justin and

two Alireza in the group. Every once in a while, I savor the fun we had on the canoe trips, game nights, cookouts… as a group. Justin 'Tintin' Carstens, who I sometimes shared fries with when I just got to VT, has been a good chatting target when I got stuck in some idea and needed to take my mind off for a little while. Justin Yonker, thank you for your enthusiasm to science and NO chemistry. Brentha Thurairajah, I enjoyed our girls' time together. Padma 'Padme' Thirukovoruri, how could you change your last name after I finally got to correctly pronounce your old one? Karthik Venkataramani, the atomic chats were always fun. Thank you all for training me to be brave enough to carry on my next attempts for long last names. Thanks to Heather Hunter for being a good friend to me. As if it were just yesterday, I vividly remember that selfie we took in the hallway on the 6th floor, not the prettiest but still the best. Haiyang 'Yangyang' Fu, it had been fun to share your ups and downs. Hyomin 'Oppa' Kim, the break-time Korean lessons were fun. Thanks to my Japanese teacher, Yasuko Kumazawa, and my French teacher, Francoise Mizutani. The language classes had freshened my school days. Katie Harris, even though we missed each other the first time because you gave me the wrong number, we still managed to become good friends and had so much fun together whether on the land, in the water, or in the air.

Thanks to my teachers and friends back at home in Taiwan. Thank you, Jenny Ou (小歐), for being an old-time friend and the dearest older sister to me and for believing in me. Without any complaint or asking for returns, you read and corrected the probably-not-so-fun English essays I wrote. Thanks to Ching-Yi Tsai (老大) for the geeky days and nights doing rocky science together and for your coat when it was cold and I did not care to carry one with me. Joy Sun for your inspiration and postcards from all over Japan. Thanks to the 314ers: Lwin, Waha, Birdcan, Fthil,

and Monica. I could not be me today without your friendship – understanding, loving, as well as teasing.

My only wish is to come before each one of you, look into your eyes, and deliver my gratitude with a long hug. Too many that I can possibly name in a limited human way so I would like to simply give thanks to our amazing God who provides and loves me all the time.

Table of Contents

List of Figures

List of Tables

Table of Acronyms Referred Frequently in the Dissertation

APPLE – Apertural Progression Procedure for Light Estimate

BB – broadband

ESP – EUV SpectroPhotometer

EUV – extreme ultraviolet

EVE – Extreme ultraviolet Variability Experiment

FUV – far ultraviolet

ISS – International Space Station

MEGS-A – Multiple EUV Grating Spectrograph A

MUV – Middle Ultraviolet

NB – narrowband

NO – nitric oxide

PED – photon event detection

RAIDS – Remote Atmospheric and Ionospheric Detection System

SAM – Solar Aspect Monitor

XUV – X-ray ultraviolet

1 INTRODUCTION

Over the past few decades, space shuttles, satellites, and rockets have been launched into space for various interests and application: climatology, plasma physics, biology, satellite positioning, and communication. One of the many reasons is simply out of pure curiosity from humanity. Today, commercial space vehicles are being developed in the hope of carrying their customers into space [Ryabinkin 2004]. However, space is not empty. Neutral and ionized gases exist thousands of kilometers above the surface of Earth. Their existence protects us from fatal cosmic rays but these gases also react to the input energy and directly impact the terrestrial life. Often severe space weather is caused by the active Sun. How do activities on solar atmosphere impact our daily life given that the Sun is 3×10^{17} km away? The thermal expansion or shrinking of the atmosphere, as a result of ambient temperature varying with solar cycle, results in different levels of satellite drag, whose magnitude is proportional to the neutral gas density [Emmert et al., 2010]. During solar flares, the Sun releases intensive energy in all wavelengths. Solar radio burst has been observed to impact the performance of ground GPS receivers and result in potential failure [Cerruti et al., 2006; Kintner et al., 2007]. The strong induced ground current during geomagnetic storm has destroyed power grids and caused large blackouts [Kappenman, 2005]. Aviation safety also relies on GPS and high-frequency (HF) communication over the polar region. As our life started depending on technical infrastructures in space, space weather has become a critical subject of study. The growth of space technology has led to a series of space weather studies as we try to understand the mechanism of the entire Sun-Earth system. The Sun-Earth system is not a simple subject. It requires a great number of researchers from various disciplines to work together. Hand in hand, step by step, scientists from different disciplines, such as heliophysics,

plasma physics, atmospheric science, dynamics, and aeronomy continuously develop models and carry out experiments trying to explain the phenomenon we see.

Based on the temperature structure from the Earth surface to space, neutral atmosphere is categorized into troposphere, stratosphere, mesosphere, thermosphere, and exosphere. Above the mesopause (~ 85 km), gas species are ionized by very energetic solar photons or charged particles and form the ionosphere, above which lie plasmasphere and magnetosphere. Coexisting at similar altitudes are the ionosphere and thermosphere, where the most violent solar energy gets absorbed. As a result, temperature increases dramatically from the bottom to the top of the thermosphere. Among all the species in the ionosphere/thermosphere system, nitric oxide (NO) plays numerous key roles in the lower thermosphere though being a minor constituent. Its production is very sensitive to those energy sources able to break the strong bond of molecular nitrogen and its concentrations are indicative of energy deposition. Cooling through infrared emission at 5.3 μm, NO is a crucial part of the thermospheric energy balance. Given that NO has the lowest ionization potential in the chemical reaction chain, NO^+ is the terminal ion and dominates the electron density in the E-region of the ionosphere where most of its production is by solar soft X-ray and extreme ultraviolet (EUV) radiation. It is also present in the D-region where its production is by much longer wavelength solar photons, weak but high-flux, of hydrogen Lyman α emission line at 122 nm. As all of the constituents in the atmosphere, the abundance of NO is determined when the production and loss mechanisms reach steady-state equilibrium. If no transport is considered, the continuity equation can be written as simple competition between production, P, and loss, L.

$$\frac{dn}{dt} = P - L \tag{1.1}$$

where P and L are results of many chemical reactions and will be further discussed in Chapter 2. These reactions are functions of gas density, ambient temperature, and solar radiation. Therefore, variation of the NO presence reflects that of the energy input to the atmosphere, including solar radiation and participation of energetic particles. Consequently, solar signatures, such as 11-year cycles, 27-day rotation, and even as short as flares, can be observed in the NO density.

The important role solar soft X-ray irradiance plays in the NO production was recognized in the late 1980s [Barth, et al., 1988]. To explain the coupling between solar activity and the NO density at 110 km, it was hypothesized that solar soft X-ray photons between 20 and 100 Å, which are absorbed at this altitude, is the cause of the NO variation. Figure 1.1 shows that solar radiation at wavelengths shortward of 20 nm and longward of 80 nm is mostly absorbed at the altitudes between 100 to 150 km. Using one-dimensional NO model, Siskind et al. [1990] suggested that a soft X-ray flux fifty times higher than the value provided by the solar spectrum reference model, SC21REFW, for solar minimum condition is needed to better agree with their sounding rocket observation. The suggested higher solar soft X-ray flux increases the ionization of molecular nitrogen. This idea was later supported by a time-dependent thermospheric model which proved that solar soft X-ray is the main driver for the variation of NO density at the equator [Bailey et al., 2002]. In his dissertation, Yonker [2013] showed photoelectron ionization rate of molecular nitrogen, which is the main driver of NO production, at the lower thermosphere is primarily dominated by short-wavelength photons with energy greater than 10 keV. On the other hand, at the polar region, the effect of solar photons is not as strong as energetic particle participation, especially during strong geomagnetic activities. At the polar region, descent of NOx (NO and NO_2) has been observed. The enhancement of NO abundance due to Joule heating has been observed

diffusing to the lower altitudes [Barth et al., 2009, 2010]. After stratospheric sudden warming (SSW) events, the NO enhancement at the lower altitudes is unusually strong during vortex recovery [Randall et al., 2009]. If NO is transported to the lower altitudes, it is a catalytic destroyer of ozone [Solomon et al., 1982].

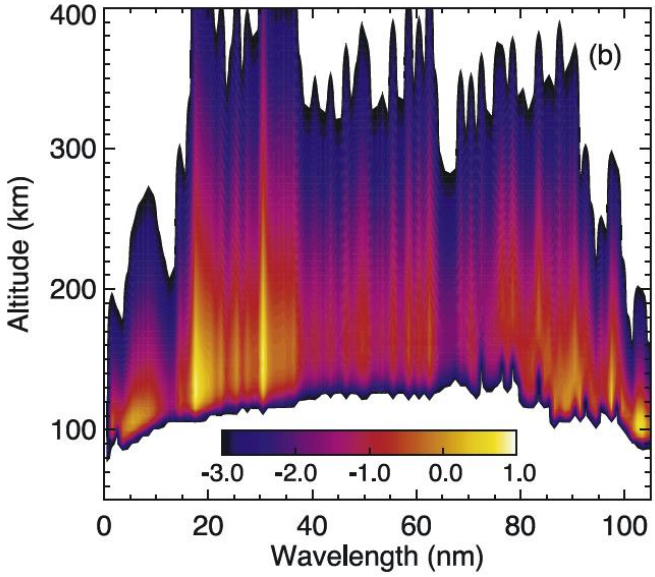

Figure 1.1. Deposition of solar EUV energy in the thermosphere [Solomon et al., 2005].

The history of solar soft X-ray observation can be traced back to the l960s. Sounding rocket measurements opened a page to several satellite-based experiments, including SOLRAD, Orbiting Solar Observatory (OSO) [Hall and Hinteregger, 1970; Hall, 1971], the Atmospheric Explorer (AE) satellites [Gibson and Van Allen, 1970], SkyLab (1973 – 1979) [Vaiana et al., 1976], and Solar Maximum Monitor (SMM) (1980) [Acton et al., 1980; Bohlin et al., 1980]. The Soft X-ray Telescope (SXT) on Yohkoh took full-disk images of the Sun between 0.2–3 nm from 1992 to 2005 [Ogawara et al., 1992]. Soft X-ray irradiance can be estimated with an isothermal spectral model and modeled by means of differential emission measure (DEM) [Acton et al., 1999]. The

Solar soft X-ray Photometer (SXP) on the Student Nitric Oxide Explorer (SNOE) had several broadband channels making daily measurement of solar soft X-ray with bandpasses of 2–7 nm, 6–19 nm, and 17–20 nm [Bailey et al., 1999, 2006]. Solar Extreme ultraviolet Monitor (SEM) on the SOlar and Heliospheric Observatory (SOHO) has continuously measured the solar EUV irradiance since 1996 [Judge et al., 1998; Ogawa et al., 1998]. Its zeroth-order channel monitors the full-disk solar irradiance from 0.1 to 50 nm, and has a first-order channel measuring the He II 30.4 nm irradiance. The NOAA Geostationary Operational Environmental Satellite (GOES) series satellites carry X-Ray Sensor (XRS), measuring X-ray flux at 0.05–4 nm and 0.1–0.8 nm. The Solar EUV Experiment (SEE) onboard the Thermosphere, Ionosphere, and Mesosphere Energetics and Dynamics (TIMED) satellite carries the XUV Photometer System (XPS) and the EUV Grating Spectrograph (EGS) to provide daily irradiance of XUV between 0.1 and 35 nm and EUV between 25 and 200 nm [Woods et al., 1999]. The Solar Radiation and Climate Experiment (SORCE) XPS [Woods et al., 2008] is essentially identical to the one on TIMED/SEE. The X-Ray Telescope (XRT) on Hinode started taking X-ray images since 2006 [Golub et al., 2007; Kano et al., 2007]. Woods et al. [2004] gave a detailed historical account of the spaceborne measurements of solar EUV and soft X-ray irradiance. To this date discrepancies still lie among all the soft X-ray data sets and models [Solomon et al., 2005]. Theoretical and empirical reference models [Tobiska et al., 2010; Warren, 2005; Richards et al., 2006; Chamberlin et al., 2007, 2008] of the solar spectrum are therefore established to better assist climate models when measurements are not available; however, comparison of modeled atmospheric response using solar measurements with available atmospheric data has shown that the soft X-ray may be underestimated in the solar reference models and needs to be scaled by a factor of 2 or more [Bailey et al., 2002]. This uncertainty is

verified in studies of ion and electron densities for which are created in proportion to the solar ionizing irradiance [Solomon et al., 2006].

Launched in 2010, Solar Dynamics Observatory (SDO) is the first mission of NASA's Living With a Star (LWS) program. The goal of the SDO mission is to understand the solar variability and its impact to the terrestrial technology and society. SDO facilitates not only better knowledge of heliophysics through studying the evolution of solar magnetic fields and its atmosphere but also the connection from solar activities to the life on Earth. The Extreme ultraviolet Variability Experiment (EVE), conducted by the Laboratory for Atmospheric and Space Physics (LASP), is one of the three instruments on SDO [Hock et al, 2010; Woods et al., 2010]. EVE observes the region of solar spectrum which heavily drives the variability of the Earth's upper atmosphere: the extreme ultraviolet (EUV) and the soft X-ray. The Solar Aspect Monitor (SAM) is a pinhole camera on EVE. Its bandpass filter is designed to allow photons shortward of 7 nm (energy above 180 eV) to be detected. Though SAM is a spare channel, efforts have been put in to use its images to resolve solar spectral irradiance, which is the main scope of the second half of this study. Details of the SAM instrument are discussed in Chapter 3. The EUV SpectroPhotometer (ESP) on EVE, developed at University of South California, is an expanded version of SOHO/SEM. It is a non-focusing broadband spectrograph. Its quad-diode (QD) channel produces main datasets of broadband soft X-ray irradiance measurements for the EVE science goal [Didkovsky et al., 2009]. In this study, broadband irradiance in soft X-ray wavelengths is obtained from the SAM images and compared with the ESP zeroth-order QD product.

In this dissertation, Chapter 2 focuses on the remote sensing results of NO in the lower thermosphere. Data reduction, processing, and analysis are performed on the level 0 data of the NO emission line at 237 nm from a limb viewing geometry by the Remote Atmospheric and Ionosperic Detection System (RAIDS). This experiment was conducted by the Naval Research Laboratory (NRL). The retrieval procedure is developed and the derived local-time variation of the NO density is further compared with the 1D thermospheric NO model, NOx1D. Chapter 3 introduces the techniques developed to obtain solar soft X-ray broadband (BB) irradiance from the contaminated level 0b solar images taken by SAM. The validation is performed against the ESP measurements and the agreement within 25% is obtained regardless solar activity levels. Further in Chapter 4, the Apertural Progression Procedure for Light Estimate (APPLE) studies strength of active regions via tracking locations and brightness on the charge-coupled detector (CCD). The BB and APPLE results facilitate the photon-event detection (PED) algorithm, with which photon events are extracted from the raw images and available for application toward spectral irradiance and solar feature studies.

References

Acton, L. W., J. L., Culhane, A. H. Gabriel, R. D. Bentley, J. A. Bowles, J. G. Firth, M. L. Finch, C. W. Gilbreth, P. Guttridge, R. W. Hayes, E. G. Joki, B. B. Jones, B. J. Kent, J. W. Leibacher, R. A. Nobles, T. J. Patrick, K. J. H. Phillips, C. G. Rapley, P. H. Sheather, J. C. Sherman, J. P. Stark, L. A. Springer, R. F. Turner, and C. J. Wolfson, "The soft X-ray polychromator for the Solar Maximum Mission," Solar Physics, 1980

Acton, L. W., D. C. Weston, M. E. Bruner, "Deriving solar X-ray irradiance from Yohkoh observations," Journal of Geophysical Research, 104, 1999

Bailey, S. M., T. N. Woods, C. A. Barth, and S. C. Solomon, "Measurements of the solar soft x-ray irradiance from the Student Nitric Oxide Explorer," Geophysical Research Letters, 26, 9, 1999

Bailey, S. M., C. A. Barth, and S. C. Solomon, "A model of nitric oxide in the lower thermosphere," J. Geophys. Res., 107(A8), doi:10.1029/2001JA000258, 2002.

Bailey S. M., T. N. Woods, F. G. Eparvier, and S. C. Solomon, "Observations of the solar soft X-ray irradiance by the student nitric oxide explorer," Advance in Space Res., 37, 2006

Barth, C. A., W. K. Tobiska, D. E. Siskind, and D. D. Cleary, "Solar-terrestrial coupling: low-latitude thermospheric nitric oxide," Geophysical Research Letters, Vol. 15, 1988

Barth, C. A., et al., Joule heating and nitric oxide in the thermosphere, *J. Geophys. Res.*, 114, A05301, doi:10.1029/2008JA013765, 2009

Barth, C. A., Joule heating and nitric oxide in the thermosphere, 2, *J. Geophys. Res.*, 115, A10305, doi:10.1029/2010JA015565, 2010

Bohlin, J. D., K. J. Frost, P. T. Burr, A. K. Guha, G. L. Withbroe, "Solar Maximum Mission," Solar Physics, 1980

Cerruti, A. P., P. M. Kintner, D. E. Gary, L. J. Lanzerotti, E. R. de Paula, and H. B. Vo, "Observed solar radio burst effects on GPS/Wide Area Augmentation System carrier-to-noise ratio," Space Weather, Vol. 4, 2006

Emmert, J. T., J. L. Lean, and J. M. Picone, "Record-low thermospheric density during the 2008 solar minimum," Geophysical Research Letters, Vol. 37, 2010

Gibson, S. J. and J. A. Van Allen, "correlation of X-ray radiation (2-12 A) with microwave radiation (10.7 centimeters) from the nonflaring Sun," Astrophysical Journal, 161, 1970

Hall L. A. and H. E. Hinteregger, "Solar radiation in the EUV and its variation with solar rotation," Journal of Geophysical Research, 75, 1970

Hall, L. A., "Solar flares in the extreme ultraviolet," Solar Physics, 21, 1971

Judge, D. L., D. R. McMullin, H. S. Ogawa, D. Hovestadt, B. Klecker, and M. Hilchenbach, "First solar EUV irradiance obtained from SOHO by the CELIAS/SEM," Solar Phys., 177, 1998

Kano, R., T. Sakao, H. Hara, S. Tsuneta, K. Matsuzaki, K. Kumagai, M. Shimojo, K. Minesugi, K. Shibasaki, E. E. DeLuca, L. Golub, J. Bookbinder, D. Caldwell, P. Cheimets, J. Cirtain, E. Dennis, T. Kent, and M. Weber, "The Hinode X-Ray Telescope (XRT): Camera design, performance and operations," Solar Phys., 249, 2008

Kappenman, J. G. "An overview of the impulsive geomagnetic field disturbances and power grid impacts associated with the violent Sun-Earth connection events of 29-31 October 2003 and a comparative evaluation with other contemporary storms," Space Weather, Vol. 3, 2005

Kintner, P. M, B. M. Ledvina, and E. R. de Paula, "GPS and ionospheric scintillations," Space Weather, Vol. 5, 2007

Ogawa, H. S., D. L. Judge, D. R. McMullin, P. Gangopadhyay, and A. B. Galvin, "First-year continuous solar EUV irradiance from SOHO by the CELIAS/SEM during 1996 solar minimum," J. of Geophysical Research, Vol. 103, 1998

Randall C. E., V. L. Harvey, D. E. Siskind, J. France, P. F. Bernath, C. D. Boone, and K. A. Walker, "NOx descent in the Arctic middle atmosphere in early 2009," Geophysical Research Letters, Vol. 36, 2009

Ryabinkin, C. T., "Let there be flight: It's time to reform the regulation of commercial space travel," Journal of Air Law and Commerce, 2004

Siskind, D. E. et al., "The Possible Effect of Solar X-Rays on Thermospheric Nitric Oxide," Journal of Geophysical Research, Vol. 95, 1990

Solomon S., P. J. Crutzen, and R. G. Roble, "Photochemical coupling between the thermosphere and the lower atmosphere 1. Odd nitrogen from 50 to 120 km," Journal of Geophysical Research, 87, 1982

Vaiana, G. S. et al., "ATM observations, X-ray results," Astrophysics and Space Science, 39, 1976

Woods, T. N., G. J. Rottman, S. M. Bailey, S. C. Solomon, J. R. Worden, "Solar extreme ultraviolet irradiance measurements during solar cycle 22," Solar Physics, 1998

Woods, T. N., E. Rodgers, S. M. Bailey, F. G. Eparvier, and G. Ucker, "TIMED Solar EUV Experiment: pre-flight calibration results for the XUV Photometer System," SPIE, 3756, 1999

Woods, T. N., L. W. Acton, S. B. Bailey, F. Eparvier, H. Garcia, D. Judge, J. Lean, J. T. Mariska, D. McMullin, G. Schimidtke, S. C. Solomon, W. K. Tobiska, H. P. Warren, and R. Viereck, "Solar Extreme Ultraviolet and X-ray Irradiance Variations," Solar Variability and its Effects on Climate, Geophysical Monograph 141, AGU, 2004

Woods, T. N., P. C. Chamberlin, W. K. Peterson, R. R. Meier, P. G. Richards, D. J. Strickland, G. Lu, L. Qian, S. C. Solomon, B. A. Iijima, A. J. Mannucci, B. T. Tsurutani, "XUV Photometer System (XPS): Improved solar irradiance algorithm using CHIANTI spectral models," Solar Physics, 2008

Yonker, J. D., "Contribution of the First Electronically Excited State of Molecular Nitrogen to Thermospheric Nitric Oxide," PhD dissertation, 2013

CHAPTER 2 Observation of the Local-Time Variation of Nitric Oxide Abundance in the Equatorial Lower Thermosphere by the Remote Atmospheric and Ionospheric Detection System

Abstract

Observation of the local-time variation of nitric oxide (NO) abundance in the lower thermosphere is accomplished by the Remote Atmospheric and Ionospheric Detection System (RAIDS). On-board the International Space Station (ISS), RAIDS is a suite of limb-scanning monitors taking measurements from the extreme ultraviolet (EUV) to the near infrared (NIR). A single-scattering Rayleigh model is developed to eliminate the scattered brightness below 90 km and an inversion technique is applied on limb-scanned radiance profiles at 236.5 nm, NO (0,1) gamma band. The ISS orbit allows observations from 7:00 to 16:00 local hours over a one-month period. The uniquely stable solar activity during 2010 allows the local time variation of NO to be observed with limited influence of solar variability. The comparison with a 1D model shows good agreement at altitude above 120 km, suggesting that most of the local time variation of NO is due to solar illumination, radiation, chemistry, and vertical diffusion.

Keywords: nitric oxide, thermosphere, local-time variation, NOx1D

2.1 Introduction

NO plays numerous key roles in the lower thermosphere though being a minor constituent there. Its production is very sensitive to those energy sources able to break the strong bond of molecular nitrogen and its concentrations are indicative of energy deposition, such as energetic particle precipitation [Baker et al., 2001; Barth et al., 2001] and solar soft X-ray [Barth et al., 1988; 1999; 2003; Barth and Bailey, 2004; Siskind et al., 1990]. Cooling through infrared emission at 5.3 μm [Mlynczak et al., 2003], NO is a crucial part of the thermospheric energy balance. Given that NO has the lowest ionization potential in the chemical reaction chain, NO^+ is the terminal ion and dominates the electron density in the E-region of the ionosphere. If NO is transported to lower altitudes, it is a catalytic destroyer of ozone [Crutzen, 1970; Solomon et al., 1982; Randall et al., 2009]. As all of the constituents in the atmosphere, the presence of NO and its abundance are determined when the production and loss mechanisms reach steady-state equilibrium. Its variation reflects that of the energy input into the atmosphere and shows the signature of 11-year solar cycles [Kumar et al., 1999], 27-day solar rotation [Barth et al., 1999], and as short as flares [Rodgers et al., 2010] and auroral participation that last only a few hours [Baker et al., 2001]. The effect of solar soft X-ray on thermospheric NO was first proposed by Siskind et al. [1990], whose work was later followed by a time-dependent thermospheric model which proved that solar soft X-ray is the main driver for the variation of NO density at the equator [Bailey et al., 2002]. It has been shown that photoelectron ionization rate of molecular nitrogen, which is the main driver of NO production, at the lower thermosphere is primarily dominated by short-wavelength photons with energy greater than 10 keV [Yonker, 2013].

In Section 2.2, we introduce the major processes leading to production and destruction of NO. A 1D model is later implemented for the comparison to the observation. The RAIDS mission is introduced in Section 2.3. Data reduction and handling are performed on the level 0 data to prepare data sets for retrieval. Viewing at lower altitudes, Rayleigh scattering is much brighter than the NO emission. A single-scattered Rayleigh model is developed in Section 2.4 to estimate the brightness observed below 80 km. The estimate of the uncertainties are discussed in Section 2.5. Derived from the retrieved NO profiles, the local-time variation of NO from the observation and the model at 120–150 km is presented in Section 2.6. Section 2.7 summarizes this study and states possible future projects.

2.2 Photochemistry of NO and Model NOx1D

The physics of NO production and loss has long been a topic of study [see Barth, 1992; Bailey et al., 2002, and references therein]. It is produced by the oxidation of atomic nitrogen.

$$N\left(\,^2D,\,^4S\right) + O_2 \rightarrow NO + O \qquad \text{(R2.1)}$$

Excited nitrogen, N(^{2}D), is the primary source of NO near the NO peak at around 106 km because the oxidation of ground-state nitrogen, N(^{4}S), is inefficient at the temperatures there near 300K, but this is no longer the case at higher altitudes where higher temperatures increase the rate of N(^{4}S) oxidation much more significantly than that of N(^{2}D). NO is primarily destroyed by the cannibalistic reaction (R2.2) and also the charge exchange with O_2^+ (R2.3).

$$NO + N\left(\,^4S\right) \rightarrow N_2 + O \qquad \text{(R2.2)}$$

$$NO + O_2^+ \rightarrow NO^+ + O_2 \qquad \text{(R2.3)}$$

A major source of N(^{4}S) is the photodissociation of NO itself by far ultraviolet (FUV) sunlight [Minschwaner and Siskind, 1993].

$$NO + h\nu \rightarrow N\left(\,^4S\right) + O \qquad \text{(R2.4)}$$

Ionization is a crucial process in the formation of NO. Ionization of NO by Lyman-α at 121.6 nm is a loss, but subsequent dissociative recombination of NO yields N(^{2}D) which ultimately leads to the reformation of NO (R2.5-2.6). As soon as N(^{2}D) is created, NO is created since the reaction R2.1 takes less than one second. Ultimately the key to understanding the production of NO is to understand the sources of atomic nitrogen and in particular N(^{2}D).

$$NO + h\nu \rightarrow NO^+ + e^- \qquad \text{(R2.5)}$$

$$NO^+ + e^- \rightarrow N\left(\,^2D\right) + O \qquad \text{(R2.6)}$$

The role of ionized N_2 by X-ray ultraviolet (XUV) photons or photoelectrons in the production and loss of NO has recently been emphasized [Yonker, 2013]. At the lower thermosphere, ionization of N_2 is important as the resultant N_2^+ can react with atomic oxygen, forming NO+ and N(^{2}D).

$$N_2^+(X) + O\left(\,^3P\right) \rightarrow NO^+\left(\,^1\Sigma^+\right) + N\left(\,^2D\right) \qquad \text{(R2.7)}$$

Dissociation of N_2 by electrons and photons is important, however since the resultant nitrogen atoms contribute to both production and loss of NO and while ionization of N_2 through R2.7 leads to the production of two NO molecules, ionization turns out to the more important process for producing NO. Figure 1.1 in Yonker's [2013] work summarizes the chain events of this complex NO photochemistry at 110 km at the equatorial noon on a typical day close to the maximum of solar cycle 22.

NOx1D is a one-dimensional time-dependent model that includes transport, neutral and ion photochemistry, and vertical eddy and molecular diffusion [Bailey et al., 2002]. Several key reaction rate coefficients were updated in this model from its previous versions. Using the GLOW model [Solomon et al., 1988; Solomon and Abreu, 1989] to calculate the photoelectron spectrum improved the model accuracy because no local approximation in photoelectron calculation had to be made. In their study, Bailey et al. [2002] took solar irradiance longward of 20 nm from the model of Hinteregger et al. [1981] and applied three different scaling factors to irradiance in 2 – 7 nm, 7 – 17 nm, and 17 – 20 nm of the same model. Measurements from the Solar soft X-ray Photometer (SXP) on the Student Nitric Oxide Explorer (SNOE) are used to determine these three scaling factors.

Yonker [2013] updated NO chemistry based on modern lab results into NOx1D and has significantly improved our understanding of the NO chemistry and in particular its relationship with energy inputs, such as the role of $N_2(A)$ in the NO reactions.

$$N_2(A) + O \rightarrow NO + N(\,^2D) \qquad \text{(R2.8)}$$

In his work, Yonker [2013] provides parameterization of the $N_2(A)$ production rates which can be further implemented in various atmospheric models to lower the computational expenses. In this paper, NOx1D is driven by the Extreme Ultra-Violet flux model for Aeronomical Calculations (EUVAC) solar spectrum, which has 37 wavelength bins of various ranges [Richards et al., 2006]. In each bin, the EUV flux is estimated by

$$f_i = f_{ref}[1 + A_i(P - 70)] \qquad (2.9)$$

where f_{ref} is the standard reference spectrum at solar minimum, A_i the scaling coefficient, and P the average of the daily and the 81-day mean of $F_{10.7}$.

As predicted by the model, NO abundance at its peak altitude (~110 km) is expected to first decrease in the early morning and then increase in several hours. After sunrise, the solar optically thin far ultraviolet (FUV) radiation penetrates to and is absorbed at the lower altitudes at large solar zenith angles and leads to photodissociation of NO (R2.5). Going toward noon, the decrease of solar zenith angle allows the optically thick soft X-ray irradiance to deposit at the lower altitude where it rapidly produces $N(^2D)$ and thus NO (R2.1). The production due to soft X-ray irradiance reaches its maximum from around local noon to 2 PM. As solar zenith angle starts increasing, the NO production and its abundance decreases in the afternoon. On the other hand, soft X-ray irradiance is absorbed as soon as the atmosphere is sunlit at higher altitudes (~150 km) so the increase in production of NO should be observed soon after sunrise.

2.3 Observations

SNOE observed lower thermospheric NO March 11, 1998 through November 5, 2003 and has proven the importance and dependence of solar soft X-ray irradiance and auroral activities to the production of NO with its measurements [Barth et al., 2003; Barth and Bailey, 2004]. SNOE was in a sun-synchronous orbit and therefore was only able to obtain NO densities near 11 AM local time.

RAIDS was developed to provide a comprehensive observation of the global thermosphere-ionosphere system. It was launched with Kibo Japanese Experiment Module (JEM-EF) to be onboard the ISS on September 10, 2009. After a period of on-orbit checkout and commissioning phase, RAIDS began routine observations on October 23. Carrying three

narrowband photometers, three scanning spectrometers and two imaging spectrographs, RAIDS is a suite of limb viewing radiance monitors observing the lower thermosphere at wavelengths from the extreme ultraviolet (EUV) through the near infrared (NIR). A detailed description of the orbital configuration and the instruments is provided by Budzien et al. [2009, 2011]. The middle-ultraviolet (MUV) spectrometer is an f/5 Ebert-Fastie scan-enabled grating monochromator that covers 190 – 317 nm at 1-nm resolution. It operates in two modes: 1) spectrum scanning at fixed tangential altitudes and 2) limb scanning at fixed wavelength. In this study, an inverse technique is applied to radiance profiles at 236.5 nm, the optically thin NO (0,1) emission, when the data is taken at fixed-wavelength mode so that the vertical distribution of NO can be established. Figure 1 in [Barth and Bailey, 2004] shows the modeled NO density varies with local time: increasing after sunrise owing to the solar X-ray illumination at 110 km and decreasing after sunset because of absence of the production source and downward transport. ISS orbits around the Earth 15.7 times a day at altitude of 355 km. Benefited by it, RAIDS was not only able to perform its scientific experiments globally but also is the first experiment for several decades that truly observed NO profiles at all daytime local hours. Thus, it observes the temperature driven diurnal and seasonal variations in NO. However, no limb-scanned observations could be further obtained since late Dec, 2010 due to a mechanic problem occurring on the rotating platform. Among all scientific observations over the period Jan 10, 2010 through Dec 14, 2010, limb-scanning at wavelength of 236.5 nm in the MUV operation mode shares about 100 days of the time (Figure 12 in Budzien et al.'s work [2011]). The brightness measured by the RAIDS limb-viewing mode is used to retrieve the NO vertical profile at different latitudes, local sunlit time, and solar zenith angles.

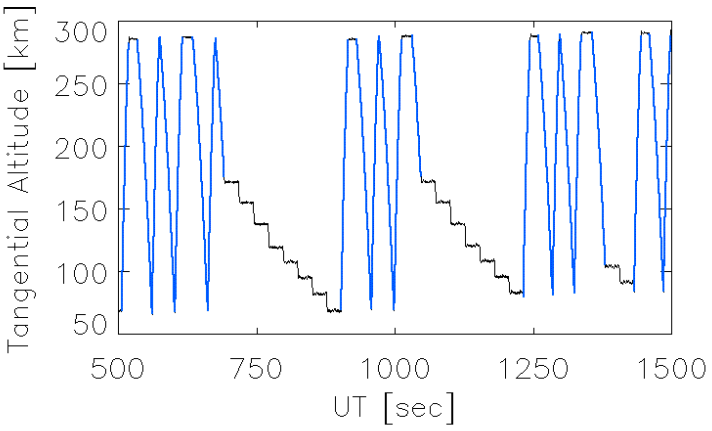

Figure 2.1. The MUV experiments are perform in limb-scanning (blue) and spectral (black) modes. Observed tangential altitudes show the regular yet different patterns of the mechanically rotating platform combined with the wobbling effect by ISS.

A software-controlled stepper motor drives the scan platform through a sequence of angles for different observation modes. Altitude of the tangential points scanned by RAIDS is determined not only by its own rotating platform but also by the ISS activities. The term, tangential altitude, is used throughout this paper and is defined as the altitude of the tangential point, where the line of sight is perpendicular to the local zenith and whose NO abundance contributes the most for the line-of-sight optically thin emission measurements. Any maneuver and astronauts' activity on ISS changes the ISS mass distribution and affect the viewing geometry of the observation. A small change in viewing angle at the ISS end could result in a several-kilometer difference in altitude at the tangential points. The ISS attitudes, the star tracker attitudes, and the RAIDS data have been carefully registered to address the causes of the pointing issue [Budzien et al., 2011]. Figure 2.1 shows that the wobbling of ISS is modulated onto the limb scans and shapes the envelope of tangential altitudes. On the other hand, due to the nature of the ISS orbit and the altitudes where the measurements are taken, the raw RAIDS limb-scanned measurements are taken with varying altitudinal spacing over a varying altitudinal range. Within a single scan the vertical spacing

between two measurement points could be as large as 6 km when the tangential altitude is at 100 km and 3 km at 300 km. In order to apply Abel inversion, which assumes the atmosphere consists of spherically symmetrical layers, the RAIDS measurements have to be re-binned onto a uniform grid for the retrieval. Additionally, since the spacecraft keeps moving during the scan, every measurement is kilometers away from its previous one. This means even temporally adjacent measurements are under different geophysical conditions, such as latitude, longitude, which implies local sunlit time, solar zenith angle and solar-input condition. Therefore, great care needs to be taken when re-binning the raw measurements. In this study, the data are binned into grids of 10° in latitude, one hour in sunlit local time, and 10° in solar zenith angle in order to keep geophysical condition similar enough in each retrieved profile and to preserve the information of a single retrieved vertical profile at a certain tangential location for possible future investigation.

2.4 Background Rayleigh-scattered Radiance

The intensity of the emission at 236.5 nm indicates the abundance of the NO along the line of sight and NO column density can be estimated with measured brightness counts by

$$n_{NO,col} = \frac{B\Delta\lambda_{hw}F_{ray}}{STg} \tag{2.10}$$

where B is the raw brightness counts, S the sensitivity of the spectrometer, $\Delta\lambda$ the full width of half maximum, F_{ray} the Rayleigh factor, T the integration period of 0.5 seconds per frame, and the g-factor estimates the number of emitted photons with the presence of NO. The sensitivity of 6 (count per second) / (Rayleighs per Angstrom) is measured and calibrated at 236.5 nm of the MUV spectrometer [Stephan et al., 2009; 2011]). The value of g-factor is taken as 2.25 x 10^6 photons per molecule per second [Barth et al., 2003] and F_{ray} is 10^6 photons per cm^2 per second per solid angle.

As shown in Figure 2.1, the lowest altitude of each RAIDS limb scan is around 70 – 90 km. The main scanning is performed by the RAIDS platform but slight variation of the upper and lower boundaries is due to the ISS onboard activities. This lower bound is in the upper mesosphere and the lower thermosphere. The dashed line in Figure 2.2 is a sample vertical profile of column densities converted from re-binned raw brightness observed by RAIDS. The brightness from the Rayleigh scattering obscures the NO measurements below 100 km and needs to be removed. Figure 2.3 shows a single-scattered Rayleigh model in the atmosphere with unit solar flux. The simulation uses the standard profiles of N_2, O_2 and O_3. Radiance of this type peaks at around 60 km with slight variation due to solar zenith angle and e-folds above the peak. The magnitude of brightness caused by Rayleigh scattering is several orders greater than that from NO. The assumption has been made that no brightness below 80 km comes from NO and all the brightness below such altitude are subtracted off by scaling the modeled Rayleigh curves accordingly. The dashed curve in Figure 2.2 is the corresponding column density profile if Rayleigh-scattered radiance were mistreated as NO emission and is the amount that needs to be subtracted from the pre-correction column density (dot). After correction, Abel transform is performed onto the resulting line-of-sight radiance (solid) for the volume density retrieval of NO.

However, in fact the limb radiance at 236.5 nm does not complete disappear even at tangential altitude below 70 km with the moderate amount of NO in the lower thermosphere. Figure 2 of the paper by Bailey et al. [2005] has demonstrated for radiance at 215 nm. By eliminating all brightness below 80 km we implicitly overestimate the Rayleigh scattering and underestimates the NO contribution to the column emission there. In Figure 2.2, the correction appears to lower the column density by 8% at around 100 km but does not cause much depletion

at the altitudes above 120 km due to the fact that the exponentially folding of the Rayleigh scattered radiance drops to 0.1% from 80 km to 120 km and 3.9% from 100 km to 120 km. Therefore, the NO abundance above 120 km retrieved from the RAIDS observation in this study represents closely to the real atmospheric conditions.

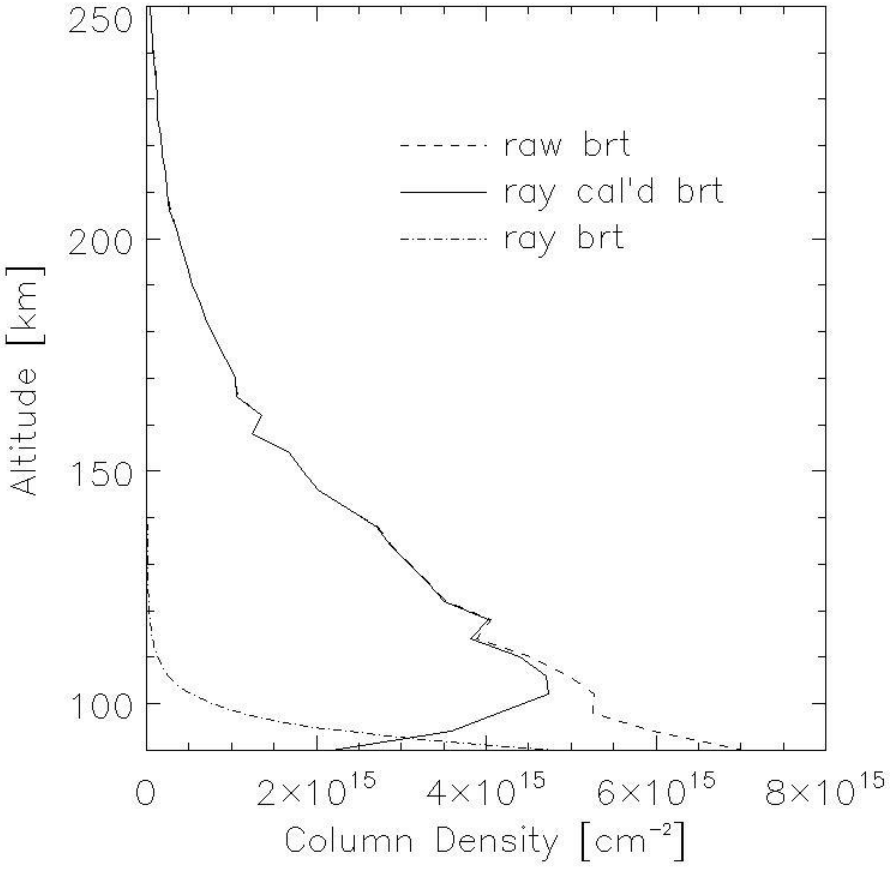

Figure 2.2. Vertical profile of NO column density (dash) converted from the raw brightness counts is overwhelmed by the Rayleigh-scattered radiance. The Rayleigh contribution is estimated (dash dot) and removed. Abel transform is performed onto the resulting vertical profile of line-of-sight radiance (solid) to retrieve volume density.

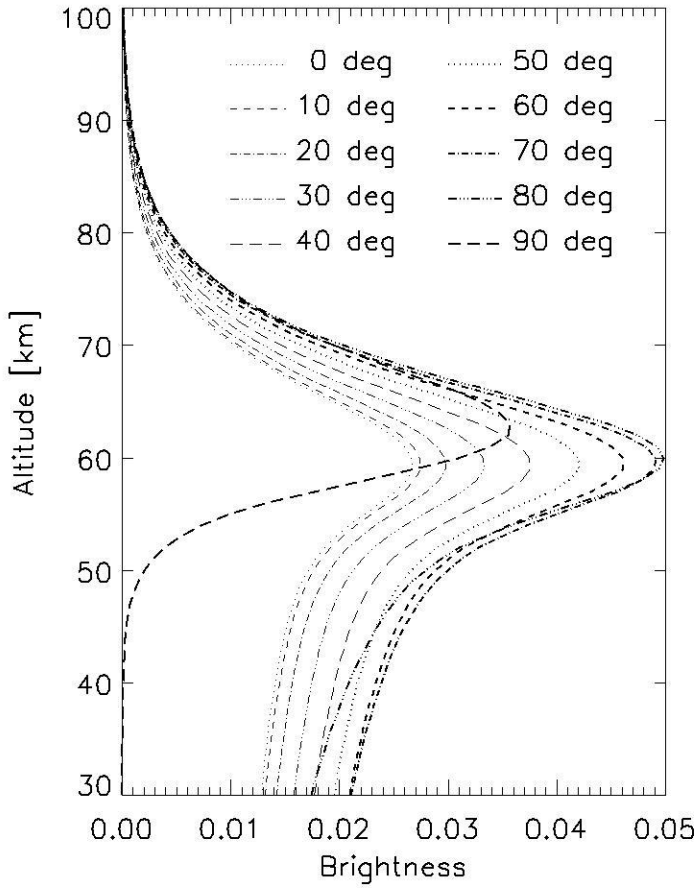

Figure 2.3. Modeled Rayleigh-scattered brightness of unit solar flux serves as a multiplier for eliminating its effect in the brightness counts at the lower altitudes (< 80 km) in the raw data. The curve representing 90-degree solar zenith angle shows when the Chapman approximation fails.

2.5 Retrieval and Uncertainties

If the RAIDS data, $\boldsymbol{d}$, are binned into m altitudinal grids and the to-be-retrieved NO vertical profile, $\boldsymbol{x}$, is divided into n uniform layers, a geometric matrix, $\boldsymbol{G}$, is the transfer function relating $\boldsymbol{d}$ and $\boldsymbol{x}$.

$$\boldsymbol{Gm} = \boldsymbol{d} \tag{2.11}$$

Most of the inversion process involved in geophysics, hydrology, astronomy, and other disciplines often experience solving least squares problems that is of particular interest in ill-conditioned or

rank-deficient system. As explained in the previous sections, altitudes scanned by RAIDS though mostly fall in between 100 – 300 km as in Figure 2.1, they are subject to the ISS operations and at times they extend to lower or higher altitudes. Under these circumstances, several altitudinal bins likely have zero measurements and make the system ill-conditioned or rank-deficient. To assist this matter, an over-determined case is preferred so that the noisiness of the retrieval process due to missing data at any altitudinal bins may be minimized. $\boldsymbol{G}$ is then a rectangular matrix instead of a square one and the general solution for an over-determined case is simply

$$\boldsymbol{m} = (\boldsymbol{G}^T\boldsymbol{G})^{-1}\boldsymbol{G}^T\boldsymbol{d} \tag{2.12}$$

However, the inverse of $\boldsymbol{G}^T\boldsymbol{G}$ in Equation 2.12 does not exist when $\boldsymbol{G}$ is not of full column rank. Therefore, the singular value decomposition (SVD) is introduced to decompose G into

$$\boldsymbol{G} = \boldsymbol{U}\boldsymbol{S}\boldsymbol{V}^T \tag{2.13}$$

The generalized inverse of $\boldsymbol{G}$, $\boldsymbol{G}^{\dagger}$, which is called Moore-Penrose pseudoinverse, can be computed by the compact forms of $\boldsymbol{U}$, $\boldsymbol{S}$, and $\boldsymbol{V}$ [Aster et al., 2005].

$$\boldsymbol{G}^{\dagger} = \boldsymbol{V}_p\boldsymbol{S}_p^{-1}\boldsymbol{V}_p^T \tag{2.14}$$

where p refers to first p nonzero singular values in the decomposition. Then, the retrieval is simply the multiplication of $\boldsymbol{G}^{\dagger}$ and the observation, $\boldsymbol{d}$.

$$\boldsymbol{m}^{\dagger} = \boldsymbol{G}^{\dagger}\boldsymbol{d} \tag{2.15}$$

The uncertainties of each retrieved NO profile come from two sources: the Poisson noise on the spectrometer, the retrieval, and the pointing. The Poisson noise on an optical sensor is characterized as the square root of the received photon counts. The uncertainty, σ, due to the Poisson noise is propagated to the retrieved profile following Equation 2.16.

$$\mathrm{cov}(\boldsymbol{m}^{\dagger}) = \boldsymbol{G}^{\dagger}\mathrm{cov}(\boldsymbol{d})(\boldsymbol{G}^{\dagger})^T = \sigma^2\boldsymbol{G}^{\dagger}(\boldsymbol{G}^{\dagger})^T \tag{2.16}$$

The 95% confidence interval can be computed performing Equation 2.17.

$$\boldsymbol{m}^{\dagger} \pm 1.96 \cdot \mathrm{diag}[\mathrm{cov}(\boldsymbol{m}^{\dagger})]^{1/2} \tag{2.17}$$

Additionally, the potential pointing error is about 0.08 degree whereas the attitude control of ISS and the star tracker adds another 0.1 degree to the variance. This uncertainty of 0.18 degree is roughly the step size of the rotating platform and equivalent to the vertical spacing between limb measurements. The uncertainty from pointing can be estimated by multiplying derivative of the vertical NO density by the local altitudinal spacing which varies with altitude. One retrieved NO vertical profile is shown in Figure 2.4, where the uncertainties due to the Poisson noise and the pointing are included. The magnitude of uncertainty due to the Poisson is considerably small while that of pointing can be significant at the lower altitudes below 100 km.

2.6 Local-Time Variation of NO

Due to the characteristics of the ISS orbit, local sunlit time of the observed tangential point is coupled with its latitude as ISS orbits around the earth. This wide coverage over latitudes along with varying local sunlit hours makes it difficult to conclude any statistically significant seasonal variability at a given location. However, because of this, it allows investigating the NO abundance in the local atmosphere with different levels of solar irradiance due to varying solar zenith angles. In Figure 2.5, the coupled latitudes and local sunlit hours at the limb-scanned tangential points are illustrated in two ways with the 13 consecutive days (Jun 11 to Jun 23) of observation: the drifting of observed latitudes at the same local hours and observed local hours at certain latitude.

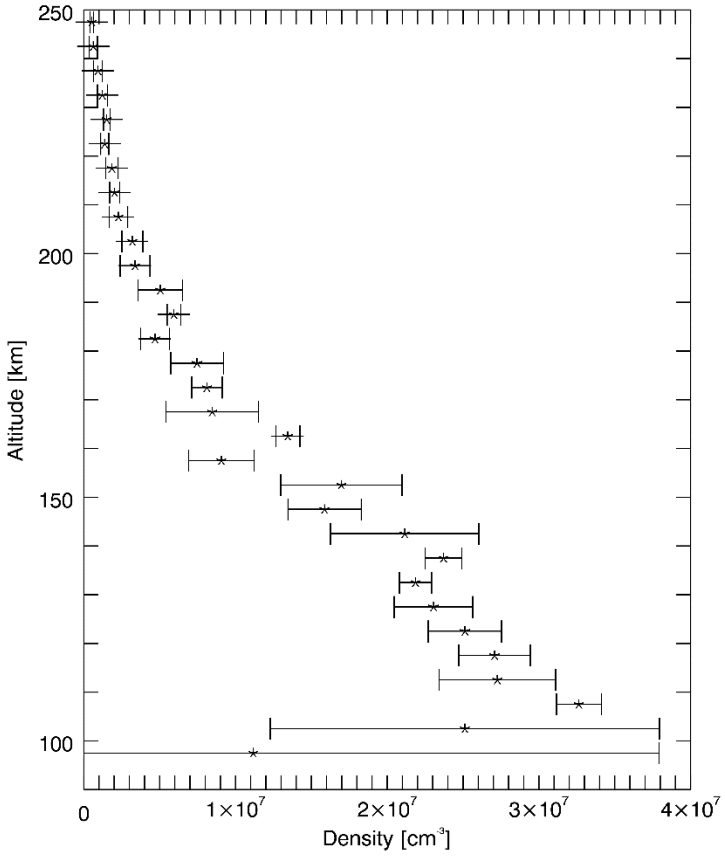

Figure 2.4. This sample retrieval of NO vertical profile is carried out by the principles described in Sections 2.4 and 2.5 at 50°N at 10 AM on May 28, 2010.

Great care therefore has been taken to select a temporal window of the available NO retrievals to cover all the sunlit local hours which are under similar geophysical conditions. Figure 2.6 illustrates the idea of the selection. In the top panel, NO abundance at 120 km at the equatorial region is plotted with local sunlit hour for days 120 to 220 of year 2010. The strap-like features are the signatures of the coupling between local time and latitude as described in Figure 2.5. The bottom panel shows the auxiliary indicators for selecting a period of time for local-time study. The modeled NO densities are shown in the unit of 10^6 molecules at two local hours: solid line as noon

and dashed line as 2 PM. The daily $F_{10.7}$ index in blue and the hourly soft X-ray irradiance in red are indicative of the solar activity levels. The dashed lines locate the period selected for this study, from June 10 to July 9. During this time, the $F_{10.7}$ index is low and at very similar level while M-class flares in the early days result in higher soft X-ray irradiance. Though the hourly NO densities predicted by NOx1D shows slight seasonal increase over time, it is the best period in 2010 for this study factoring in the data availability, solar activities, and the completeness of the data sets.

As the tangential points progress through different geographical locations (latitude, longitude, local time), the number of limb-scanned measurements varies from a set of geographical grids to another. The number of the available limb scans at each local sunlit hour during the selected temporal window (Figure 2.6) is shown in Figure 2.7. It is expected that a smaller number of scans correspond to a larger uncertainty if all other statistical conditions hold the same. On the other hand, care has to be taken while estimating mean and uncertainties of the observation and model. To make the comparison consistent, the modeled NO densities is considered as a data pool. Whenever the RAIDS observation is available for a particular time and location, modeled result under the same geophysical conditions is pulled out to be examined later. At the end, exactly the same number of samples are taken out from the model to draw the statistically significant comparison with the observation. RAIDS requires the scattered sunlight as the mean to observe the gamma-band emission at 236.5 nm so only the sunlit atmosphere is examined here. Figure 2.8 shows the comparison of the local-time variation from 7 AM to 4 PM between the RAIDS observation and the NOx1D model at the equatorial region (15°S – 15°N). There are only about 20 retrievals are available at 5 PM, a much smaller number than the rest of the hours (Figure 2.7) and resulting in much greater uncertainties, and therefore this local hour is excluded. The

uncertainties discussed in Section 5 are estimated and accounted for. A lesser number of profiles, such as at 12 and 2 PM, result in greater uncertainties; however, each uncertainty source contributes differently at each hour and each altitude where the measurements are taken. Since sunrise, NO production through temperature-dependent reaction of ground-state nitrogen and impact of photoelectrons to molecular nitrogen starts competing with the loss mechanism by photo-dissociation. This results in a gradual increase in NO density at altitude at and above 120 km. The increase peaks slightly after local noon. In the absence of sunlight, transport becomes the most significant loss mechanism.

2.7 Summary and Conclusions

The procedures are developed for retrieval of NO vertical profile from the RAIDS limb measurements at 236.5 nm. The ISS orbit allows observation at all the local sunlit hours but limits to certain latitudes on a given day. One month window from Jun 10 to July 9, 2010 is selected for study of the NO local-time variation. During the sunlit hours, the NO abundance at 120 km first decreases and then is followed by a gradual increase. The solar optically thin FUV radiance can penetrate to and be absorbed at the lower altitudes even at larger solar zenith angles and thus leads to the loss of $N(^4S)$ and NO. Going toward noon, the decrease of solar zenith angle allows the optically thick solar XUV irradiance to deposit at the lower altitude. When XUV is deposited, $N(^2D)$ and NO are produced. The production due to XUV reaches its maximum at around local noon to 2 PM. As solar zenith angle starts increasing, the NO production and its abundance decreases in the afternoon. The comparison between the RAIDS measurements and the NOx1D

modeled densities shows good agreement within 50% between 120 and 150 km. This strengthens the modern understanding of the thermospheric NO chemistry.

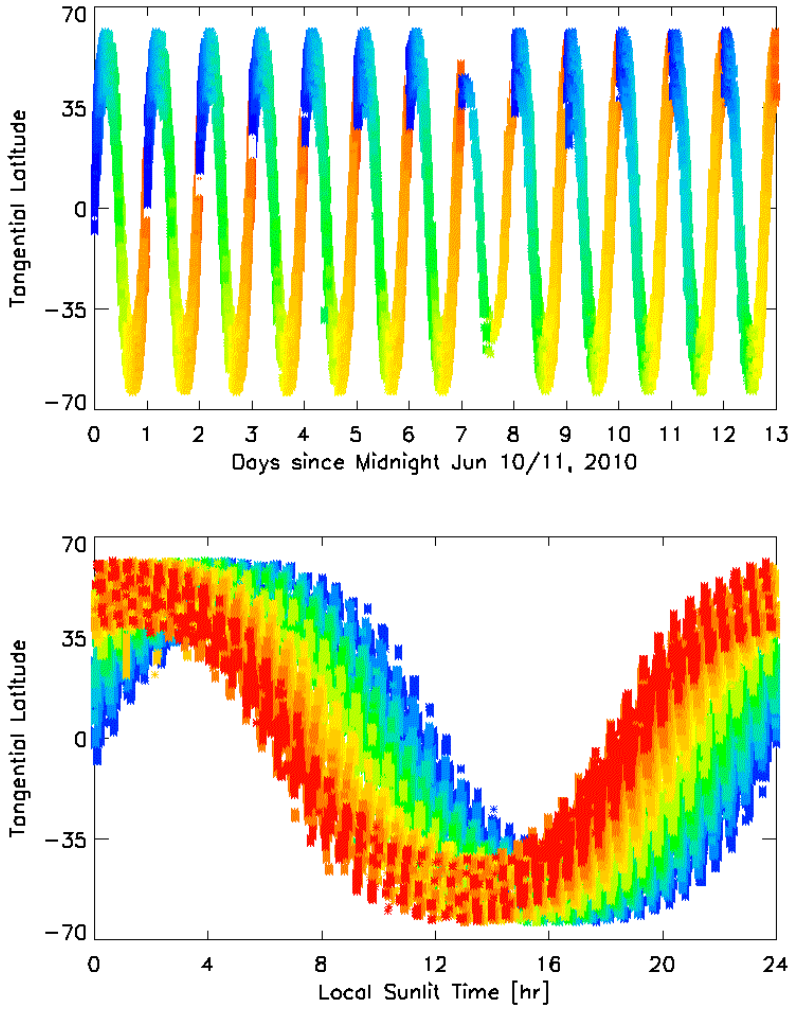

Figure 2.5. Illustration of the coupled latitudes and local sunlit hours at the limb-scanned tangential points. The consecutive 13-day (Jun 11 to Jun 23) observation shows the drifting of (top) observed latitudes at the same local hours (a particular color representing certain a local sunlit hour) and (bottom) observed local hours at certain latitude (a particular color representing a certain day).

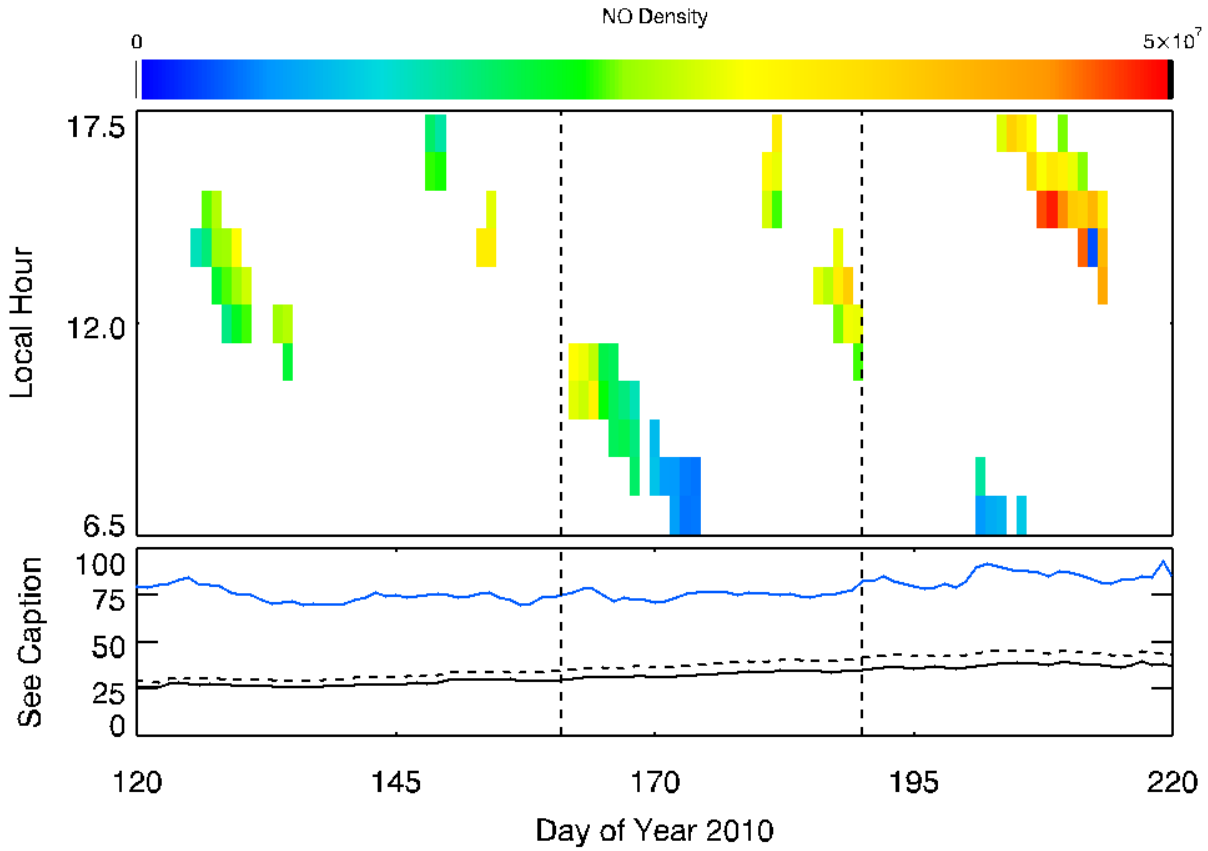

Figure 2.6. The NO abundance at 120 km at the equatorial region is plotted with local sunlit hour for days 120 to 220 of year 2010 (Top). The strap-like features are the signatures of the coupling between observed local time and latitudes. Auxiliary indicators (bottom) for selecting a period of time for local-time study are the modeled NO density (black), the $F_{10.7}$ index (blue) and the soft X-ray irradiance (red). NO density is shown in the unit of 10^6 molecules at local noon (solid) and 2 PM (dash). Solar activity level is represented by the radio $F_{10.7}$ index (blue) and the soft X-ray irradiance multiplied by 10^5 (red). The dashed lines locate the period selected for this study, from June 10 to July 9. During this time, the $F_{10.7}$ index is low and at very similar level while M-class flares in the early days result in higher soft X-ray irradiance. Though the hourly NO densities predicted by NOx1D shows slight seasonal increase over time, it is the best period in 2010 for this study factoring in the data availability, solar activities, and the completeness of the data sets.

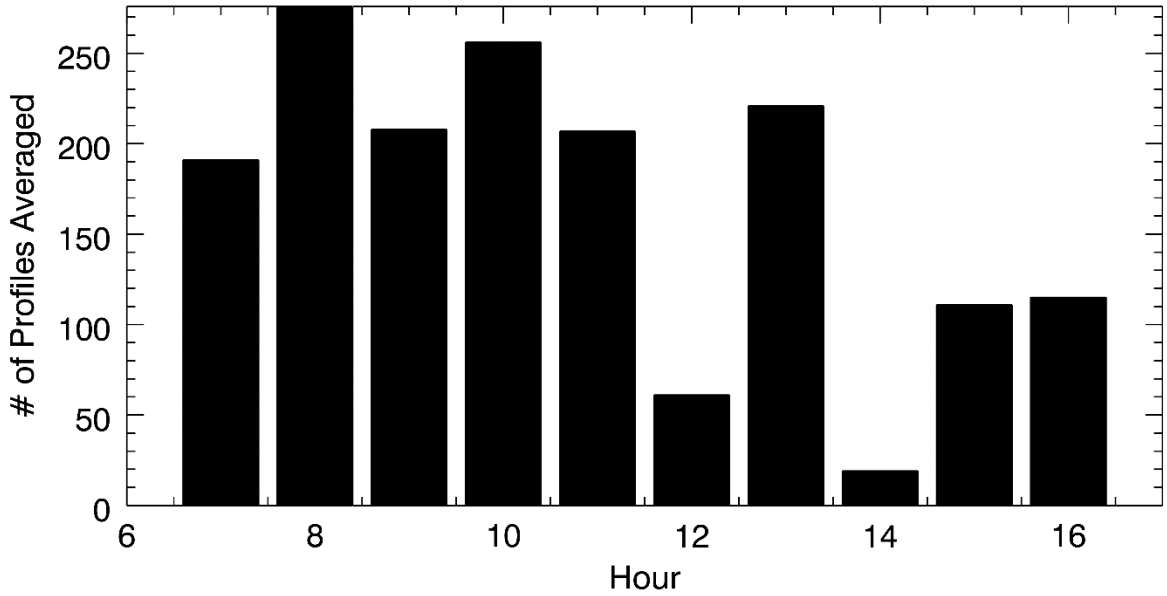

Figure 2.7. The number of profiles gets averaged for the local-time study at each local sunlit hour.

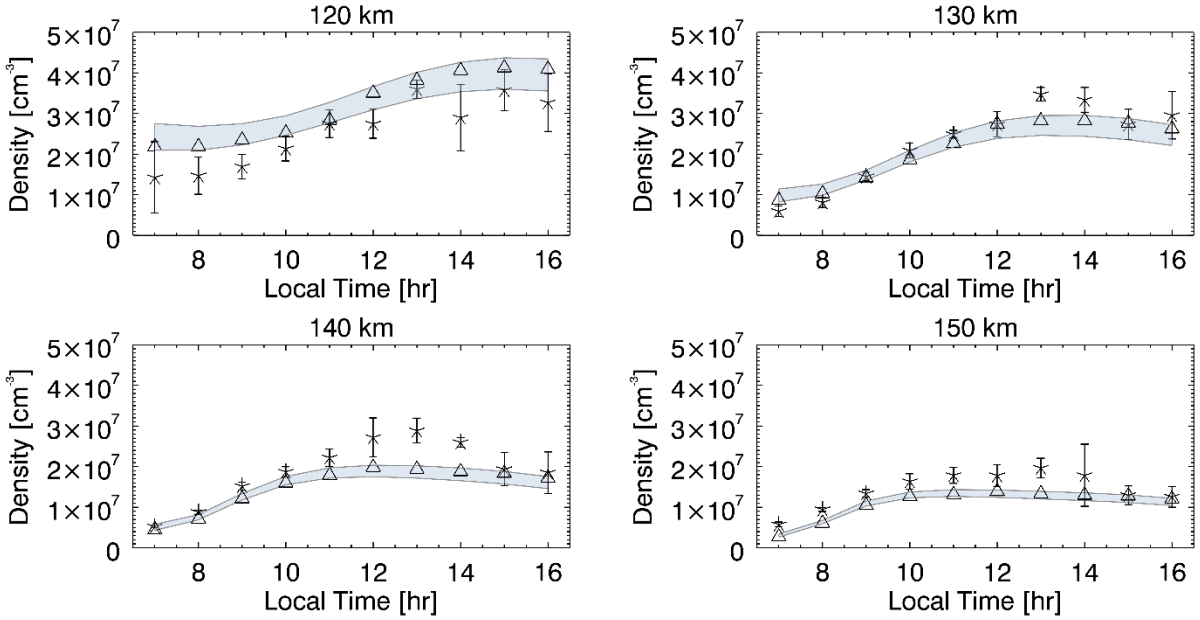

Figure 2.8. The local-time variation of NO (black stars) derived from the retrieved NO profiles over the time period of June 11 to July 10, 2010. Data shown here cover the measurement around the geomagnetic equator (15°S to 15°N). The modeled NO densities by NOx1D (red triangles) appear to agree well with the RAIDS observations at the higher altitudes.

References

Aster, R. C. et al., "Parameter estimation and inverse problems," Elsevier Academic Press, 2005

Bailey, S. M., C. A. Barth, and S. C. Solomon, "A model of nitric oxide in the lower thermosphere," Journal of Geophysical Research, 107(A8), doi:10.1029/2001JA000258, 2002.

Bailey, S. M., A. W. Merkel, G. E. Thomas, and J. N. Carstens, "Observations of polar mesospheric clouds by the Student Nitric Oxide Explorer," Journal of Geophysical Research, 110, D13203, doi:10.1029/2004JD005422, 2005

Baker, D. N., C. A. Barth, K. E. Mankoff, S. G. Kanekal, S. M. Bailey, G. M. Mason, and J. E. Mazur, "Relationships between precipitating auroral zone electrons and lower thermospheric nitric oxide densities: 1998 – 2000," Journal of Geophysical Research, A11, 2001

Barth, C. A., W. K. Tobiska, and D. E. Siskind, "Solar-terrestrial coupling: Low-latitude thermospheric nitric oxide," Geophysical Research Letters, 15, 1988

Barth, C. A., "Nitric oxide in the lower thermosphere," Planetary and Space Science, 40, 1992

Barth, C. A., S. M. Bailey, and S. C. Solomon, "Solar-terrestrial coupling: Solar soft X-rays and thermospheric nitric oxide," Geophysical Research Letters, 26, 1999

Barth, C. A., D. N. Baker, K. D. Mankoffand S. M. Bailey, "The northern auroral region as observed in nitric oxide," Geophysical Research Letters, 26, 2001

Barth, C. A. et al., "Global observations of nitric oxide in the thermosphere," Journal of Geophysical Research, 108(A1), 1027, doi:10.1029/2002JA009458, 2003

Barth, C. A. and S. M. Bailey, "Comparison of a thermospheric photochemical model with Student Nitric Oxide Explorer (SNOE) observations of nitric oxide," Journal of Geophysical Research, 109, A03304, doi:10.1029/2003JA010227, 2004

Budzien, S. A. et al., "The Remote Atmospheric and Ionospheric Detection System experiment on the ISS: Mission Overview," Proc. SPIE 7438, Solar Physics and Space Weather Instrumentation III, 74380X, doi:10.1117/12.826513, 2009

Budzien, S. A. et al., "The RAIDS experiment on the ISS: on-orbit performance," Proc. SPIE 8148, 814805, 2011

Crutzen, P. J., "The influence of nitrogen oxides on the atmospheric ozone content," Quart. J. R. Met. Soc., 96, 1970

Hinteregger, H. E., K. Fukui, and B. R. Gilson, "Observational reference and model data on solar EUV from measurements on AE-E," Geophysical Research Letters, 8, 1981

Kumar, C. K., A. P. Batra, and L. Klein, "Solar cycle variation of nitric oxide in the thermosphere," Journal of Geophysical Research, 104, 1999

Minschwaner, K. and D. E. Siskind, "A New Calculation of NO Photolysis in the Stratosphere Mesosphere and Lower Thermosphere," Journal of Geophysical Research, 98, 1993

Mlynczak, M., F. J. Martin-Torres, J. Russell, K. Beaumont, S. Jacobson, J. Kozyra, M. Lopez-Puertas, B. Funke, C. Mertens, L. Gordley, R. Picard, J. Winick, P. Wintersteiner, and L. Paxton, "The natural thermostat of nitric oxide emission at 5.3 μm in the thermosphere observed during the solar storms of April 2002," Geophysical Research Letters, 30, 2003

Randall C. E., V. L. Harvey, D. E. Siskind, J. France, P. F. Bernath, C. D. Boone, and K. A. Walker, "NOx descent in the Arctic middle atmosphere in early 2009," Geophysical Research Letters, Vol. 36, 2009

Richards, P. G., T. N. Woods, and W. K. Peterson, "HEUVAC: A new high resolution solar EUV proxy model," Advances in Space Research, 37, 2006

Rodgers, E. M., S. M. Bailey, H. P. Warren, T. N. Woods, and F. G. Eparvier, "Nitric oxide density enhancements due to solar flares," Advances in Space Research, 45, 2010

Siskind, D. E. et al., "The Possible Effect of Solar X-Rays on Thermospheric Nitric Oxide," Journal of Geophysical Research, Vol. 95, 1990

Solomon S., P. J. Crutzen, and R. G. Roble, “Photochemical coupling between the thermosphere and the lower atmosphere 1. Odd nitrogen from 50 to 120 km,” Journal of Geophysical Research, 87, 1982

Solomon, S. C., P. B. Hays, and V. J. Abreu, “The auroral 6300 Å emission: Observations and modeling,” Journal of Geophysical Research, 93, 1988

Solomon, S. C., and V. J. Abreu, “The 630 nm dayglow,” Journal of Geophysical Research, 94, 1989

Stephan, A. W. et al., “The Remote Atmospheric and Ionospheric Detection System on the ISS: Sensor performance and space weather applications from the extremem to the near ultraviolet,” Proc. SPIE 7438, Solar Physics and Space Weather Instrumentation III, 2009

Stephan, A. W., A. B. Christensen, K. Minschwaner, S. A. Budzien, R. L. Bishop, and J. H. Hecht, “Characterization of sensitivity degradation seen from the UV to NIR by RAIDS on the International Space Station,” Proc. SPIE 8148, Solar Physics and Space Weather Instrumentation IV, 2011

Yonker, J. D., “Contribution of the First Electronically Excited State of Molecular Nitrogen to Thermospheric Nitric Oxide,” PhD dissertation, 2013

CHAPTER 3 Soft X-ray irradiance measured by the Solar Aspect Monitor on the Solar Dynamic Observatory Extreme ultraviolet Variability Experiment

Abstract

The Solar Aspect Monitor (SAM) is a pinhole camera on the Extreme-ultraviolet Variability Experiment (EVE) flying on the Solar Dynamics Observatory. SAM projects the solar disk onto the CCD through a metallic filter designed to allow only solar photons shortward of 7 nm to pass. Contamination from energetic particles and out-of-band irradiance is, however, present. We present a technique for isolating the 0 to 7 nm integrated irradiance from the SAM signal to produce broadband irradiance for the time period of the SAM observations. The results of this analysis agree with the zeroth-order product from the EUV SpectroPhotometer (ESP) – a separate instrument on EVE and has a photodiode measuring the same bandwidth – within 25%. We also make comparisons with measurements from the Student Nitric Oxide Explorer (SNOE) Solar X-ray Photometer (SXP) and the Thermosphere Ionosphere Mesosphere Energetics and Dynamics (TIMED) Solar EUV Experiment (SEE) at similar levels of solar activity. We show that the SAM broadband results compare well to the other measurements of the 0.1 to 7 nm irradiance.

Keywords: solar irradiance, soft X-ray, XUV

3.1 Introduction

Over the history of solar observation, indices have been developed to characterize solar activity level. Sunspot number and the 10.7 cm radio flux (F10.7) are based on the ground measurements and therefore are available back in 1818 [SILSO data, Royal Observatory of Belgium, Brussels, http://www.sidc.be/silso/home] and 1946 [Tapping, 1987; 2013] respectively. With technical challenges of solar monitoring instruments at shorter wavelengths, such as ultraviolet and X-ray, to this date uncertainties lie in solar irradiance measured by different spacecraft at these wavelengths [Feng et al., 1989; Bailey et al., 2006; BenMoussa et al., 2013; Solomon and Qian, 2005]. Solar radiation shortward of 20 nm is mostly absorbed at the altitudes between 100 and 150 km and is the major driver to both neutral and ionized atmosphere [Fuller-Rowell et al., 2004]. Several names have been used interchangeably for this wavelength band, such as soft X-ray [Barth et al, 1988], X-ray ultraviolet (XUV) [Fuller-Rowell et al., 2004; Woods et al., 2004; 2008], and vacuum ultraviolet (VUV) [Wood et al., 1998]. The EUV and soft X-ray radiation is shown to be critical to electron densities in the ionospheric E-region [Sojka et al., 2006; Solomon, 2006]. Changes of neutral density have impact on satellite drags and have to be considered for the orbit calibration [Emmert et al., 2010]. The important role solar soft X-ray irradiance plays in the NO production was recognized in the late 1980s [Barth et al., 1988; Siskind et al., 1990].

The history of solar soft X-ray observation can be traced back to the l960s. Sounding rocket measurements opened a page to several satellite-based experiments, including SOLRAD, Orbiting Solar Observatory (OSO) [Hall and Hinteregger, 1970; Hall, 1971], the Atmospheric Explorer (AE) satellites [Gibson and Van Allen, 1970], SkyLab (1973 – 1979) [Vaiana et al., 1976], and Solar

Maximum Monitor (SMM) (1980) [Acton et al., 1980; Bohlin et al., 1980]. The Soft X-ray Telescope (SXT) on Yohkoh took full-disk images of the Sun between 0.2–3 nm from 1992 to 2005 [Ogawara et al., 1992]. Soft X-ray irradiance can be estimated with an isothermal spectral model and modeled by means of differential emission measure (DEM) [Acton et al., 1999]. The Solar soft X-ray Photometer (SXP) on the Student Nitric Oxide Explorer (SNOE) had several broadband channels making daily measurement of solar soft X-ray with bandpasses of 2–7 nm, 6–19 nm, and 17–20 nm [Bailey et al., 1999; 2006]. Solar Extreme ultraviolet Monitor (SEM) on the SOlar and Heliospheric Observatory (SOHO) has continuously measured the solar EUV irradiance since 1996 [Judge et al., 1998; Ogawa et al., 1998]. Its zeroth-order channel monitors the full-disk solar irradiance from 0.1 to 50 nm, and has a first-order channel measuring the He II 30.4 nm irradiance. The NOAA Geostationary Operational Environmental Satellite (GOES) series satellites carry X-Ray Sensor (XRS), measuring X-ray flux at 0.05–4 nm and 0.1–0.8 nm. The Solar EUV Experiment (SEE) onboard the Thermosphere, Ionosphere, and Mesosphere Energetics and Dynamics (TIMED) satellite carries the XUV Photometer System (XPS) and the EUV Grating Spectrograph (EGS) to provide daily irradiance of XUV between 0.1 and 35 nm and EUV between 25 and 200 nm [Woods et al., 1999]. The Solar Radiation and Climate Experiment (SORCE) XPS [Woods et al., 2008] is essentially identical to the one on TIMED/SEE. The X-Ray Telescope (XRT) on Hinode started taking X-ray images since 2006 [Golub et al., 2007; Kano et al., 2008]. Woods et al. [2004] gave a detailed historical account of the spaceborne measurements of solar EUV and soft X-ray irradiance. To this date discrepancies still lie among all the soft X-ray data sets and models [Solomon and Qian, 2005]. Theoretical and empirical reference models [Tobiska et al., 2010; Warren, 2005; Richards et al., 2006; Chamberlin et al., 2007, 2008] of the solar spectrum are therefore established to better assist climate models when measurements are not

available; however, comparison of modeled atmospheric response using solar measurements with available atmospheric data has shown that the soft X-ray may be underestimated in the solar reference models and needs to be scales by a factor of 2 or more [Bailey et al., 2002]. This uncertainty is verified in studies of ion and electron densities for which are created in proportion to the solar ionizing irradiance [Solomon et al., 2006].

Launched in 2010, Solar Dynamics Observatory (SDO) is the first mission of NASA's Living With a Star (LWS) program. The goal of the SDO mission is to understand the solar variability and its impact to the terrestrial technology and society. SDO facilitates not only better knowledge of heliophysics through studying the evolution of solar magnetic fields and its atmosphere but also the connection between solar activities and its terrestrial effects. The Extreme ultraviolet Variability Experiment (EVE) is one of the three instruments on SDO [Hock et al, 2010; Woods et al., 2010]. EVE measures the soft X-ray and EUV solar spectrum from 0.1–105 nm which strongly drives the variability of the Earth's atmosphere. The Solar Aspect Monitor (SAM) is a pinhole camera on EVE. It is designed to image the solar disk with photons shortward of 7 nm (energy above 180 eV). Images are taken every 10 seconds. Details of the SAM instrumentation are covered in Section 2. The EUV SpectroPhotometer (ESP) on EVE is an expanded version of SOHO/SEM. It is a non-focusing broadband spectrograph. Its quad-diode (QD) channel produces broadband soft X-ray irradiance measurements in the same spectral band as SAM [Didkovsky et al., 2009]. In this study, broadband irradiance in soft X-ray wavelengths is obtained from the SAM images and compared with the ESP zeroth-order QD product.

3.2 Instrument and Observations

SAM shares a CCD with one of the Multiple EUV Grating Spectrograph (MEGS-A) on EVE [Woods et al., 2010; Hock et al., 2010]. It operates in two modes. In XUV photon-counting mode, a Ti/Al/C foil filter is in position to allow photons shortward of 7 nm (>180 eV) to reach the detector. Dark measurements are made when the pinhole is covered by a dark filter. This dark mode is performed only for about one minute per day during normal operation. SAM operates in the XUV mode more than 23 hours a day.

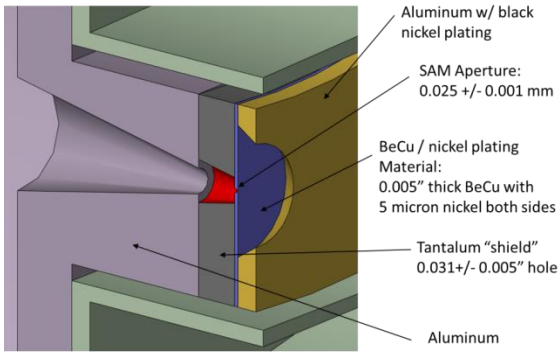

Figure 3.1. The pinhole design of SAM.

The SAM entrance aperture is a 26 µm diameter pinhole set 32 cm from the CCD. The size of a CCD pixel is 15 µm by 15 µm, which gives approximately 15 arcsecond resolution of the solar disk. SAM projects the solar disk onto the corner of the CCD where spectral lines from MEGS-A are dim. Though few, some MEGS-A photons appear and contaminate the SAM images. Because the detector is tilted by 17° (due to the MEGS-A instrument design) relative to the normal of the principal axis, projection of the Sun is slightly elliptical with a semi major axis of about 215 pixels in the E/W direction and a minor axis of about 205 pixels in the N/S direction. The corona extends about 50 pixels above the limb surface. For the CCD used on EVE, an electron hole is

created when equivalent energy, E_{si}, of 3.63 eV impacts a CCD pixel and is registered as one data number (DN). The calibration shows that the gain of the CCD, *G*, is 2.47 electrons per DN. The conversion from DN to energy simply follows Equation 3.1.

$$E = E_{si} \cdot G \cdot DN_{corrected} \tag{3.1}$$

Dividing the constant, 1239.84, in eV·nm by the energy, *E*, in eV, yields wavelength in nm. Units of nm, eV, and DN are used interchangeably in the following context. Equation 3.1 should only be used for dark-count corrected DN values. The key values used in the data process may be referred to in Table 1. Two components contributing to the background dark counts are the electronic bias and the thermal noise. Four virtual pixels are placed at the beginning of each CCD read-out row and are the indication of charge amplifier signal prior to reading actual CCD pixels. The average of these four pixels is obtained and subtracted off from all the pixels of interest in that row for ever frame. At the temperature the EVE CCDs operate at, the thermal noise contribution is about 3 DN/s with uncertainty of about 2 DN/s. Both of these two terms are relatively small compared to the contamination from multiple sources appears at the SAM corner of the CCD.

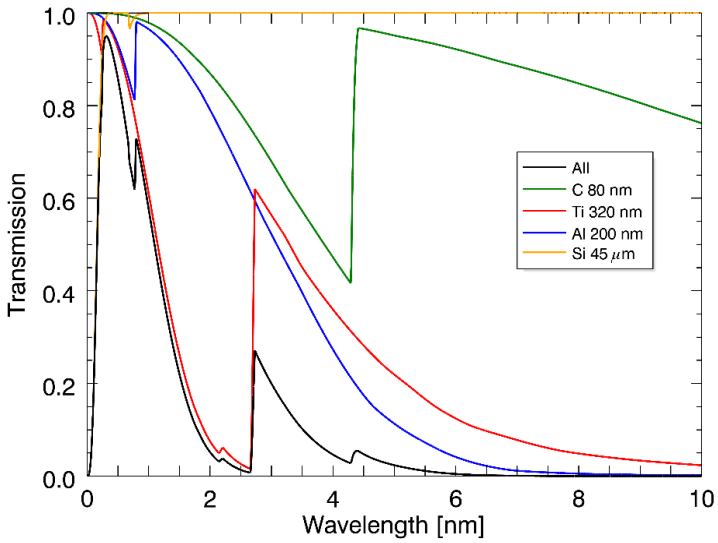

Figure 3.2. The transmission function of SAM.

As the goal is to obtain solar irradiance at soft X-ray wavelengths, the XUV filter is designed to allow high-energy photons. Thickness of each material of the SAM foil filter is carbon of 80 nm, titanium of 320 nm, and aluminum of 200 nm and that of the Si CCD is 45 microns. With these parameters, the SAM transmission is modeled using tabulated atomic scattering factors [Henke et al., 1993] and shown in Figure 3.2. Sharp edges in transmission are shaped by each material: C at around 4.5 nm, Ti from 1.5 to 3 nm, and Al at around 0.7 nm. The declining of transmission below 0.5 nm is defined by the silicon absorption of the detector. This response function is slightly different than the one in the work presented by Hock et al [2010] due to better knowledge of the Si thickness. SAM's nature of low data counts has led to overwhelming contamination from energetic particles with similar energy levels of the designated soft X-ray photons. Study of the raw DN counts on the SAM images reveals the semi-diurnal encounter of the SDO spacecraft with the particle in the outer (electron) Van Allen radiation belt. Some of these particles strike the CCD directly and some cause bremsstrahlung from the supporting material around the CCD, resulting in high-DN read-outs on the CCD pixels. The SAM dark filter is in position about one minute per day. These 1-minute dark measurements are insufficient to directly determine the changing particle environment the spacecraft encounters every 10 seconds. Therefore, more involved method has to be performed to remove the particle contribution from the measurements.

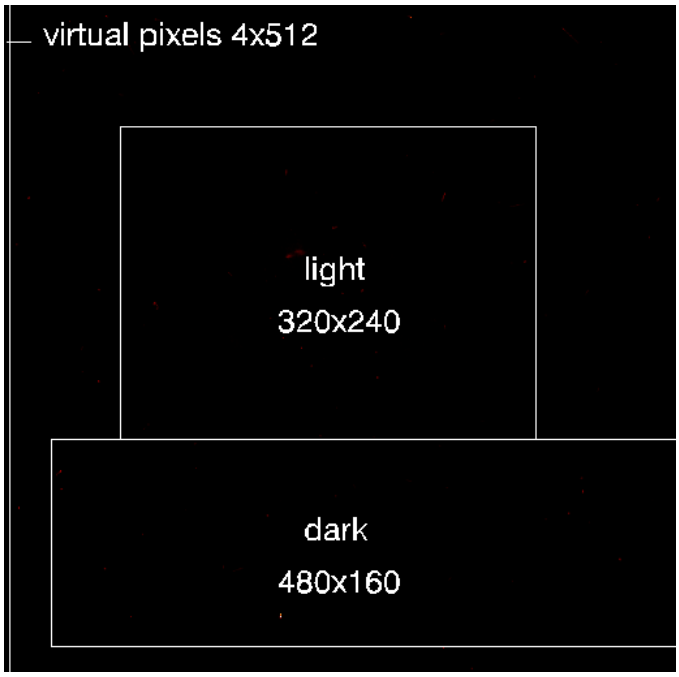

Figure 3.3. A 512x512-pixel area is truncated from a corner of a MEGS-A image along with a 4x512-pixel column of virtual pixels from the first pixels of each CCD readout row to form a data set for the SAM data analysis. Light is a 320x240 rectangular sunlit area and dark is a 480x160 strip adjacent to light but non-sunlit.

Since SAM projects both the solar disk and atmosphere onto a relatively dark corner of the MEGS-A CCD, to include any possible flares occurring at the limb and the corona, size of the sunlit image taken for the analysis is 320 pixels by 240 pixels from this corner on the MEGS-A image. This area is referred to as *light* in the following context. A narrow strip of non-sunlit area below the sunlit rectangle is chosen to be the representation of the particle environment at all times for calibration. It is located close enough to the light area so that what is present on this portion of the CCD resembles that on *light*. This area will be hereafter referred to as *dark*. The size of the dark is chosen to be 480 pixels by 160 pixels so that there are the same number (67,200) of pixels on both types of images. During nominal science mode, each complete MEGS-A CCD image provides as a single SAM light and dark image pair, from which soft X-ray irradiance can be obtained using the techniques presented in Section 3. Over 8,000 image pairs as Figure 3.3 are

produced in one day of nominal operations. The top panel of Figure 3.4 shows the DN histograms of the actual light (red) and dark (black) images which represent most of the non-flaring days. When the Sun is quiet, the light and dark distributions lie close together and do not show apparent differences below 20 DN and beyond 1000 DN. The non-zero dark distribution is indicative of non-photon sources of DN. It is hypothesized that information of the incoming flux lies in the difference of the light and dark distribution. Hereafter, unless otherwise specified, the difference of the light and dark histograms is simply referred as *histogram*.

3.3 Broadband Irradiance

Conversion from broadband solar measurements to irradiance requires an instrument response function and a solar reference spectrum. Scaling factors are calculated to convert measured quantity (either voltage or current) to solar irradiance [Bailey et al., 2006]. Figure 3.1 shows the modeled transmission function of SAM. The Solar Irradiance Reference Spectra (SIRS) for the 2008 Whole Heliosphere Interval (WHI) [Chamberlin et al., 2008; Woods et al., 2009], whose spectral resolution is 0.5 nm, is the reference spectrum implemented in this study. The broadband SAM measurements in DN is the incoming solar irradiance weighted by the device response function.

$$DN = m \cdot f \cdot I_{sun} \tag{3.2}$$

where m is 3.68×10^{-9} DN/(W·m^{-2}) to DN and f is a unit-less weighting factor and is the ratio of the weighted solar irradiance by the instrument response function to its non-weighted value. SAM not only provides broadband information but energy resolved information also resides in its DN histogram. Further investigation of the DN histogram grants knowledge toward obtaining a clean

version of broadband irradiance from particle contamination. The goal of this study is to establish routines that are able to produce solar irradiance from the SAM images and all the decision are to be made based on the information residing in these images.

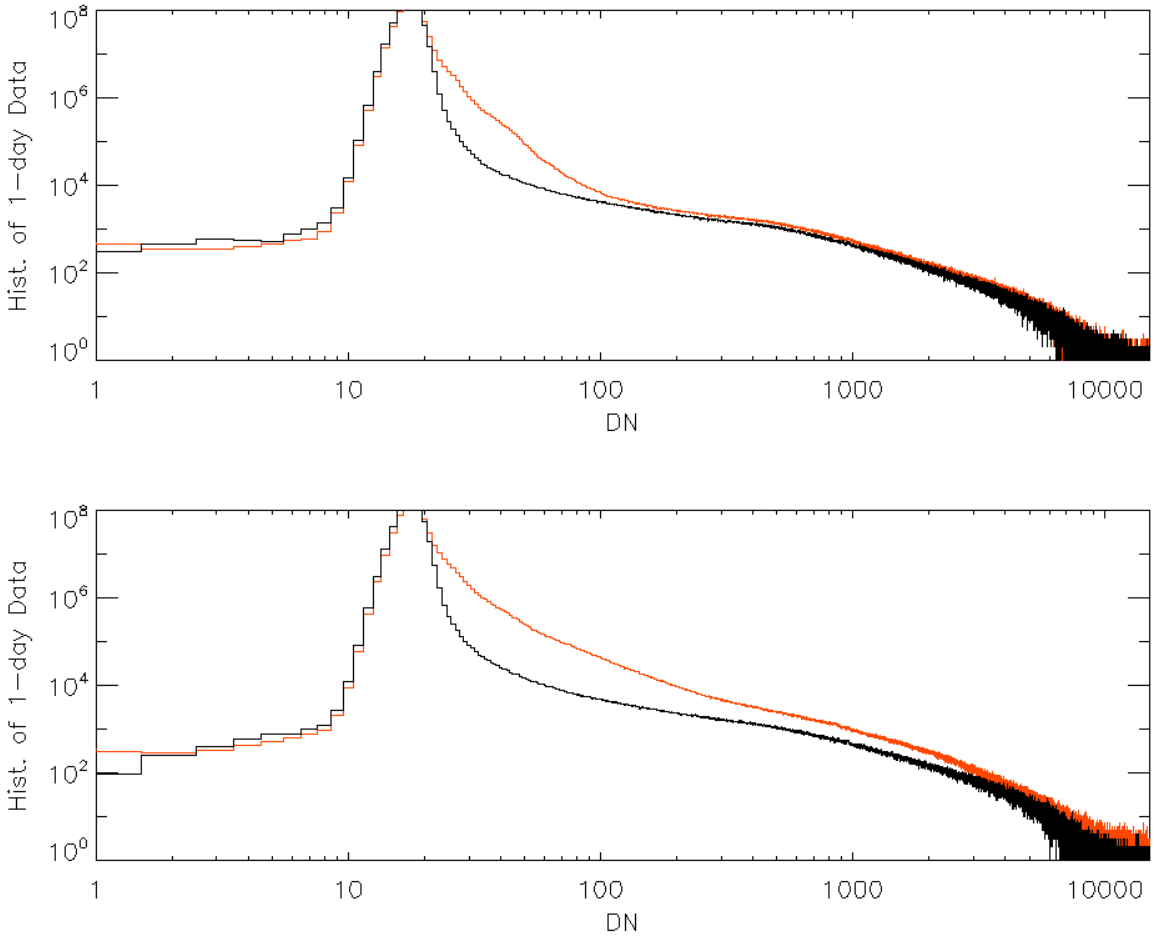

Figure 3.4. Examples of DN histograms of 1-day light (red) and dark (black) images, each of which contains information of over 8,000 10-second images. The top panel is representative of a typical day of low to medium solar activity and the bottom one is an extreme case where a strong flare takes place and the light and dark curves are apart all the way toward the high end of the DN distribution.

3.3.1 Narrow Bands

Information of solar irradiance as well as particles resides in the DN histogram, upon which fifteen narrow bands are defined to estimate contribution from the Sun and particles. The narrow bands were originally defined in wavelength regarding to certain emission lines. Uniform digitation in DN however provides finer (coarser) resolution toward shorter (longer) wavelengths. Therefore, the narrow bands are defined based on DN and with nonuniform DN range. The bandwidth is 100 DN for bands including DN values between 100 and 1,000 and 1,000 DN for those including DN values above 1,000. Direct interpretation from integral of a narrow DN range to narrowband irradiance creates big uncertainties. These uncertainties can be minimized by taking the difference of integrals of two broader bands of different DN ranges as in Equation 3.3.

$$I_{NB_i} = K\left[\frac{\sum_j p\left(15 \le j < DN_{i,high}\right)}{f_{i,high}} - \frac{\sum_j p\left(15 \le j < DN_{i,low}\right)}{f_{i,low}}\right] \tag{3.3}$$

The numerator of each term in the square bracket is the integrals of pixel values, *p*, from 15 DN to the upper limits, $DN_{i,low}$ and $DN_{i,high}$, which form the narrow band. The denominator, *f*, is the weighting factor as in Equation 3.2 obtained for the designated DN range and K, 2.72×10^{-10} $W\cdot m^{\wedge 2}/DN$, is the reciprocal of *m* in Equation 3.2. As an example, narrowband #1 is the difference of the integrals from 15 DN to 16383 DN ($DN_{1,high}$) and from 15 DN to 6999 DN ($DN_{1,low}$). Fifteen narrow bands are tabulated in Table 1. According to the WHI quiet-Sun spectrum, about 73% of the solar irradiance shortward of 7 nm lies between 2–7 nm (bands 14 and 15) where SAM is insensitive to. The fraction drops quickly to insignificance toward shorter wavelengths. Yet significant amount of energy is released from shortward of 2 nm when the Sun is flaring. Figure 3.5 shows the correlation of these narrow bands with the GOES XRS A (0.5–4 Å , XRS B (1–8 Å), F10.7, and the raw SAM broadband irradiance itself. Year-long data of 2011 (dot), 2012 (dash), and 2013 (dash dot) as well as the four-year data set from 2010 to 2013 (solid) are presented. The

correlation with the GOES data is only performed during the active days, when the X-ray level is above 10^{-6} W·m^{-2} in 1–8 Å or above 10^{-7} W·m^{-2} in 0.5–4 Å, as GOES XRS is designed to be highly sensitive to solar X-ray flux. Exiting from its minimum, the Sun did not have many flares and the GOES XRS channels were low in 2010 so the 2010 correlation curves are not presented. Shaded areas indicate the overlapping wavelength ranges with GOES XRS-A (orange) and XRS-B (blue) and out-of-band wavelength range (green) with the assumption that energy of one photon is totally absorbed by one pixel. Figure 3.5 indicates: 1) high correlation between bands 1–8 and the GOES irradiance; 2) high correlation between bands 10–15 with F10.7; and 3) decreasing correlation between narrow bands and broadband irradiance toward longer wavelengths. In other words, the variability of the shorter-wavelength bands dominates that of the broadband irradiance. Though not shown in Figure 3.5, the 2010 data have similar trend with F10.7 as the other years but opposite trend with the GOES channels. Thus, a flaring component of the solar irradiance or particle contribution may be characterized by shorter-wavelength bands whereas a quiet component by longer-wavelength bands. Study of the narrow bands helps develop the procedure to remove particle contamination in the following sections.

3.3.2 One-component Method

Though the best knowledge of dark from calibration is subtracted previously, particle contamination appears in all DN levels as the result of SDO's encounter with the radiation belt semi-diurnally in its geosynchronous orbit. Regardless the solar activity levels, the enhancement of the received signal brought by particles is close to 10 times more variable than and overwhelms the true solar irradiance. This effect is more significant at the higher-energy end of the SAM

wavelength range where solar variability is high. Only during flares does solar flux at these high-DN values rise above the noise level as shown in the bottom panel of Figure 3.4. In our analysis a histogram is obtained at every 10 second time step. In the *one-component* method, a component in the solar irradiance is assumed to correlate with the F10.7 index as shown in Figure 3.5 and that the raw irradiance, I_r, converted from total DN by Equation 2 can be expressed as a combination of contributions from true solar irradiance, I_s, and particle contamination, s_p, as Equation 4.

$$I_r = I_{s,1-comp} + s_{p,1-comp} \tag{3.4}$$

The terms with subscript, *1-comp*, are to be distinguished from the later-introduced two-component terms. The raw irradiance is the broadband signal obtained by integrating all the pixels of above 15 DN except the saturated ones. Shown in Figure 3.5, bands 1–6 at the highest-energy end have low correlation (< 0.2) with the F10.7 index and are selected to represent the variability of the particle term. Equation 4 is rewritten into Equation 5.

$$I_{BB} = I_{s,1-comp} + A \cdot I_{NB1-6} \tag{3.5}$$

The left-hand term, noted BB for broadband, is essentially the summation of all the narrow bands 1–15 and is the broadband irradiance from 0.01 to 7 nm. The coefficient, *A*, is a multiplier to represent the variability characterized by the narrowband measurements. It is not measureable and can only be estimated. Given the raw broadband and narrowband measurements, each value of *A* corresponds to a new $I_{s,1\text{-}comp}$, as Equation 5. If *A* is greater than one, it indicates a fraction of total irradiance in the rest of the bands process similar variability as due to particles. If A is less than one, a fraction of the bands selected to represent particles is rather subject to solar flux. The estimation of *A* is performed by substituting various values for *A* until a maximal correlation between the resulting solar term, $s_{s,1\text{-}comp}$, and the F10.7 index is reached. Since F10.7 is a daily index, daily averages of broadband and narrowband measurements over certain period of time are

taken to form I_{BB} and $I_{NB1\text{-}6}$. Data studied include dates from May 15 (day 135), 2010 to Dec 31, 2013, providing 1327 daily and 31,848 hourly data. Out of these four years, the Sun is most active in 2011 and quietest in 2010. Estimates of coefficients A and B are obtained for all individual years with year-long data as well as all four-year data. The comparison among one-year and four-year is illustrated in Figure 3.6. The greater-than-unity one-component estimates of A for all individual years suggest the likelihood of particle contribution to bands 7–15 and the variation of the estimates indicates partial inclusion of solar irradiance in the particle term. The estimate of A derived from four-year data (thick dashed line) is 1.52 and the corresponding correlation between solar component, I_s, and F10.7 is 0.86.

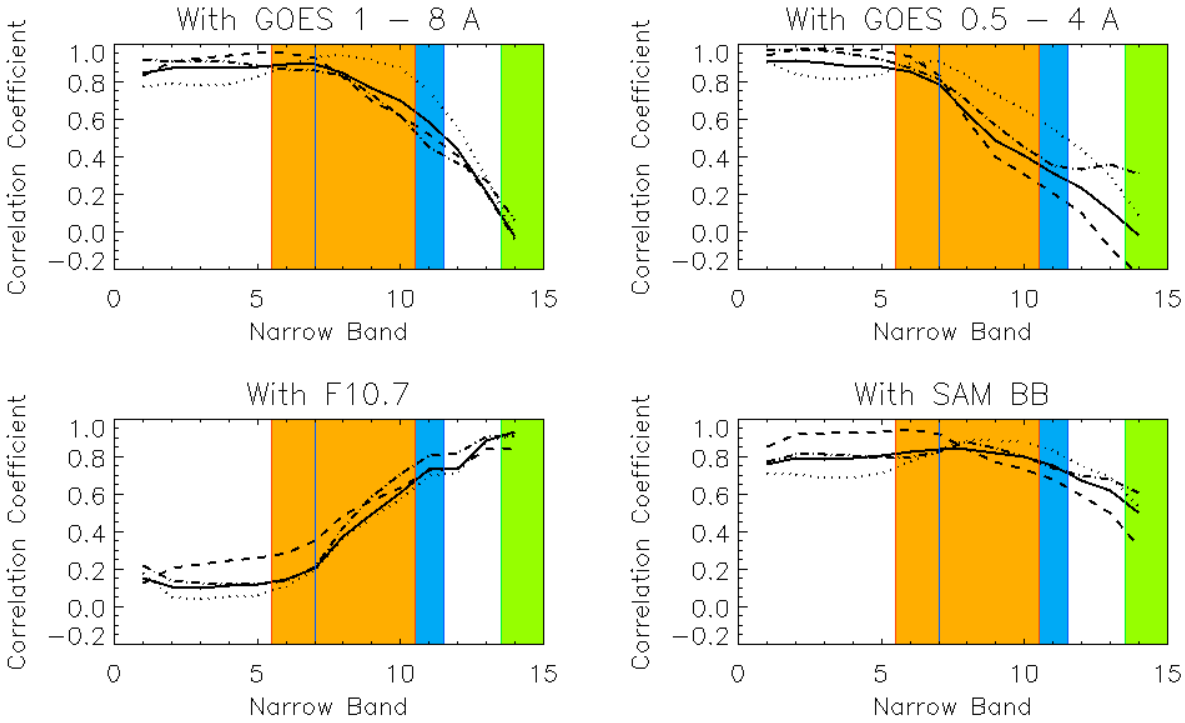

Figure 3.5. Correlation between each narrow band and the GOES 1–8 A (top left), 0.5–1 A (top right), F10.7 (bottom left), and the SAM broadband irradiance. Year-long data of 2011 (dot), 2012 (dash), and 2013 (dash dot) as well as the four-year data set from 2010 to 2013 (solid) are presented in the figures. Note that the correlation with the GOES data is only performed during the active days, when the X-ray level is above 1e-6 W/m^2 in 1-8 A or above 1e-7 W/m^2 in 0.5-4 A, as GOES XRS is designed to be highly sensitive to solar X-ray flux, which is the reason the 2010 data are not included in this comparison. Shaded areas indicate the overlapping wavelength ranges with GOES XRS-A (orange) and XRS-B (blue) and out-of-band wavelength range (green) with the assumption that energy of one photon is totally absorbed by one pixel.

Table 3.1. Definition of narrow bands – upper and lower limits in DN, energy, and wavelength. To minimize the uncertainties caused by assuming energy of one photon is completely absorbed by one pixel, signal strength of a narrow band is determined by the difference of that of two broad bands.

Band	DN		Energy* [keV]		Wavelength* [nm]		$NB_i = BB_i - BB_{i+1} = \frac{\sum s_{m_i}}{f_i} - \frac{\sum s_{m_{i+1}}}{f_{i+1}}$	%	Note
i	min	max	From	To	From	To			
1	7000	16383	62.76	146.89	8.4e-3	2.0e-2	$\frac{\sum p_{15-16383}}{f_1} - \frac{\sum p_{15-6999}}{f_2}$	**	p
2	6000	6999	53.80	62.76	2.0e-2	2.3e-2	$\frac{\sum p_{15-6999}}{f_2} - \frac{\sum p_{15-5999}}{f_3}$	**	p
3	5000	5999	44.83	53.80	2.3e-2	2.8e-2	$\frac{\sum p_{15-5999}}{f_3} - \frac{\sum p_{15-4999}}{f_4}$	**	p
4	4000	4999	35.86	44.83	2.8e-2	3.5e-2	$\frac{\sum p_{15-4999}}{f_4} - \frac{\sum p_{15-3999}}{f_5}$	**	p
5	3000	3999	26.90	35.86	3.5e-2	4.6e-2	$\frac{\sum p_{15-3999}}{f_5} - \frac{\sum p_{15-2999}}{f_6}$	**	p
6	2000	2999	17.93	26.90	4.6e-2	6.9e-2	$\frac{\sum p_{15-2999}}{f_6} - \frac{\sum p_{15-1999}}{f_7}$	**	p, f
7	1000	1999	8.97	17.93	6.9e-2	1.4e-1	$\frac{\sum p_{15-1999}}{f_7} - \frac{\sum p_{15-999}}{f_8}$	**	f
8	500	999	4.48	8.97	1.4e-1	2.8e-1	$\frac{\sum p_{15-999}}{f_8} - \frac{\sum p_{15-499}}{f_9}$	**	f
9	400	499	3.59	4.48	2.8e-1	3.5e-1	$\frac{\sum p_{15-499}}{f_9} - \frac{\sum p_{15-399}}{f_{10}}$	**	
10	300	399	2.69	3.59	3.5e-1	4.6e-1	$\frac{\sum p_{15-399}}{f_{10}} - \frac{\sum p_{15-299}}{f_{11}}$	~10^{-3}	
11	200	299	1.79	2.69	4.6e-1	6.9e-1	$\frac{\sum p_{15-299}}{f_{11}} - \frac{\sum p_{15-199}}{f_{12}}$	0.1	
12	100	199	0.90	1.79	6.9e-1	1.4	$\frac{\sum p_{15-199}}{f_{12}} - \frac{\sum p_{15-99}}{f_{13}}$	2.1	
13	50	99	0.45	0.90	1.38	2.77	$\frac{\sum p_{15-99}}{f_{13}} - \frac{\sum p_{15-49}}{f_{14}}$	24.6	
14	20	49	0.18	0.45	2.77	6.91	$\frac{\sum p_{15-49}}{f_{14}} - \frac{\sum p_{15-19}}{f_{15}}$	73.0	
15	15	19	0.13	0.18	6.91	9.22	$\frac{\sum p_{15-19}}{f_{16}}$		

*The conversion from DN to energy and wavelength is performed under the assumption that energy of a photon is completely absorbed by a pixel.

**Fraction is too small to be accurately accounted for due to model constrains.

3.3.3 Two-component Method

Solar irradiance is known to have different degrees of variability at different wavelengths as the solar flux originates at various regions in the solar atmosphere: factors of hundreds in hard X-ray, tens in soft X-ray, and 2 in EUV [Woods et al., 2004]. Solar models and proxies are often built acknowledging the difference in variability. For instance, the flare component is modeled separately and added to the daily background irradiance in the Flare Irradiance Spectral Model [Chamberlin et al., 2007, 2008] and a hot component (flare) is separated from the cold component (background) in the broadband measurements to construct a proxy for GOES XRS [Hock et al., 2013]. Therefore, the assumption of one single solar component in the SAM measurements as profiled in Equation 4 varying with F10.7 is likely not sophisticated enough though it is shown to remove some particle contamination as the first step. Two components, quiet s_q and active s_a, forming the solar term, $I_{s,2\text{-}comp}$ are introduced to represent the variability of quiet and active solar irradiance respectively as in Equation 6.

$$I_r = I_{s,2-comp} + s_{p,2-comp} = I_q + I_a + s_{p,2-comp} \tag{3.6}$$

Bands 1–6 still represent the particle term here as in the one-component method. In the process of building key criteria the GOES 1–8 Å is the main data set that will be compared to and based on for flaring condition since it is the channel NOAA currently uses to classify flares. The shortest-wavelength bands (up to band 6) within the narrow wavelength range of 0.5 Å have similarly high correlation with the GOES irradiance likely because they belong to similar groups of emissions. High correlation with GOES is the reason why bands 6–8 are selected to characterize the variability of the active component in solar irradiance and substitute for I_a at the right side of Equation 6 with a coefficient *B*. Bands are marked with *'p'* and *'f'* in Table 1 to indicate their roles in the analysis.

Similarly, in the *two-component* method Equation 6 is rewritten into Equation 7 with terms substituted by broadband and narrowband measurements.

$$I_{BB} = I_q + B \cdot I_{NB_{6-8}} + A \cdot I_{NB_{1-6}} \tag{3.7}$$

The inclusion of band 6 in both active and particle terms allows it to contribute as a particle channel but reserve its accountability for solar photons during flares. A 2D search grid is performed to find the optimal combination of *A* and *B* which result in the maximal correlation between I_q and F10.7. The two-component approach gives A of 1.08, B of 0.86, and the highest correlation found between I_q and F10.7 index is 0.88. Results of the one-component and two-component methods are listed in Table 2.

Table 3.2. Values of A and B are obtained by maximizing correlation between solar components with F10.7.

Method	1-component		2-component		
Coefficient	A	Correlation. of $s_{s,1\text{-comp}}$ with F10.7	A	B	Correlation of s_q with F10.7
Value	1.52	0.86	1.08	0.86	0.88

Both methods estimate the amount of particle contribution to be removed by obtaining maximal correlation between the solar components (the quiet component in two-component case) with F10.7 and reserving their products with the coefficients *A and B*. The higher value A and B, the lower contribution are due to particles. With only one term representing the solar contribution in the received signal, the one-component estimate of irradiance, $I_{s,1\text{-}comp}$, consists of both quiet and active parts of the true solar irradiance. On the other hand, the two-component method produces a quiet component, I_q, and an active component, I_a, which together construct the estimate of broadband irradiance, $I_{s,2\text{-}comp}$. It is worth noting here that $I_{s,2\text{-}comp}$ is not necessarily equal to $I_{s,1\text{-}}$

$_{comp}$. Different values of *A* are found in these two approaches: 1.52 for the one-component case and 1.08 for the two-component case; hence, the magnitude of the signal subtracted from the raw data is higher in one-component method than in two-component method. Even though higher level of particle contribution, I_p, is subtracted in the one-component case, the resulting solar irradiance, $I_{s,1\text{-}comp}$, is not as quiet as the quiet component, I_q, obtained using two-component method as depicted in the top left panel in Figure 3.7. The slope of the dashed line in the plot is one. The benefits of including an active term in the two-component approach are: 1) it takes back certain fraction of the raw signal that is taken away as particle contribution by the one-component approach and preserves the highly variable portion of the irradiance during flares; 2) it also results in a quieter component, I_q, that is closer to the particle-free condition than $I_{s,1\text{-}comp}$. On the other hand, the one-component irradiance, $I_{s,1\text{-}comp}$, contains both quiet and active parts of the solar irradiance though it does not fully capture as high irradiance on the active days nor reach as low at quiet conditions. These two estimates of the solar irradiance are compared using the quantity, *D*, defined in Equation 3.8. In the top right panel of Figure 3.7, this difference of $I_{s,2\text{-}comp}$ from $I_{s,1\text{-}comp}$ shows that solar irradiance can be either over-estimated by the two-component method or under-estimated by the one-component method at low solar activities (F10.7 < 100).

$$D = \frac{\left(I_{s,2-comp} - I_{s,1-comp}\right)}{I_{s,1-comp}} = \frac{\left(I_q + I_a - I_{s,1-comp}\right)}{I_{s,1-comp}} \tag{3.8}$$

In the comparison with the GOES level, variability of $I_{s,1\text{-}comp}$ scatters and even falls back down to lower than 2 at high solar activity level while it is not expected to (bottom left panel of Figure 3.7) and that of $I_{s,2\text{-}comp}$ is higher even with no apparent X-ray activities (bottom right panel). This reveals the possible issue of underestimation by the one-component method at high solar activities (GOES > 1e-6) and overestimation by the two-component method at low solar activities (GOES

< 1e-6). Therefore, we hypothesize that one-component estimate of solar irradiance should be adopted during lower solar activities and two-component estimate during higher solar activities.

3.3.4 A Hybrid Method

It has been shown that the one-component (two-component) method provides better broadband estimate at lower (higher) activities. The nonlinearity of the SAM data counts with respect to GOES 1–8 nm measurements is also presented in [Hock et al., 2013]. A hybrid approach has to take place to determine the set of coefficients, *A* or *A/B*, to be applied to the measurements according to the solar activity level so that the one-component coefficient is used on lower-activity days and the two-component coefficients for higher-activity days. Criteria of estimating solar activity level need to be established to help the program decide which sets of parameters to be applied and implemented in the future data production so that the broadband irradiance can be retrieved solely upon the SAM data in the entire process. Relationship of several quantities and the GOES X-ray irradiance are therefore examined. These include: a) one-component estimate, $I_{s,1\text{-}comp}$, b) quiet component, I_q, from two-component method, c) difference between $I_{s,1\text{-}comp}$ and I_q, the components upon which the correlation coefficients are calculated, d) daily mean (Mean) of the active component, I_a, e) standard deviation (Stddev) of the active component, and f) degree of variation defined as the ratio of standard deviation to mean of the active component. In Figure 3.8, four quadrants are defined in four panels as those quantities increase with the GOES level. Thresholds (dashed lines) are set to capture the C-class flares and above in the first quadrant, where the two-component coefficients are to be applied to the data of those flaring days. Data points falling in the fourth quadrant indicate the active day that will not get recognized and those falling

in the second quadrant are identified as the active days while GOES shows lower X-ray irradiance. All of the quantities that are examined except the variability of I_a generally serve as good indicators for solar activity level and with slight differences each misses less than 5 flaring days. The criterion based on standard deviation of the active component is the best among all selected to be utilized in the process. When the standard deviation of I_a is greater than 5×10^{-4}, a day is considered active and the two-component coefficients are employed. Otherwise, the one-component estimate is provided. Four years of the broadband derived from the SAM images are compared to the ESP irradiance in Figure 3.9. Hourly average of irradiance is shown with dots and daily average with asterisks in panel (a). The green squares indicate the days considered as active by the criteria and the 2-component coefficients are applied. The diamonds are color-coded to indicate the flare strength on the particular days: C class in blue, M class in orange, and above X class in red. The daily soft X-ray irradiance does not necessarily correlate with the GOES flare class, which is defined as the peak value of its one-minute measurements within one day span. The scatter plot in panel (b) shows that the ratio of the SAM to ESP irradiance is not a function of the ESP irradiance. The use of the 2010–2014 data as an entire data set implicitly emphasizes more on the variability of active component but particle contribution (one quiet year versus three active years). Therefore, the estimated SAM irradiance is higher (a factor of 2) than the ESP value in 2010. This effect is also seen from the difference between the coefficients obtained for the individual years and all four years in Figure 3.6. Overall, the SAM/ESP ratio from 2010 to 2014 is close to one. Of all the 31,848 hours studied, the SAM/ESP ratio has a mean of 1.07 and a standard deviation of 0.28. Orange shades beneath the black curve in panel (c) mark the days considered active by the procedure. Clearly the criteria based on the active component has successfully identified the flare days and the procedure properly applies the better set of the coefficients to estimate the irradiance.

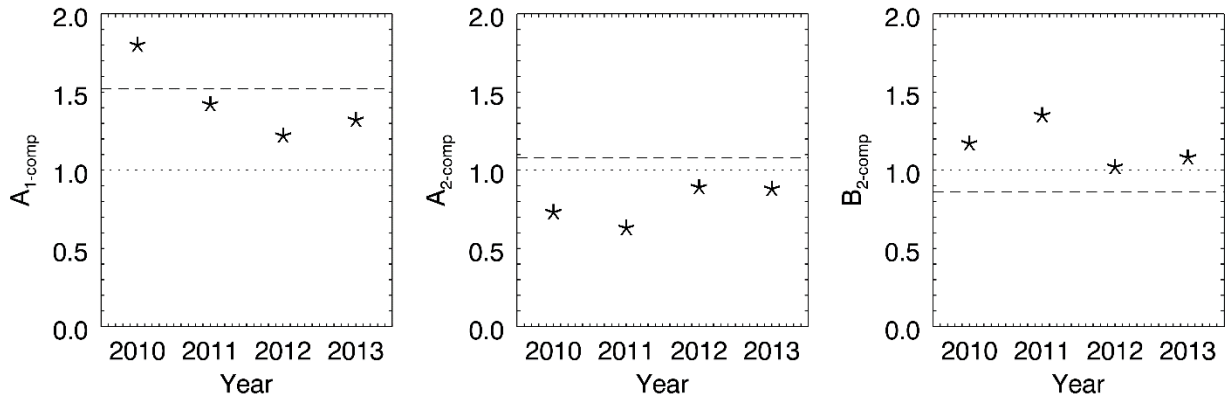

Figure 3.6. The one-component estimates of coefficient *A* (left) are greater than unity (thin dash) for all individual years while the two-component ones (middle) are less than unity with the introduction of coefficient *B* (right). Year 2010 is the only year whose one-component estimate of *A* is greater than the four-year estimate (thick dash).

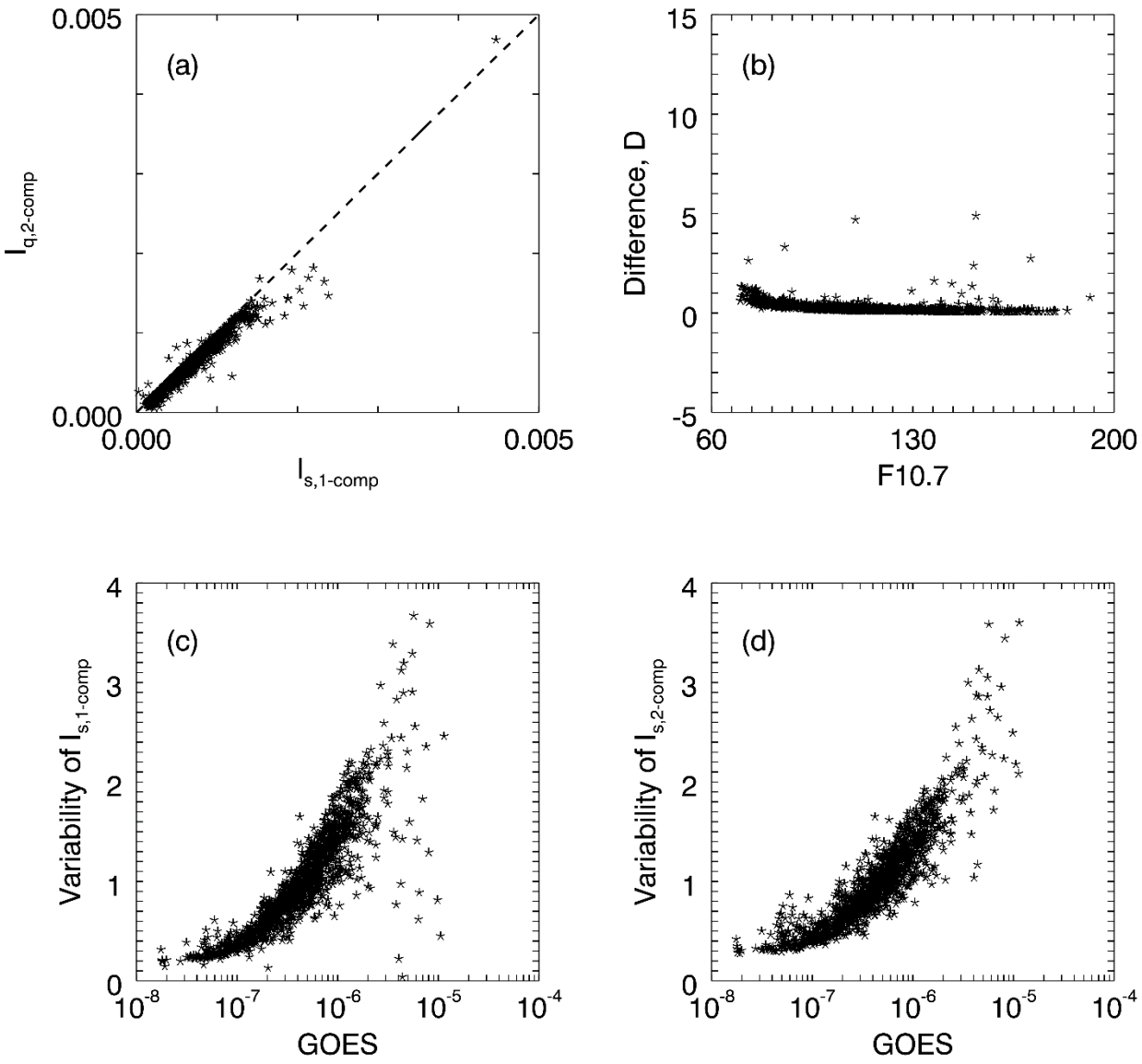

Figure 3.7. Comparison of products of the one-component and two-component methods. Two-component method provides two solar terms, I_q and I_a, whereas one-component method produces only one solar component, I_s, which contains partial irradiance of the active Sun and is higher than that of the two-component quiet irradiance as shown in panel (a). In panel (b), the difference between the one-component and two-component estimates is higher at low solar activities (F10.7 < 100). While compared with the GOES level, variability of $I_{s,1\text{-}comp}$ scatters and even falls back down to lower than 2 at high solar activity level as shown in panel (c) and that of $I_{s,2\text{-}comp}$ is higher even without apparent X-ray activities in panel (d).

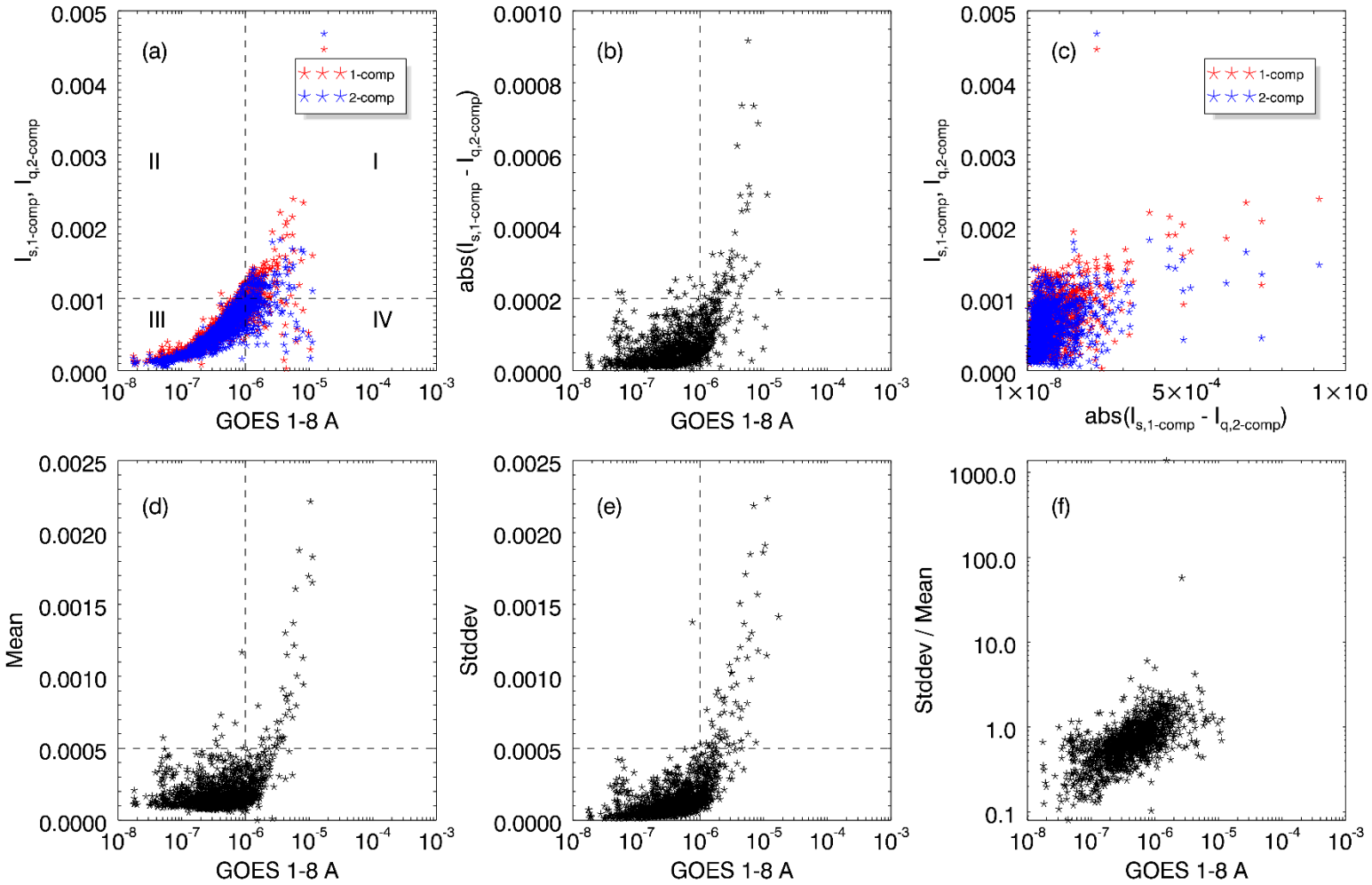

Figure 3.8. Relationship of several quantities and the GOES XRS irradiance is examined to help determine the criteria for applying proper sets of coefficients. Quantities examined include: extracted solar component, I_s, from one-component method (red) and quiet-Sun component, I_q, from two-component method (blue) shown in panel (a); difference between the two in panel (b); daily mean of the active component, I_a, as in Equation 4 in panel (d); 5) standard deviation of I_a in panel (e), and degree of variation defined as its ratio of standard deviation to mean of in panel (f). The quieter components has little correlation with the difference between each other as shown in panel (c). Four quadrants are defined by two dashed lines in the comparison with the GOES X-ray data. The right-hand side of the vertical line indicates C-class and above flares. The horizontal line is determined to define the first quadrant being able to capture the flare condition when two-component coefficients should be applied.

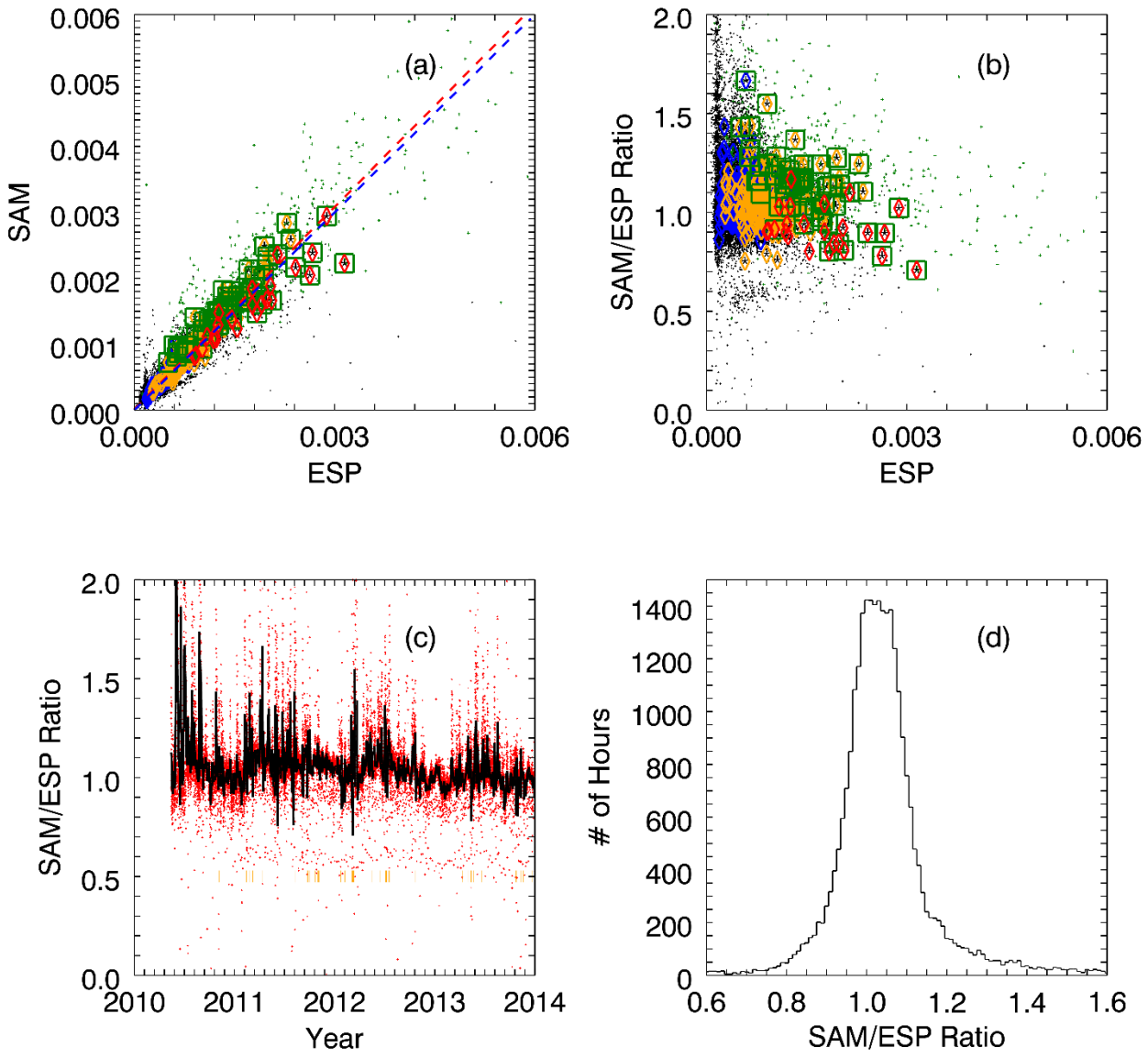

Figure 3.9. Comparison of broadband irradiance from SAM and ESP is illustrated. (a) Hourly irradiance is shown with dots and daily mean with asterisks. The green squares indicate the days recognized as active and the 2-component coefficients are applied. The diamonds are color-coded to indicate the flare strength on the particular days: C class in blue, M class in orange, and X class in red. The daily soft X-ray irradiance does not necessarily correlate with the GOES flare class, which is defined as the peak value of its one-minute measurements within one day span. Data points are fitted with a line (red), which is close to the X = Y line (blue). (b) The scatter plot shows that the ratio of the SAM to ESP irradiance is not a function of the ESP irradiance. (c) The hourly (red dots) and daily (black) ratio from 2010 to 2014 is close to one. When standard deviation of s_a reaches 5×10^{-4}, a day is considered active. Orange shades mark those days beneath the daily curve. (d) Of all the 31,848 hours studied, the SAM/ESP ratio has a mean of 1.07 and a standard deviation of 0.28.

Several sources contribute to the uncertainties in the proposed approaches. The DN cut-off between two bands implicitly assumes that the corresponding DN at both ends of the range of interest is contributed by one photon while using the reference spectrum to determine the scaling factors. As broad bands are selected to mitigate this issue, the effect is insignificant as the difference among scaling factors is less than a fraction of one tenth percent from the average for the bands used in the analysis. The major uncertainties come from obtaining values of A and B through correlating one solar component with the F10.7 index in the process of particle contamination removal. They can be estimated by performing the same analysis on each year's data, which maximally changes the value of A by 20% and 50% in the one-component case and the value of B by 55%. The most deviated values of A and B obtained from the one-year data from those obtained from the four-year data occur when the one-component method is performed on the most active year (2011) and the two-component method is performed on the quietest year (2010). This is expected as it is pointed out that the two-component method provides better estimate at the high solar activity levels and the one-component method at the low solar activity levels. Overall, the changes of the values of A and B can vary the irradiance product by 30% and 20% respectively in the one-component and two-component cases. The estimate of these uncertainties is compromised to 27% with the introduction of the hybrid method. The rest of the uncertainty sources including thermal noise and dark counts total about 3 DN, which is considered negligible to the end irradiance estimate.

3.3.5 Broadband Irradiance of 2014

The procedure of retrieving broadband solar soft X-ray irradiance from the SAM images has been demonstrated and the comparison with the ESP irradiance shows good agreement regardless of solar activity levels. The key coefficients established from the analysis are listed in Table 3.2 and are performed on the data of the first seventy days of 2014 to estimate hourly soft X-ray irradiance on a day-to-day basis. Solar activity level is judged by the estimated value of Equation 9c. On the lower activity days ($I_a^* < 5 \times 10^{-4}$), the estimate irradiance takes the value of $I_{s,1-comp}^*$; on the higher activity days ($I_a^* \geq 5 \times 10^{-4}$), it takes the 2-component estimate, $I_{s,2-comp}^*$, instead. The estimated quantities that the parameters in Table 3 are applied to are marked with asterisks to distinguish from those obtained during data analysis. Currently broadband irradiance is produced daily by these principles in one-hour and one-day cadence.

$$I_{s,1-comp}^* = I_{BB} - A_{1-comp} \cdot I_{NB1-6} \text{ (when } I_a^* < 5 \times 10^{-4}) \quad (3.9a)$$

$$I_{s,2-comp}^* = I_{BB} - A_{2-comp} \cdot I_{NB1-6} \text{ (when } I_a^* \geq 5 \times 10^{-4}) \quad (3.9b)$$

$$I_a^* = B \cdot I_{NB6-8} \quad (3.9c)$$

The broadband irradiance from the SAM images of the first seventy days of 2014 is processed based on the parameters we established and all the decision-making is performed solely based on the SAM data. The results are compared with the ESP measurement in Figures 3.10 and 3.11. The orange bars at the bottom of Figure 3.10 indicate the days when the criteria of high solar activities are reached. Two sets of dashed lines indicate the 25% (inner) and 50% (outer) difference between the SAM and ESP irradiance are drawn in Figure 3.11. The green squares indicate the flaring days recognized by the procedure when the standard deviation of the active solar component is above 5×10^{-4} W/m^2. Most of the data points reside in the 25% region.

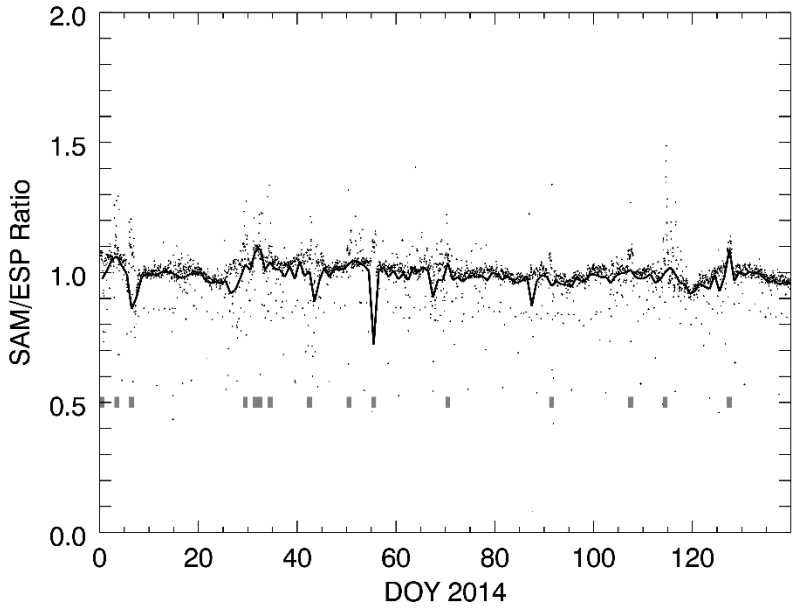

Figure 3.10. The broadband irradiance from the SAM images of the first seventy days of 2014 is processed using the parameters learned from the four-year data. All the criteria are determined solely on the SAM data. The orange bars at the bottom indicate the days when the criteria of high solar activities are reached.

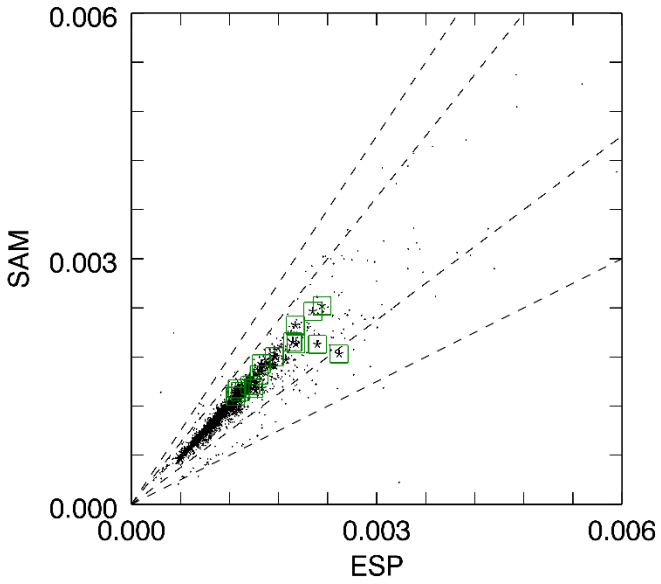

Figure 3.11. Estimated daily (asterisk) and hourly (dot) irradiance for the first seventy days of 2014 is presented. Two sets of dashed lines indicate the 25% (inner) and 50% (outer) difference between the SAM and ESP irradiance. Green squares indicate the days recognized as active ones by the procedure. Most of the data points reside within the 25% region. The hybrid approach successfully recognizes the active days and the 2-component coefficients are applied to improve the estimated irradiance that would otherwise falls outside of the 25% region.

3.4 Summary and Conclusions

By treating an array of CCD pixels as a collective photon detector, it is shown possible to determine the broadband solar soft X-ray irradiance with the SAM images. Two slices of the SAM images, marked as *light* and *dark*, are used in the analysis for the sunlit and non-sunlit areas of the image. The difference of the light and dark histograms is integrated and converted to raw broadband signal. The one-component method uses a single solar term to represent the solar contribution in the raw signal while the two-component method adepts a quiet and an active solar terms. Fifteen SAM narrow bands are defined and several of them are selected as the particle or flare indicators. The coefficients associated to the particle and solar terms are estimated through a process searching for the highest correlation between the relatively quiet component and F10.7. The one-component estimate of the irradiance does better at lower solar activities while the two-component estimate is better at higher solar activities. A criterion based on the level of the extracted active solar component is therefore set as an indicator to help select either the one-component or two-component irradiance according to the estimated solar activity level. The resulting parameters and criteria from the first four years of data are then applied to the 2014 data and no measurements from other instruments are required further on. The comparison of the 2014 SAM and ESP irradiance shows good agreement within 25% under all solar conditions.

History of broadband solar soft X-ray measurements are presented in Figure 3.12 with SNOE (1998–2003), SOHO/SEM (1996–present), TIME/SEE (2002–present), SDO/EVE/SAM (2010–present), and SDO/EVE/ESP (2010–present). The SOHO/SEM soft X-ray irradiance is interpreted from its broadband measurement between 0.1 to 50 nm [Wieman, personal communication]. Though SAM and ESP are fundamentally different types of instruments, we have

shown that the broadband soft X-ray irradiance derived from the SAM images agree with the ESP quad-diode measurements within 25%. It is clearly that SAM as an imager is also a valid solar irradiance monitor in soft X-ray. The latency for the data production is one day and the cadence of the broadband product can be as short as 10 s. The estimate of broadband soft X-ray irradiance may be further improved by implementation of more sophisticated estimators taking the parameters determined in this paper and updating them with new measurements.

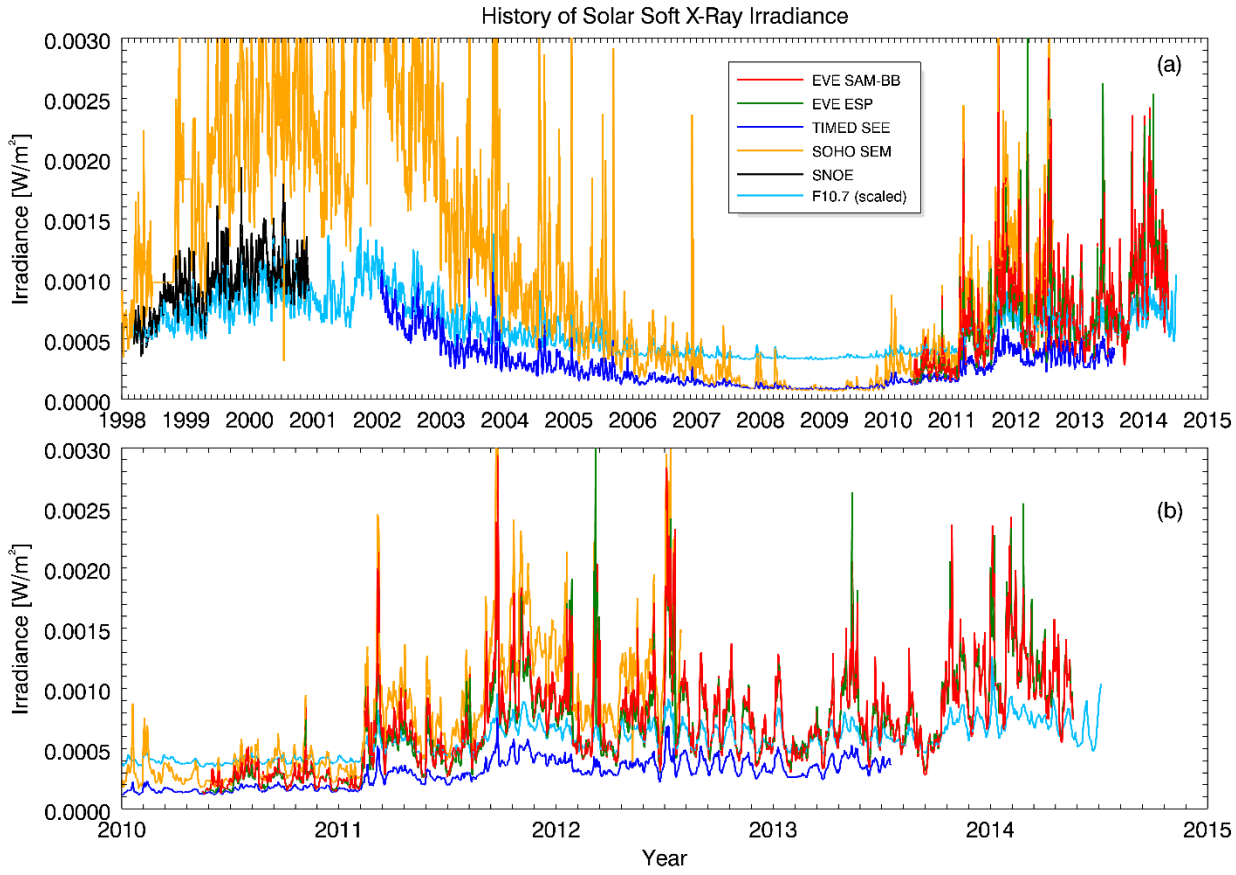

Figure 3.12. Time series of solar soft X-ray measurements and the scaled F10.7 index from 1998 (a) and from the beginning of the SDO mission (b) to present. During the second half of 2012, the Sun turns quiet and therefore the solar irradiance shows clear modulation of its 27-day rotation.

References

Acton, L. W., J. L., Culhane, A. H. Gabriel, R. D. Bentley, J. A. Bowles, J. G. Firth, M. L. Finch, C. W. Gilbreth, P. Guttridge, R. W. Hayes, E. G. Joki, B. B. Jones, B. J. Kent, J. W. Leibacher, R. A. Nobles, T. J. Patrick, K. J. H. Phillips, C. G. Rapley, P. H. Sheather, J. C. Sherman, J. P. Stark, L. A. Springer, R. F. Turner, and C. J. Wolfson, "The soft X-ray polychromator for the Solar Maximum Mission," Solar Physics, 1980

Acton, L. W., D. C. Weston, M. E. Bruner, "Deriving solar X-ray irradiance from Yohkoh observations," Journal of Geophysical Research, 104, 1999

Bailey, S. M., T. N. Woods, C. A. Barth, and S. C. Solomon, "Measurements of the solar soft x-ray irradiance from the Student Nitric Oxide Explorer," Geophysical Research Letters, 26, 9, 1999

Bailey, S. M., C. A. Barth, and S. C. Solomon, "A model of nitric oxide in the lower thermosphere," Journal of Geophysical Research, 107(A8), doi:10.1029/2001JA000258, 2002.

Bailey S. M., T. N. Woods, F. G. Eparvier, and S. C. Solomon, "Observations of the solar soft X-ray irradiance by the student nitric oxide explorer," Advance in Space Res., 37, 2006

Barth, C. A., W. K. Tobiska, and D. E. Siskind, "Solar-terrestrial coupling: Low-latitude thermospheric nitric oxide," Geophysical Research Letters, 15, 1988

BenMoussa, A. et al., “On-orbit degradation of solar instruments,” Solar Phys, 2013

Bohlin, J. D., K. J. Frost, P. T. Burr, A. K. Guha, G. L. Withbroe, “Solar Maximum Mission,” Solar Physics, 1980

Chamberlin P. C., T. N. Woods, and F. G. Eparvier, “Flare Irradiance Spectral Model (FISM): Daily component algorithms and results,” Space Weather, 5, 2007

Chamberlin P. C., T. N. Woods, and F. G. Eparvier, “Flare Irradiance Spectral Model (FISM): Flare component algorithms and results,” Space Weather, 6, 2008

Chamberlin P. C., T. N. Woods, D. A. Crotser, F. G. Eparvier, R. A. Hock, and D. L. Woodraska, “Solar Cycle Minimum Measurements of the Solar Extreme Ultraviolet Spectral Irradiance on 14 April 2008,” Geophysical Research Letters, Vol. 36, 2009

Davis, J. E., “Event pileup in Charge-Coupled Devices,” Astrophysical Journal, Vol. 562, 2001

Dere, K. P., E. Landi, H. E. Mason, B. C. Monsignori Fossi, P. R. Young, “CHIANTI - An Atomic Database For Emission Lines - Paper I: Wavelengths greater than 50 Å,” Astronomy and Astrophysics Suppl. Ser., Vol. 125, 1997

Didkovsky, L., D. Judge, S. Wieman, and T.Woods, “EUV SpectroPhotometer (ESP) in Extreme Ultraviolet Variability Experiment (EVE): Algorithms and Calibrations,” Solar Physics, 2009

Emmert, J. T., J. L. Lean, and J. M. Picone, "Record-low thermospheric density during the 2008 solar minimum," Geophysical Research Letters, Vol. 37, 2010

Feng, W. H. S. Ogawa, and D. L. Judge, "The Absolute Solar Soft X Ray Flux in the 20–100 Å Region," J. Geophys. Res., 94, 9125, 1989

Fuller-Rowell, T., S. Solomon, R. Roble, and R. Viereck, "Impact of solar EUV, XUV, and X-ray variations on Earth's atmosphere," Solar Variability and its Effects on Climate, Geophysical Monograph 141, AGU, 2004

Gibson, S. J. and J. A. Van Allen, "correlation of X-ray radiation (2-12 A) with microwave radiation (10.7 centimeters) from the nonflaring Sun," Astrophysical Journal, 161, 1970

Golub, L., E. Deluca, G. Austin, J. Bookbinder, D. Caldwell, P. Cheimets, J. Cirtain, M. Cosmo, P. Reid, A. Sette, M. Weber, T. Sakao, R. Kano, K. Shibasaki, H. Hara, S. Tsuneta, K. Kumagai, T. Tamura, M. Shimojo, J. McCracken, J. Carpenter, H. Haight, R. Siler, E. Wright, J. Tucker, H. Rutledge, M. Barbera, G. Peres, and S. Varisco, S. "The X-Ray Telescope (XRT) for the Hinode Mission," Solar Physics, 243, 2007

Hall L. A. and H. E. Hinteregger, "Solar radiation in the EUV and its variation with solar rotation," Journal of Geophysical Research, 75, 1970

Hall, L. A., "Solar flares in the extreme ultraviolet," Solar Physics, 21, 1971

Henke, B. L., E. M. Gullikson, and J. C. Davis, "X-ray interactions: Photoabsorption, scattering, transmission, and reflection at E = 50-30,000 eV, Z = 1-92," Atomic Data and Nuclear Data Tables, 54, 1993

Hock, R. A., P. C. Chamberlin, T. N. Woods, D. Crotser, F. G. Eparvier, D. L. Woodraska, and E. C. Woods, "Extreme Ultraviolet Variability Experiment (EVE) Multiple EUV Grating Spectrograph (MEGS): Radiometric Calibrations and Results," Solar Phys., 2010

Hock R. A., D. Woodraska, and T. N. Woods, "Using SDO EVE data as a proxy for GOES XRS B 1–8 angstrom," Space Weather, 11, 2013

Judge, D. L., D. R. McMullin, H. S. Ogawa, D. Hovestadt, B. Klecker, and M. Hilchenbach, "First solar EUV irradiance obtained from SOHO by the CELIAS/SEM," Solar Phys., 177, 1998

Kano, R., T. Sakao, H. Hara, S. Tsuneta, K. Matsuzaki, K. Kumagai, M. Shimojo, K. Minesugi, K. Shibasaki, E. E. DeLuca, L. Golub, J. Bookbinder, D. Caldwell, P. Cheimets, J. Cirtain, E. Dennis, T. Kent, and M. Weber, "The Hinode X-Ray Telescope (XRT): Camera design, performance and operations," Solar Phys., 249, 2008

Ogawara, Y., L. W. Acton, R. D. Bentley, M. E. Brunder, J. L. Culhane, E. Hiei, T. Hirayama, H. Hudson, T. Kosugi, J. R. Lemen, "The status of YOHKOH in orbit - an introduction to the initial scientific results," Publications of the Astronomical Society of Japan, 1992

Ogawa, H. S., D. L. Judge, D. R. McMullin, P. Gangopadhyay, and A. B. Galvin, "First-year continuous solar EUV irradiance from SOHO by the CELIAS/SEM during 1996 solar minimum," Journal of Geophysical Research, Vol. 103, 1998

Richards, P. G., T. N. Woods, and W. K. Peterson, "HEUVAC: A new high resolution solar EUV proxy model," Advances in Space Research, 37, 2006

Royal Observatory of Belgium, Brussels, SILSO data, http://www.sidc.be/silso/home

Siskind, D. E., C. A. Barth, and D. D. Cleary, "The possible effect of solar soft X-rays on thermospheric nitric oxide," J. of Geophysical Research, 95, 1990

Sojka, J. J., C. Smithtro, R. W. Schunk, "Recent developments in ionosphere-thermosphere modeling with an emphasis on solar activity," Advance in Space Research, 37, 2006

Solomon S. C. and L. Qian, "Solar extreme-ultraviolet irradiance for general circulation models," Journal of Geophysical Research, Vol. 110, 2005

Solomon, S. C, "Numerical models of the E-region ionosphere," Advances in Space Res., 37, 2006

Tapping, K. F., "Recent solar radio astronomy at centimeter wavelengths: The temporal variability of the 10.7-cm flux," Journal of Geophysical Research, 92, 1987

Tapping, K. F., "The 10.7 cm solar radio flux ($F_{10.7}$)," Space Weather, 11, 2013

Tobiska, W. K., T. Woods, F. Eparvier, R. Viereck, L. Floyd, D. Bouwer, G. Rottman, O. R. White, "The SOLAR2000 empirical solar irradiance model and forecast tool," J. of Atmospheric and Solar-Terrestrial Physics, 62, 2000

Vaiana, G. S. et al., "ATM observations, X-ray results," Astrophysics and Space Science, 39, 1976

Warren, H. P., "A Solar Minimum Irradiance Spectrum for Wavelengths Below 1200 Å," Astrophysical Journal Supplement Series, Vol. 157, 2005

Wieman, S. R., personal communication at EVE SXR Working Group, 2013

Woods, T. N., G. J. Rottman, S. M. Bailey, S. C. Solomon, J. R. Worden, "Solar extreme ultraviolet irradiance measurements during solar cycle 22," Solar Physics, 1998

Woods, T. N., E. Rodgers, S. M. Bailey, F. G. Eparvier, and G. Ucker, "TIMED Solar EUV Experiment: pre-flight calibration results for the XUV Photometer System," SPIE, 3756, 1999

Woods, T. N., L. W. Acton, S. B. Bailey, F. Eparvier, H. Garcia, D. Judge, J. Lean, J. T. Mariska, D. McMullin, G. Schimidtke, S. C. Solomon, W. K. Tobiska, H. P. Warren, and R. Viereck, "Solar Extreme Ultraviolet and X-ray Irradiance Variations," Solar Variability and its Effects on Climate, Geophysical Monograph 141, AGU, 2004

Woods, T. N., P. C. Chamberlin, W. K. Peterson, R. R. Meier, P. G. Richards, D. J. Strickland, G. Lu, L. Qian, S. C. Solomon, B. A. Iijima, A. J. Mannucci, B. T. Tsurutani, "XUV Photometer System (XPS): Improved solar irradiance algorithm using CHIANTI spectral models," Solar Physics, 2008

Woods, T. N., P. C. Chamberlin, J. W. Harder, R. A. Hock, M. Snow, F. G. Eparvier, J. Fontenla, W. E. McClintock, and E. C. Richard, "Solar Irradiance Reference Spectra (SIRS) for the 2008 Whole Heliosphere Interval (WHI)," Geophysical Research Letters, Vol. 36, 2009

Woods, T.N., F.G. Eparvier, R. Hock, A.R. Jones, D. Woodraska, D. Judge, L. Didkovsky, J. Lean, J. Mariska, H. Warren, D. McMullin, P. Chamberlin, G. Berthiaume, S. Bailey, T. Fuller-Rowell, J. Sojka, W.K. Tobiska, and R. Viereck, "Extreme ultraviolet Variability Experiment (EVE) on the Solar Dynamics Observatory (SDO): Overview of science objectives, instrument design, data products, and model developments," Solar Physics, 2010

CHAPTER 4 Photon Event Detection on Images Taken by Solar Aspect Monitor

Chapter 3 validates the solar soft X-ray broadband irradiance derived from the SAM images. The next step is to detect single photon events from the images. This process may sound similar to feature detection in the field of image processing to some degree, but it is very different. Feature recognition generally requires a sizable array of image which has continuous edges [Aschwanden, 2005; Canny, 1986]. SAM is designed to be able to isolate energetic photons and therefore results in low data count rate at each frame. This makes photons appear on the images as isolated and random as particle hits. On the other hand, clusters of bright points are seen on the CCD when there are active regions on the solar disk. Yet, these pixels can either appear connected or isolated depending on the strength of the active regions on the Sun. The term, active region (AR), in heliophysics is an area with an especially strong magnetic field where sunspots usually collocate [Lites 2005; Tian and Alexander, 2006; Liu et al., 2013]. Active regions appear bright in soft X-ray [Teske and Mayfield, 1976] and are often associated with solar flares and coronal mass ejections (CME) [Cliver, 1995; Fletcher et al., 2011, Nitta and Hudson, 2001] which cause severe space weather and in turn impact spaceborne and ground applications [Cerruti et al., 2008; Chen et al., 2005]. In this dissertation, active regions are reserved to refer to certain sustaining active features of the solar atmosphere; features observed as a group of bright pixels on the SAM images during the data processing are described as active areas or simply bright pixels in this study. Bright pixels seen in the images may associate with active regions on the Sun or various parts of the solar atmosphere emitting in X-ray from time to time. In Section 4.4, a sophisticated method is introduced to determine active regions from observed bright pixels. Two 10-second frames are

shown in Figure 4.1 with the upper panel showing the quiet Sun on May 15, 2010 and the lower panel the active Sun on Jan 27, 2012. With images shown in both natural and logarithmic values, it is difficult to tell if a certain range of energy can be properly applied to discriminate particles from in-band photons (0.01 – 7 nm). Extracting information of interest from large data sets has become an important problem as modern technology grows with an unprecedentedly fast pace. Data mining and machine learning are often required in the scientific study to facilitate the visually intuitive recognition [Fayyad, 1996].

4.1 Event Detection

The first several steps of the photon-event detection (PED) technique are identical to what needs to be done for the BB technique, including dark correction and image rotation (pinhole image is 180 degree rotated by nature). The resulting raw image is then fed into the event-detection algorithm. A set of criteria screens every extracted event during the process and put the SAM photons on a clean image. The current scheme of PED is summarized in Figure 4.2. In the PED algorithm, an event is defined as an isolated area of connecting pixels, each of which has value above the background noise level (~5 DN) as discussed in Chapter 3. Based on this definition, events are often found of irregular shapes. The causes may include: 1) higher-than-expected noise level, 2) multiple photons, and 3) cascading effect of high-energy photons and particles. If the noise level is higher than expected, an event centered at a bright pixel can have wings or side lobes of moderate brightness. The projected solar disk is no more than a 200-by-200-pixel area on the detector and a CCD pixel resolves only about 15-arcsecond of the Sun. Photons from the same active region likely appear across several pixels up to 50 pixels if a big active region presents in

the solar atmosphere. However, owing to the rarity of soft X-ray photons and the chosen filter design and integration time, photons from a single solar feature are unlikely to arrive on the detector on the same frame, resulting spotty presence of bright events. In the event detection, an event box is defined by a rectangle that tightly embraces the entire event. Two techniques of event detection have been developed. One detects monotonically decreasing edges to separate an event apart; the other is based on nearest neighbor algorithm. Currently the nearest-neighbor detection is implemented in the PED process. Both techniques are introduced in the following sections.

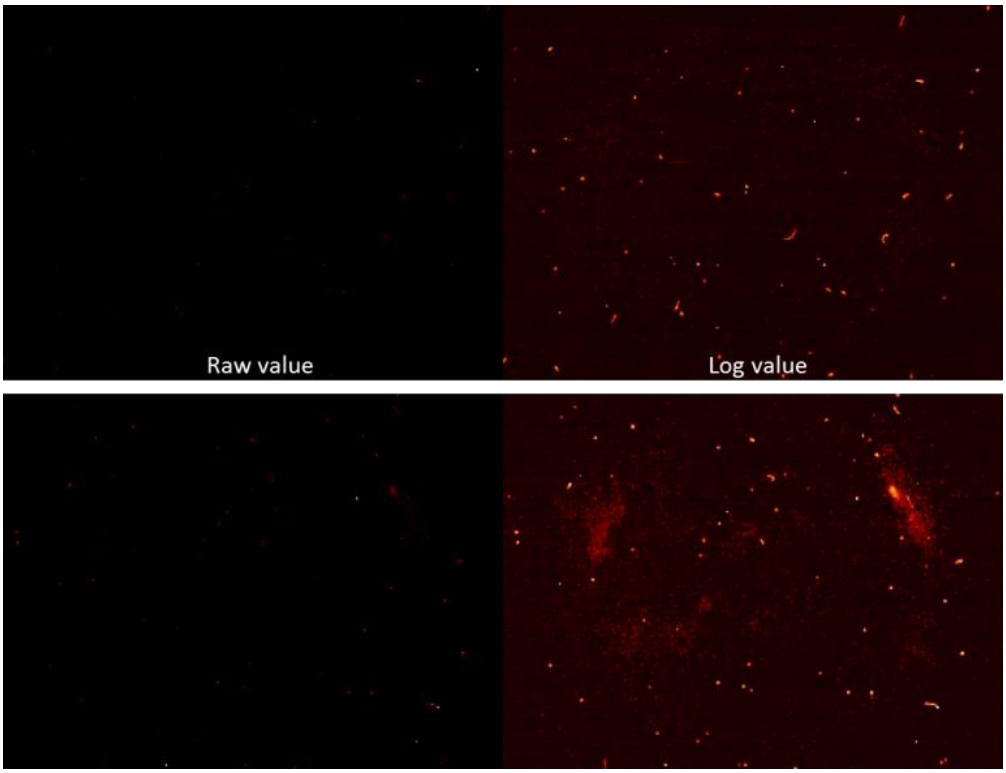

Figure 4.1. Images of the quiet (top) and the active (bottom) Sun in raw counts (left) and their logarithmic (right) value. The low-energy photons from out-of-band emission lines appear bright in the east limb, overlapping with the background atmosphere.

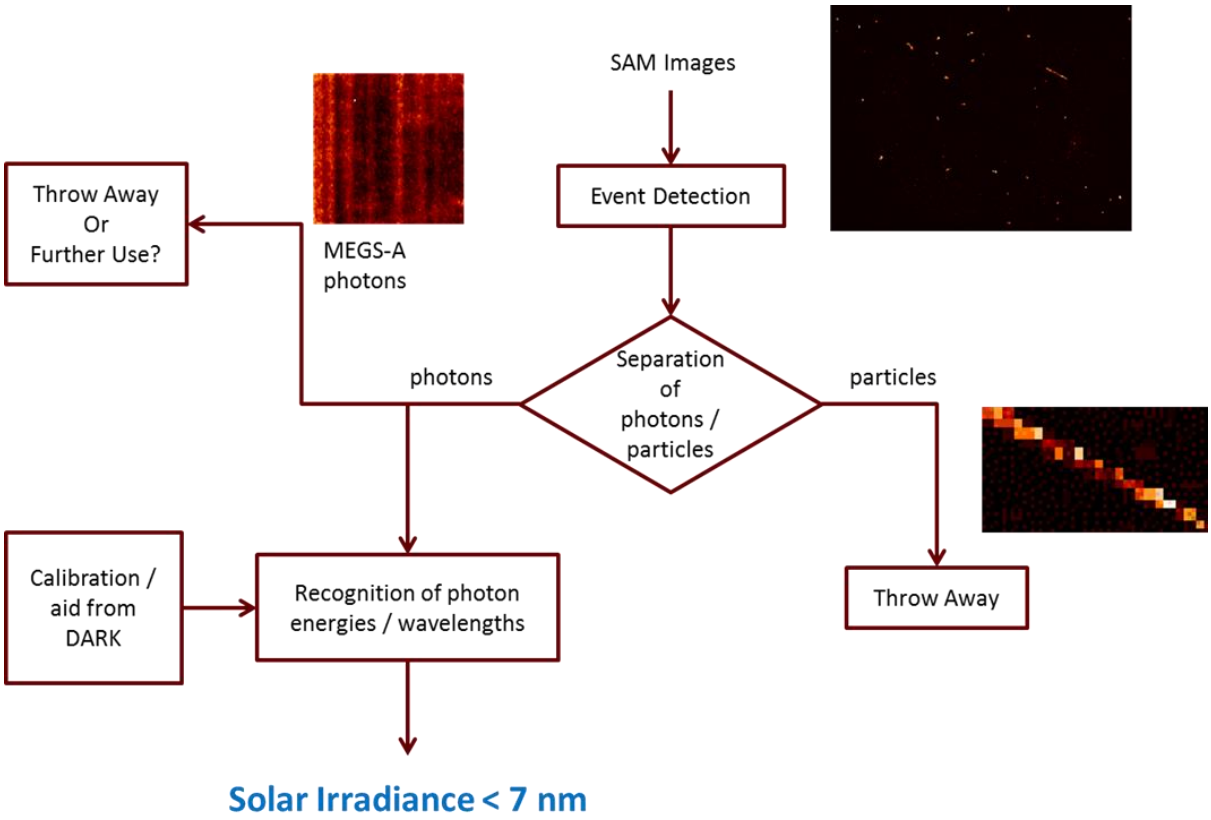

Figure 4.2. Block diagram of the PED procedures.

4.2 Monotonically Decreasing Edges

If a highly energetic photon impacts on the CCD and the energy is not completely absorbed by a pixel, its impact area may spread across several pixels; monotonically decreasing in intensity (DN) at adjacent pixels are expected to be observed. Based on this assumption, the detection algorithm starts from the brightest pixel of the image and an event box is defined by four decreasing edges in both positive and negative X and Y directions. The event box is then removed from the original image and planted on a new image which all the extracted events are to be collected. The detection continues until no more pixels of DN value higher than the noise level are left. Searching for monotonically decreasing edges is performed in positive and negative X and Y

directions rather than all slanted directions to facilitate program efficiency neglecting the fact that they likely exist in all directions on X-Y plane. When an event is found, the entire event box is extracted from the image rather than only the bright pixels. All DN values inside the box are accounted for the overall energy of the event. However, this technique falls short when 1) small isolated photon events appear on any quadrant assuming the peak is the origin and its X and Y axes sets the coordinates (an example is shown in Figure 4.3 and will be further explained in Section 4.3); or 2) impact areas of multiple photons are close enough that their 'wings' or 'side lobes' overlap. When these happen, total energy in one event box can either be overestimated or sometimes underestimated. This shortcoming leads to the development of a better detection method which is based on nearest neighbor search.

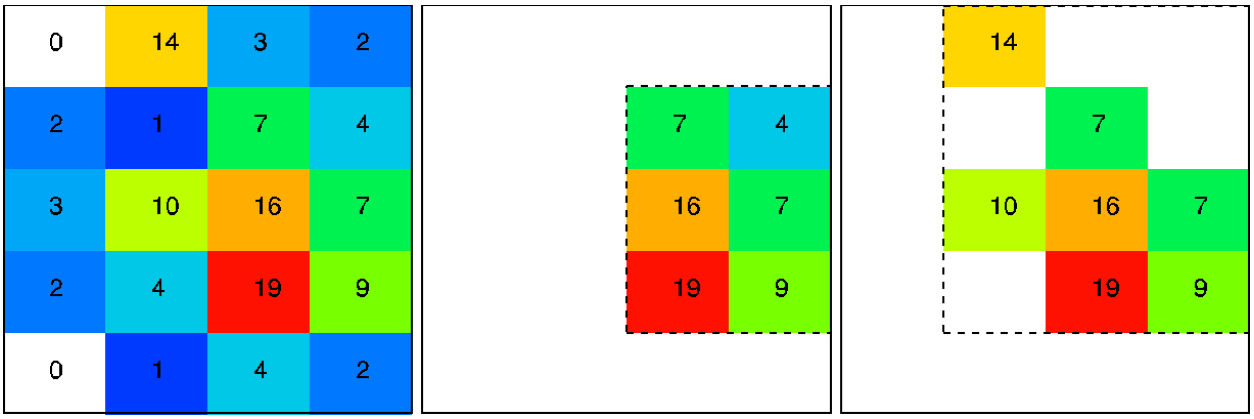

Figure 4.3. Demonstration of event detection techniques performed on a made-up image (left). The lowest detection limit is set to 5 DN. Detection of the monotonically decreasing edges (middle) produces a rectangular event box (dash), missing two off-center qualified pixels but including a low-intensity one. The event detected by the nearest neighbor search, enclosed by event box (right), contains 7 pixels out of the 12-pixel event box corresponding to an occupancy rate of 58%. The brightest pixel falls on the edge of the event box and therefore the event is treated as a particle. Total DN is 62 using the edge detection and 82 using the nearest-neighbor detection.

4.3 Nearest Neighbor Search

Nearest neighbor algorithm was among several proposed algorithms for solving the travelling salesman problem, an optimization problem that seeks for the shortest route allowing a salesman to visit each city exactly once and return to the origin city. In the nearest neighbor algorithm, the salesman starts at a random city and visits the nearest cities until all has been visited [Arya et al., 1998; Fayyad, 1996]. We improved the event detection by adopting the nearest-neighbor concept. For each image, the event detection starts from the brightest pixel, from which the algorithm searches all its eight surrounding pixels (neighbors). If a neighboring pixel has a DN value within the valid range, it is marked as part of the event. The default value of the valid range has lower limit of 5 DN and the upper limit of 2,000 DN. The search switch to each qualified neighbor and continues visiting their individual neighbors following the same principles but skips the pixels previously visited. This recursive search creates a map of all qualified neighbors and an isolated event. The event is extracted from the raw image and fed to the photon/particle filters (Section 4.4). The filters are specifically designed for the events detected with nearest-neighbor search to separate photons from particles. A qualified photon event is then planted on a new blank image. The detection continues extracting events from the raw image until no more pixels of DN value higher than the noise level are left.

The difference between the monotonically decreasing edges and the nearest neighbor search is demonstrated in Figure 4.3. Two techniques are performed on a made-up image array. In the middle panel, detection of the monotonically decreasing edges produces a rectangular event box, missing two off-center qualified pixels but including an unqualified one. Shown in the right, the event detected by the nearest neighbor search, enclosed by event box, contains 7 pixels out of

the 12-pixel event box corresponding to an occupancy rate of 58%. The total DN is 62 using the edge detection and 82 using the nearest-neighbor detection.

4.4 Photon/Particle Filters

The filtering rules separating photons from particles are designed based on studies of the particle appearance on the raw images. Figure 4.4 shows examples of particle strikes and ambiguous features. Based on these observations, particle events have 1) high-intensity peak, 2) low occupancy, 3) far-from-one aspect ratio, or 4) its peak happening at one of the four edges. With the nearest-neighbor search, an event can be detected as any shape and therefore does not necessarily occupy the same number of pixels as those inside the event box. High-intensity-peak filter screens out the event whose peak is too high. The percentage of occupancy is defined as the ratio of the number of pixels occupied by the event over that inside the event box. A low percentage indicates some particle-like shape of the event, such as a line of finite angle with respect to X or Y axis. A straight strike at X or Y direction can however pass this filter. The aspect ratio of an event box far from one or the peak of it falling at one of the edges of the box can be a signature of a particle. The filtering rules are summarized in Table 4.1. Any event satisfying one of the rules is considered as a particle and therefore discarded from the image. As an example, the event shown in the right panel of Figure 4.3 has its brightest pixel falling on the edge of the event box and therefore the event is treated as a particle. In this case, one may argue that the pixel of 14 is unlikely to be due to the same photon impact as the rest of the pixels but could have come from a separate photon. This leads to the issue of photon pileups to be addressed later in the chapter. Each of the four rules is customizable to be switched on or off upon running the PED algorithm. Applying all

of the rules often results in missing 50% photons at around active regions; if otherwise, it often leaves a noisier background. This suggests that rules are to be applied differently depending on where events are detected such as looser rules at active regions and more strict rules for quiet atmosphere.

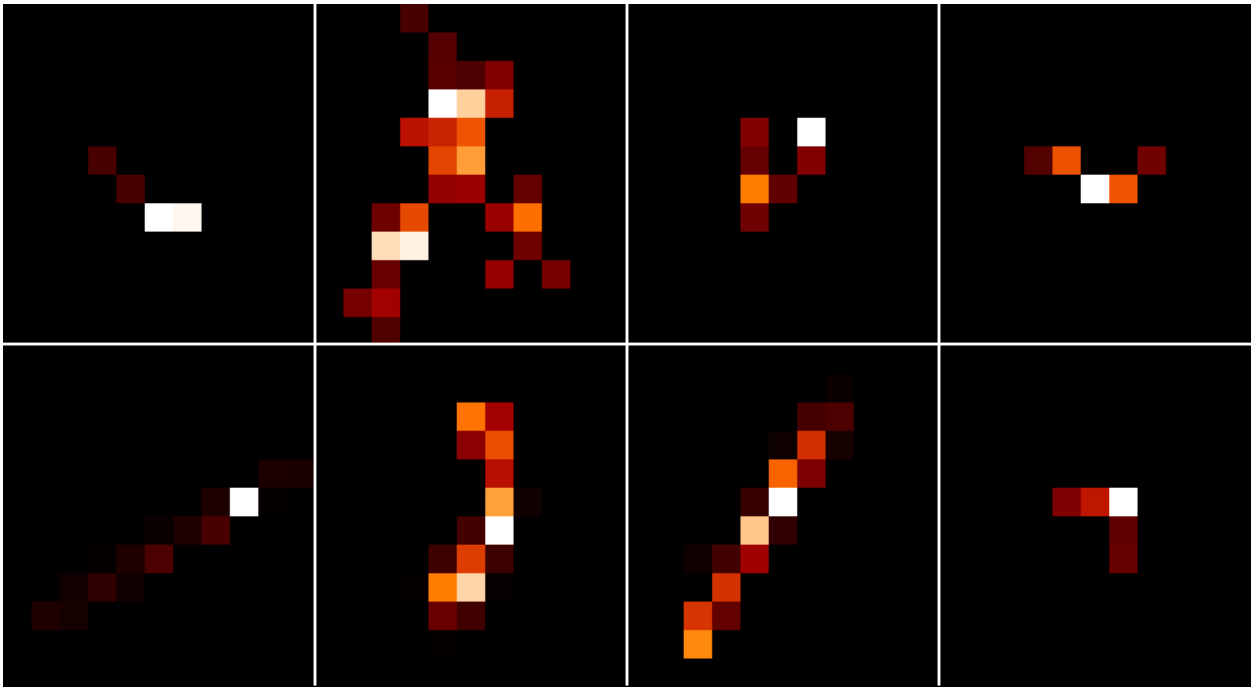

Figure 4.4. Examples of particle strikes and ambiguous features. The white pixels have the highest DN in each case.

Table 4.1 Filtering rules for particles. Each of the four rules is customizable to be switched on or off upon running the PED algorithm.

Filter	Rule to be considered as a particle
High-intensity peak	> 2,000 DN
Low occupancy	< 50%
Aspect ratio	far from 1, width difference in X and Y > 3
Peak location	Peak falls on one of the edges of the event box

4.5 Active Region Detection

A sudden bright circular feature as shown in Figure 4.5 is often observed centered at an active region during flare time. This is caused by sudden increase of the highly energetic hard X-ray photons penetrating through the outer BeCu filter which makes the pinhole. If simply applying all the particle filters listed in Table 4.1, the extracted photon events in this circular area had about 50% chance to be mistreated as particles by the screening process due to either their contributing higher DN values or photon pileups that happens to fulfill one of the rules set for particles. The Apertural Progression Procedure for Light Estimate (APPLE) is developed as a completely separate procedure to study the evolution of irradiance in up to two active regions starting by tracking the two brightest separated pixels from image to image. The APPLE algorithm creates two masks with radii of 5 and 25 pixels respectively around the brightest pixels. The inner area is defined as *core* and the outer ring as *apple* as shown in Figure 4.5.

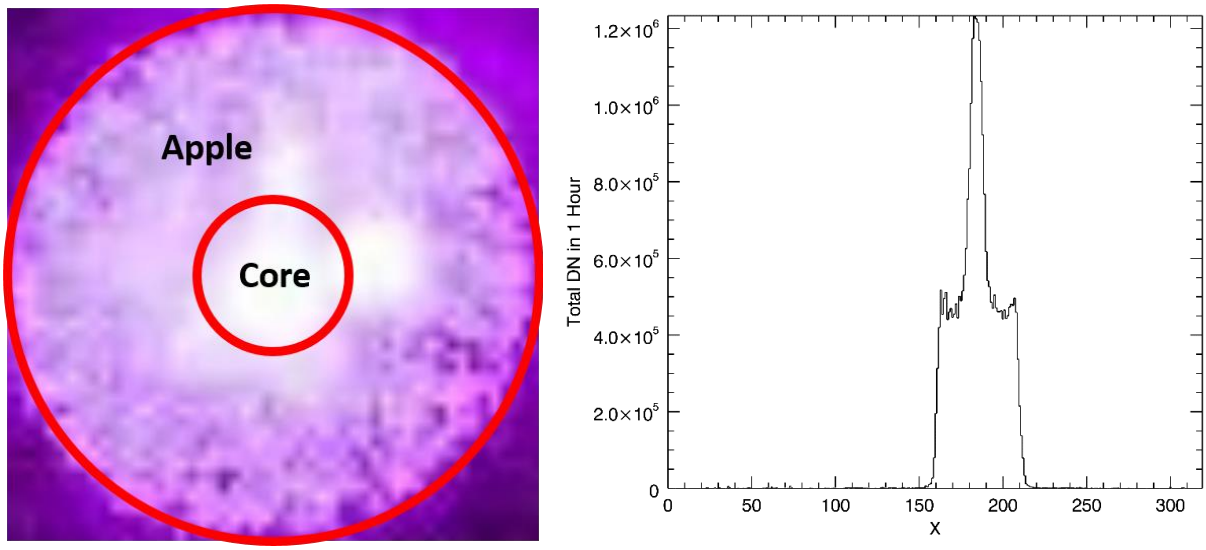

Figure 4.5. Definition of the APPLE masks (left): the core area is defined as a circular area with a radius of 5 pixels centered at the brightest pixel of the low-noise image and the apple area is the outer ring defined by a radius of 25 pixels. When the X2.3 flare erupted, hard X-ray penetration occurred and resulted in the high DN values in the ring area (right).

A pair of SAM images, taken ten seconds apart, is first compared pixel by pixel. The minimum of the pixel values forms a 20-second image to eliminate presence of particles. The median of five 20-second image pairs at each pixel forms a low-noise image which is used to estimate locations of the active regions. This is under the assumption that the active regions contributes to the persistently bright spots on the solar disk. The pair-wise technique is similar to the three-pair median performed by Hock et al. [2013] and is intended to obtain lower-noise images. During hard X-ray penetration, the enlarged circular feature has a radius about 25 pixels and the saturated pinhole area projects to an area of a radius about 5 pixels. The area around the brightest pixel of a lower-noise image is considered the location of the most active area of solar atmosphere during the 100 seconds. The second active area is only considered as the brightest pixel whose brightness reaches at least 70% of that of the first active area and which is located outside the circle of radius of 25 pixels centered the first peak. Locations of the two most active areas are obtained every 10 seconds with the span of 100 seconds centered at the current frame of processing. Note that so far the term 'active area' is used instead of the conventional 'active region.' This is because the detected active areas from every 10-second image may not necessarily belong to active regions and vary across the solar disk as shown in Figure 4.6 even the great care has been taken to reduce the noise on the images. After locations for over 8,000 images are obtained in one day, the two highest populated locations are recognized as active regions.

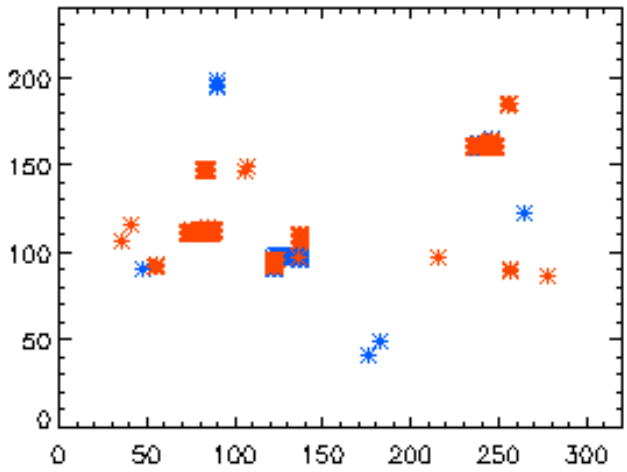

Figure 4.6. A map shows the locations of two most active pixels of each image on the CCD within one day.

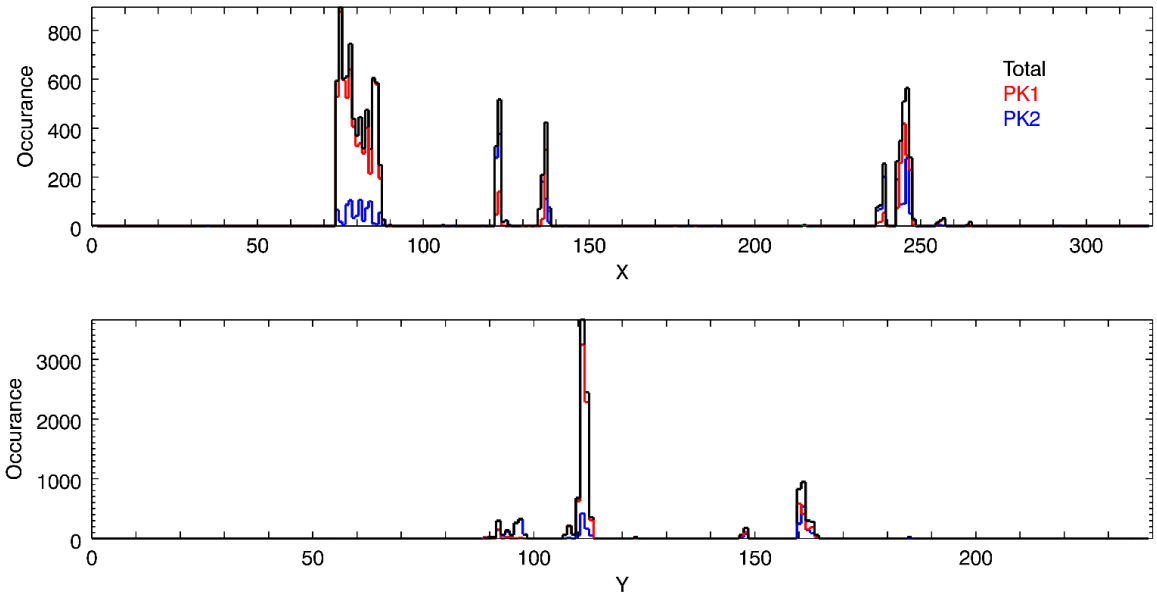

Figure 4.7. Histograms of the X and Y coordinates of two most active areas of 10-second images reveals the areas where most of the highly energetic photons are from. Before alignment, the PK1 curve captures the most active area of each image and the PK2 curve locates the secondary active area. The Y coordinates tend to group closer than the X coordinates.

Figure 4.6 shows a map of the locations of two most active pixels of each 10-second image on the CCD in the X and Y coordinates within one day. The histograms of the X and Y coordinates

of these active regions are obtained and stacked as shown in Figure 4.7. Since the Y coordinates group closer than the X coordinates, the algorithm searches for the greatest population from the histogram of the Y coordinate and its corresponding X coordinates to determine the location of the first active region. This population is then removed from the histograms. The second greatest population is detected the same way as the first one and determines the location of the second active region. Figures 4.8-4.10 show the progression of the daily-mean locations of the two most active regions from 2011 to 2014. As the Sun rotates, the X coordinate varies from ~60 to ~270. As the Earth orbits around the Sun, Y coordinates fluctuates due to Earth's inclined orbit with respect to Sun's equator. The fluctuation in Y due to Earth's orbit around the sun is modeled and corrected from Figures 4.8-10. However, the effect of SDO's geosynchronous orbit around the Earth has not yet been estimated. The trend of active regions in the solar atmosphere converging toward the Sun's equator can be observed in Figure 4.11, which is similar to the famously known butterfly diagram [Hathaway, 2010]. By following two most populated active regions using this technique, we implicitly expect solar flares and hard X-ray penetrations are likely to happen in these bright parts of the solar atmosphere.

The APPLE algorithm records the brightness (total DN) within the circular masked areas of both core and apple. The brightest two pixels are not always the same ones throughout the day. They may take places of each other but other locations have taken their places as shown in Figure 4.6. Careful alignment is performed to create light curves of two active regions. Figure 4.12 shows the integrated DN of two active regions on Feb 15, 2011 and Apr 29, 2014. On Apr 29, 2014, the active region, AR2, where a B9.7 flare took off does not result in high-intensity pixels on the CCD most of the time. On the contrary, when a X2.3 flare erupted on Feb 15, 2011, no elements on the

solar disk had a brightness that reached 70% of the brightness maintained by the flaring region about two third of the day.

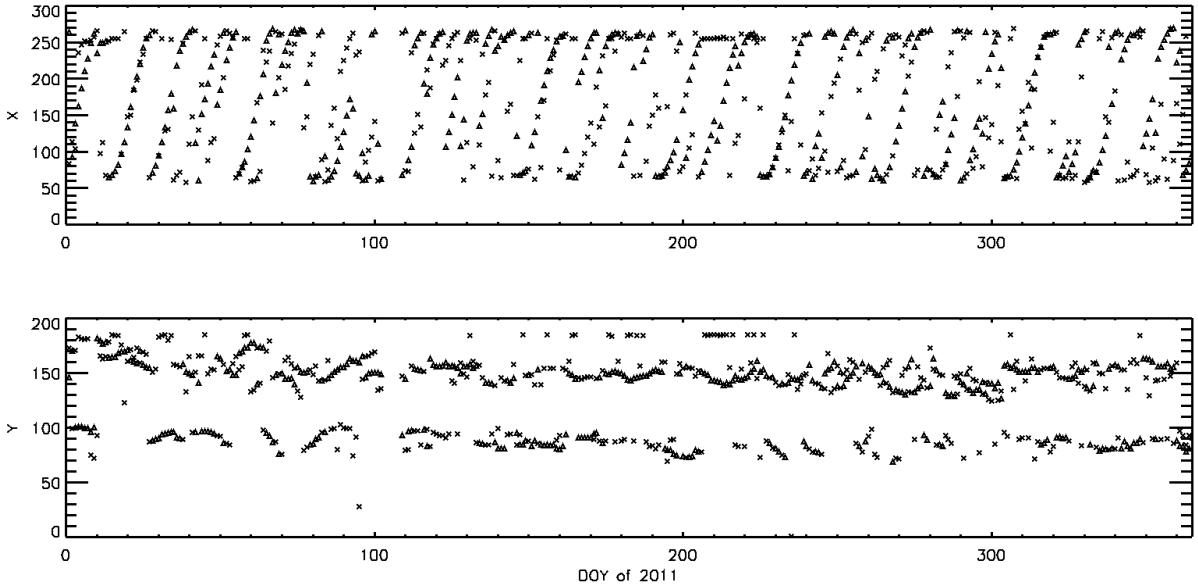

Figure 4.8. Daily-mean locations in CCD coordinates of the two most active regions in 2011.

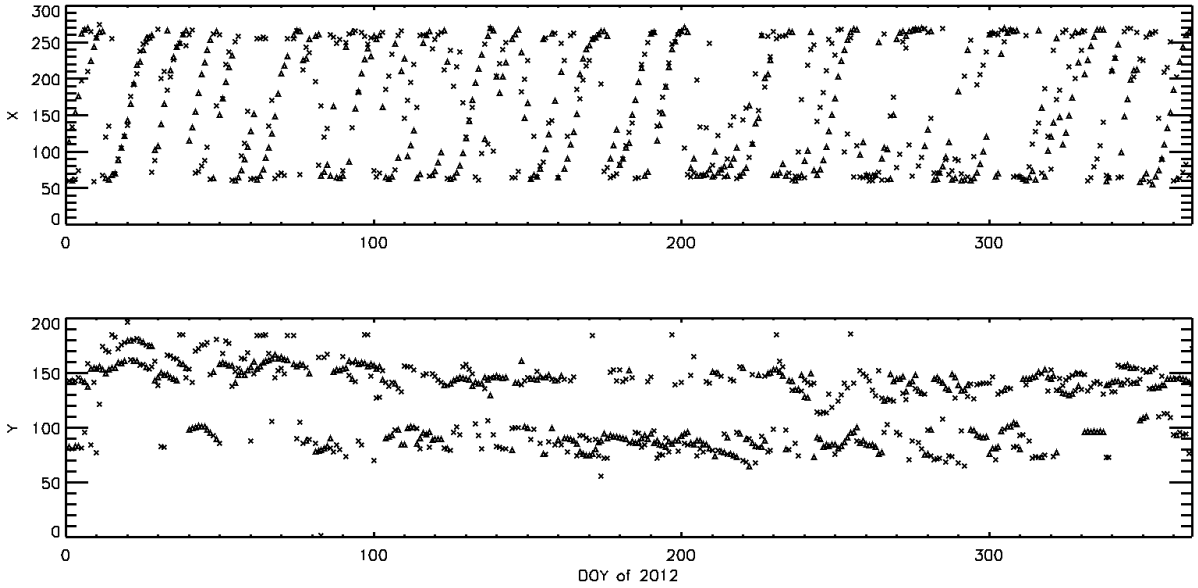

Figure 4.9. Daily-mean locations in CCD coordinates of the two most active regions in 2012.

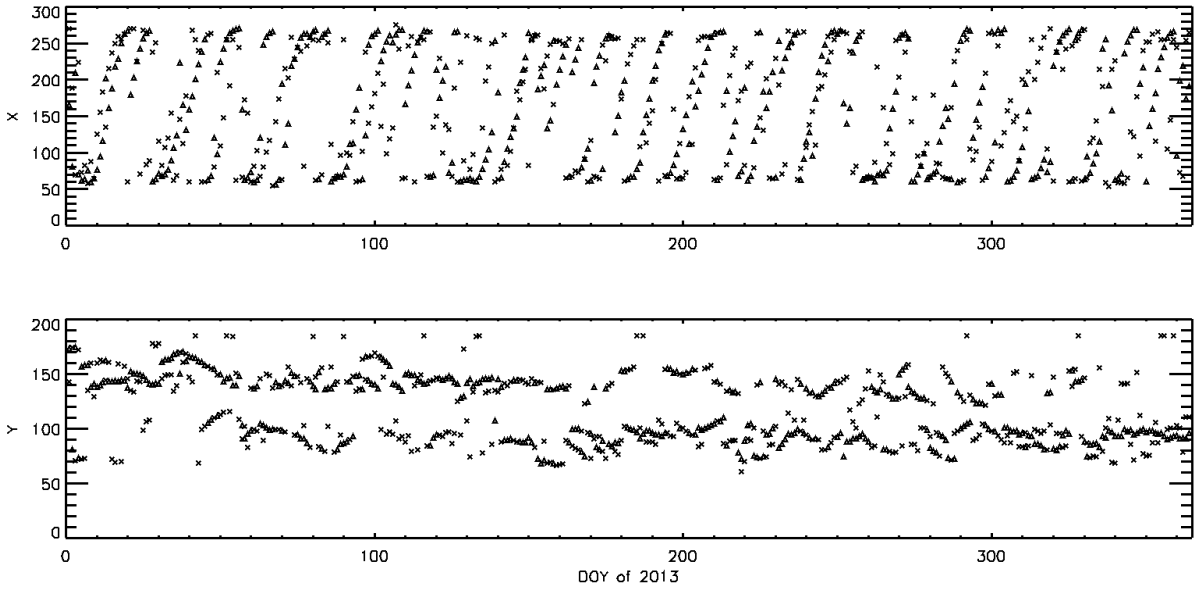

Figure 4.10. Daily-mean locations in CCD coordinates of the two most active regions in 2013.

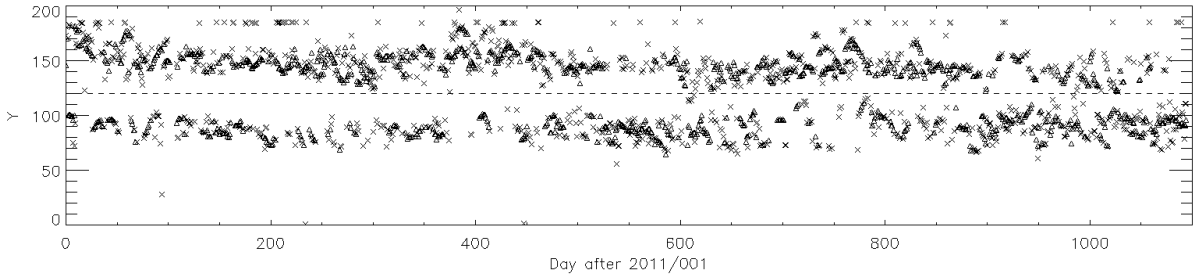

Figure 4.11. The Y coordinates of the active regions appear to converge toward Sun's equator from 2011 to 2013. Sun's equator is at around 120 (dish).

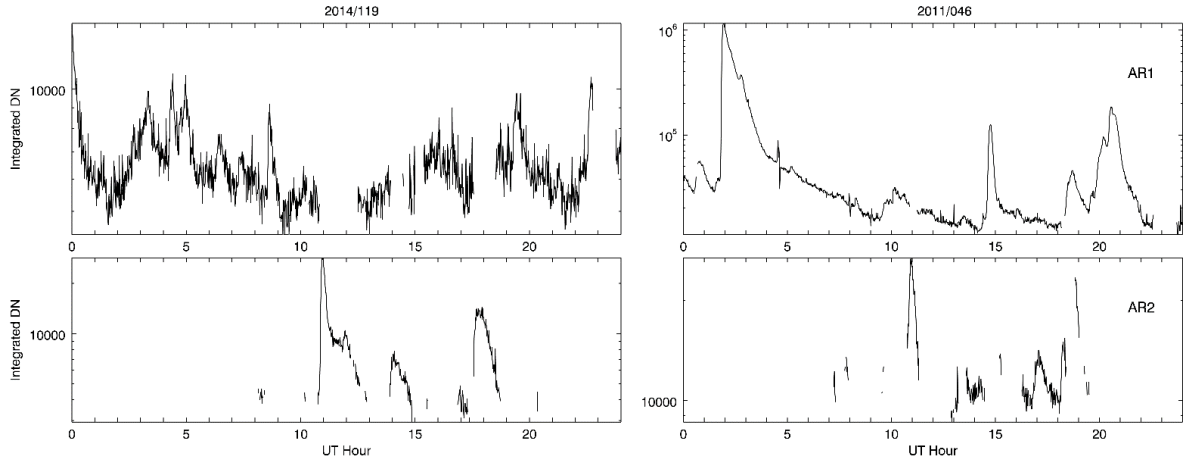

Figure 4.12. Alignment of the active regions reveals the evolution of the light curves on two flaring days. The left panels belong to two active regions on Apr 29 (day 119), 2014 and. A X2.3 flare took off on Feb 15 (day 046), 2011 (right). On a relatively quieter day, the active region, AR2, where the strongest flare of the day took off does not result in high-intensity pixels on the CCD most of the time.

4.6 Photon Events and Recreation of High Resolution Solar Images

The techniques discussed in the previous sections facilitate the PED algorithm, which is currently implemented following the following steps. First, it looks up the BB results for the solar activity level to determine if the APPLE AR circular masks are needed. Secondly, if the APPLE AR filters are required, it utilizes the information to preserve particles inside the masked areas but performs regular particle filtering outside of them. This way the highly energetic photons in the vicinity of flaring active regions that are previously discarded are now registered properly. A photon list is created every minute and contains all the extracted photons which are registered with their centroid location, total DN, size, and time of presence. There are about 1,000 photon events detected on each 10-second image on an active day and 700 events on a quiet day. Having locations of the energy centroids recorded permits the recreation of higher-resolution solar images from the original 200x200 images. A procedure plants photons from photon lists to an image of new dimensions as well as a map of the number of photons populating each individual pixel. The

population map provides customizable options for displaying images, such as 1) screening low-populated pixels to eliminate particles or noisy pixels in high-energy channel and 2) filtering out high-populated pixels to remove persistent features from such as out-of-band photons in low-energy channel. Depending on the applications, the population map serves as an indicator for the particular day and should be used with care. In general, the higher resolution of an image to be re-created, the lower threshold for population should be set since photons are farther apart; the longer the period of observation, the higher threshold may be set. Examples of displaying the PED results are shown in Figure 4.13, each of which is nine times greater than its original size. Photons are categorized into three channels by their total DN. The *long*-wavelength (low-energy) channel shown in gray scale contains photon events of 20-100 DN. The persistent presence of out-of-band (> 7nm) photons result in these low-energy photons being detected together as one event when pileup occurs and having energy falling within the DN range. The bright spectral line in the middle of the image is the higher-order grating of the 30.4 nm emission. Limb brightening outlines the circumference of the Sun. Coronal holes, dim and cooler features in the solar atmosphere where open field lines origin, are visible in this channel. The *mid*-wavelength (mid-energy) channel in green contains events of 100-700 DN. The *short*-wavelength channel in red is the most energetic channel. It contains events greater than 700 DN and therefore able to capture intensive irradiance increase during flares and hard X-ray penetration through the filter.

An automated solar image viewer is designed to saturate the brightest 10% pixels in order to display images regardless solar activity level. Images at the left column belong to May 15, 2010, which is one of the quietest days during the SDO operation. Not only is the high end of the color bar has a low value, its short-channel has few bright pixels that are noisy-like. Other than the two

active regions spreading out at the eastern and western limbs, the Sun appears to be quiet in the middle channel as well. Two X-class flares are shown in the middle and right column of Figure 4.13: an X2.3 flare on Feb 15, 2011 and a X1.3 flare on Apr 25, 2014. Both flares erupted at early UT hours and later several minor flares occurs from the same active regions. The X2.3 flare appears to have 6.5 times lower total energy output in the mid channel than the X1.3 flare but 1.6 times greater in the short channel. Its high-DN events are more concentrated at the two major active regions. Therefore, even though hard X-ray penetration occurs on both short-channel images, it is more visible in the X1.3 case because of the lower contrast among pixels. The east-west elongated features are due to the fact that all the photons in one entire day are included in these images.

The Atmospheric Imaging Assembly (AIA) is a suite of solar EUV imagers on SDO. Its high-resolution images are shown in Figure 4.14, where different solar features are visible at 304 Å (top), 193 Å (middle), and 171 Å (bottom) [The Sun Today, 2014] and serve as reference for what is observed in the SAM images. Three columns are corresponding to those in Figure 4.13.

On a quad-core personal computer with 8 GB of RAM, averagely it takes about 6 minutes to complete the PED run for one-hour data and about 2.5 hours on 8,000+ images for one day. The BB and APPLE procedures both take only about 5% of the PED process time. Overall, it is fairly manageable for a modern PC to analyze the SAM images and retrieve soft X-ray broadband irradiance and photon lists.

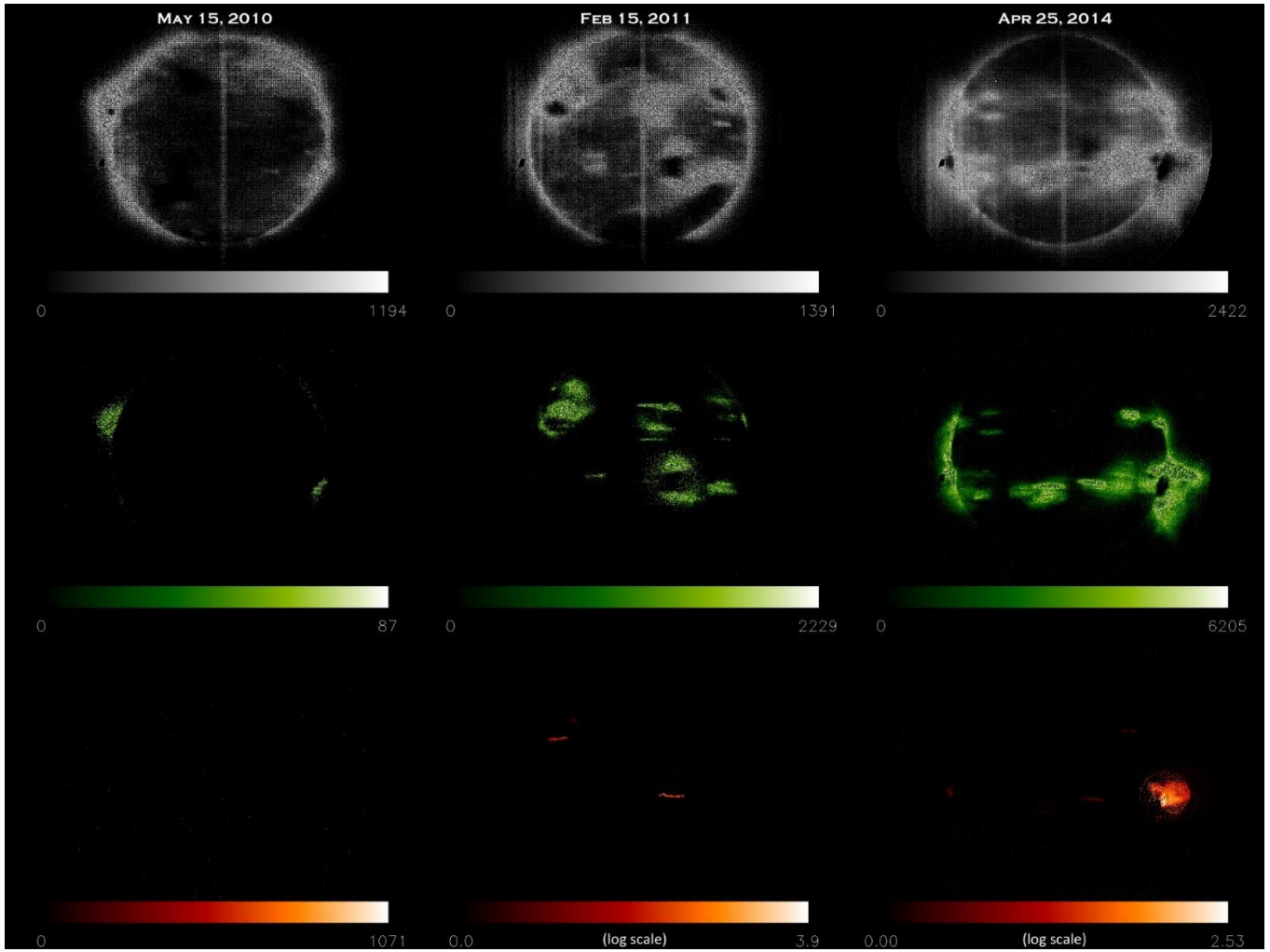

Figure 4.13. The PED photon lists enable recreation of high. Each image is nine times larger than the original image. The color bars are automatically set to saturate the brightest 10% pixels. Photons are categorized into three channels: long (gray), mid (green), and short (red). May 15, 2010 (left) is one of the quietest days during the SDO operation. Two X-class flares are also shown: an X2.3 flare on Feb 15, 2011 (middle) and a X1.3 flare on Apr 25, 2014 (right). In long channel, the bright spectral line in the middle comes from the higher-order grating of the 30.4 nm emission. Limb brightening outlines the circumference of the Sun. Coronal holes, dim and cooler features in the solar atmosphere where open field lines origin, are visible in this channel. Most of the active regions features appear in the mid channel. The short channel is able to capture intensive irradiance and hard X-ray penetration through the filter during flares.

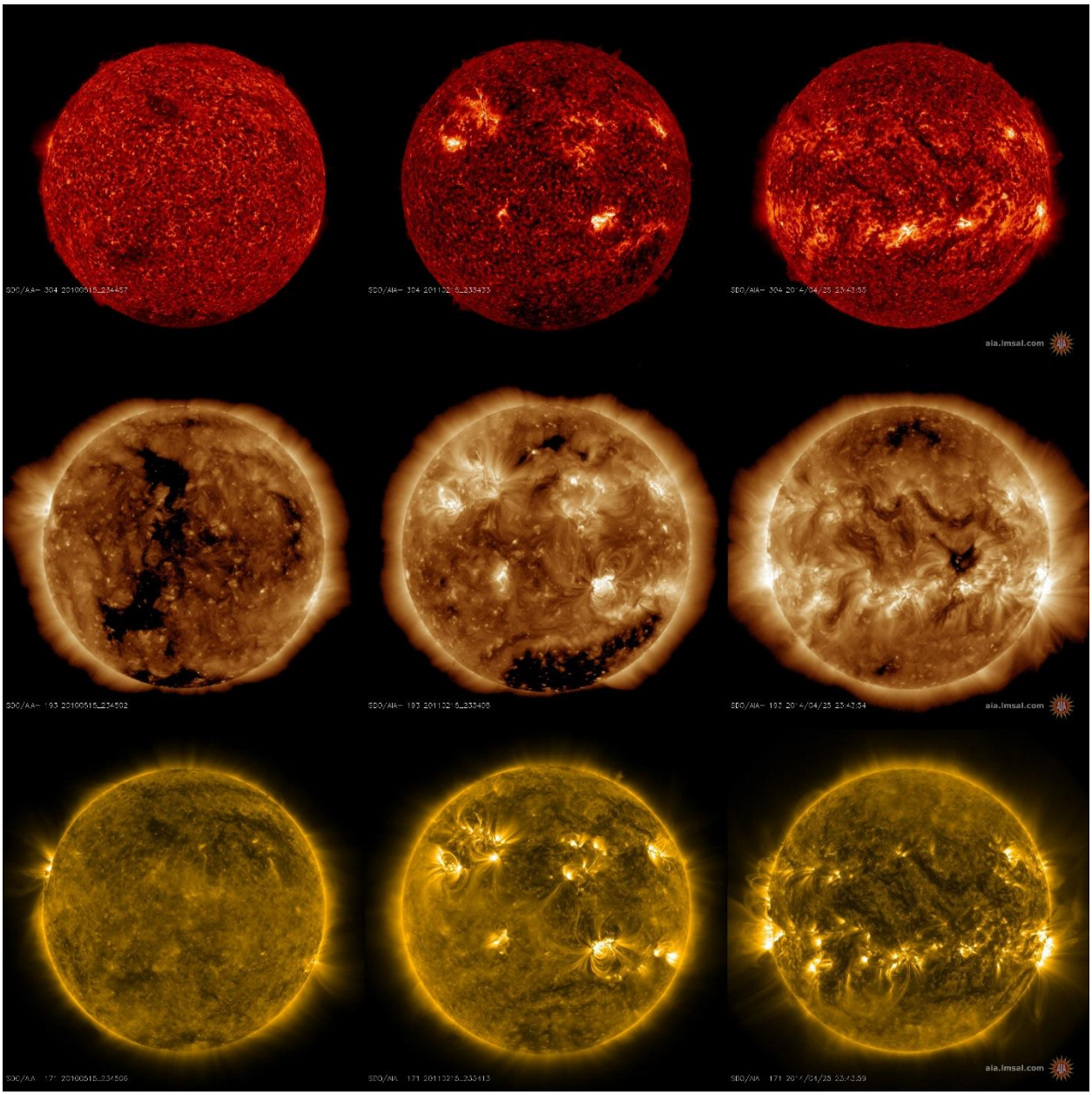

Figure 4.14. The Atmospheric Imaging Assembly (AIA) is a suite of solar EUV imagers on SDO. Channels at 304 Å (top), 193 Å (middle), and 171 Å (bottom) [Lockheed Martin Solar and Astrophysics Laboratory, The Sun Today].Three columns are corresponding to three dates as in Figure 4.13.

4.7 Spectral Irradiance

The development of the BB and PED algorithms facilitate the ultimate goal of the SAM images – to obtain spectral irradiance of the Sun at soft X-ray wavelengths. Energy of a photon, E, is associated with the frequency, ν, that it is emitted and related by the Planck-Einstein relation in Equation 4.1a. Given that energy is in eV and wavelength, λ, in nanometer, Equation 4.1a can be rewritten in a convenient form as Equation 4.1b.

$$E = h\nu \tag{4.1a}$$

$$E\ [eV] = \frac{1239.84\ [eV \cdot nm]}{\lambda\ [nm]} \tag{4.1b}$$

When a photon event is recognized and extracted form an image, the question following is: should one interpret a photon event of 1 keV as one photon of 10 keV or four of 250 eV each? The former suggests one photon at 1.2 nm while the latter suggests four photons at 5.0 nm. On the other hand, ambiguity of mistreating photons as particles or vice versa exists especially when photon pileups occur. Pileup in a CCD occurs when two or more photons coincide and a CCD element is incapable of resolving them temporally or spatially [Ballet, 1999; Davis 2001]. An example of photon pileups leading to a lower event rate which in turn results in distortion of the observed spectrum is presented in Davis' work [2001]. Failing to properly characterizing the detected events may lead to wrong interpretation of the mechanism behind the measurements as the relative spectral variability at soft X-ray wavelengths is important for understanding evolution of different features in the solar atmosphere [Chamberlin et al., 2012; Inglis and Gilbert, 2013]. Applying more sophisticated screening filters may slightly improve particle removal but risks losing more irradiance by accidentally removing more in-band photons. Further improvement of machine learning for a great amount of tiny objects across several pixels can be computational costly but

yet ineffective because ambiguity still exists when photons pile up at a small number of pixels or are close enough to be detected as one big event. A possible characteristic of photon pileups is large-size events as examples shown in Figure 4.4. and however the impact area of an energetic photon on Treatments of these issues are highly subject to the nature of the measurements, such as type of the object and integration time, and need to adapt to the specific data sets [Ballet, 1999; Davis 2001]. A preliminary statistical approach based on simulation is proposed here to obtain spectral irradiance from the SAM images.

The simulation aims to create a 320x240 image DN histogram that is close to those of the observations as in Figure 3.4 and to statistically quantify photon pileups. Irradiance between 0.1-7 nm in unit of watts per square meter observed during the Solar Irradiance Reference Spectra (SIRS) for the 2008 Whole Heliosphere Interval (WHI) [Chamberlin et al., 2008; Woods et al., 2009] is weighted by the SAM response function to create a reference reservoir of photons. The number of photons, N_{ptn}, is a function of wavelength, λ, and determined by Equation 4.2 for 10-second, SAM image.

$$N_{ptn}(\lambda) = \frac{I(\lambda) \cdot A \cdot T}{E_{ptn}(\lambda)} = \frac{6.25 \times 10^{19}}{1239.84} \cdot \lambda = 5.05 \times 10^{16} \cdot \lambda \tag{4.2}$$

where I is spectral irradiance in watts per square meter from the reference spectrum, A is the detector area, T is the integration time, and E_{ptn} is energy of a photon as a function of wavelength. Each photon in the reservoir is injected onto a random location on the simulation image. A photon does not have a physical size. Instead while reaching the detector it creates charge cloud within the CCD. It is expected that energy of a photon is shared by multiple pixels if it strikes close to an edge or a corner of a pixel [Tsunemi et al., 1999]. In the simulation a photon impact area is

characterized by a Gaussian distribution with certain full-width-at-half-maximum (FWHM). Nine FWHM cases are simulated with a fixed FWHM, from 0.1 to 0.9 pixel stepping every 0.1 pixel. In each case, all the photons contribute to equal area on the CCD. A scenario in which photons are with randomly varying FWHM is also carried out. Figure 4.15 shows the normalized DN histograms of the simulation results. For the fixed-FWHM cases, a greater impact area characterized by a wider FWHM leads to more low-DN population and fewer high-DN population. Among all the simulated cases, the varying-FWHM histogram is closest to the observation. Its histogram is lower than the observation between 20-30 DN but higher between 30-100 DN. The cause of this discrepancy is believed to be that out-of-bands contamination is not yet removed from the observation and not simulated in the simulation.

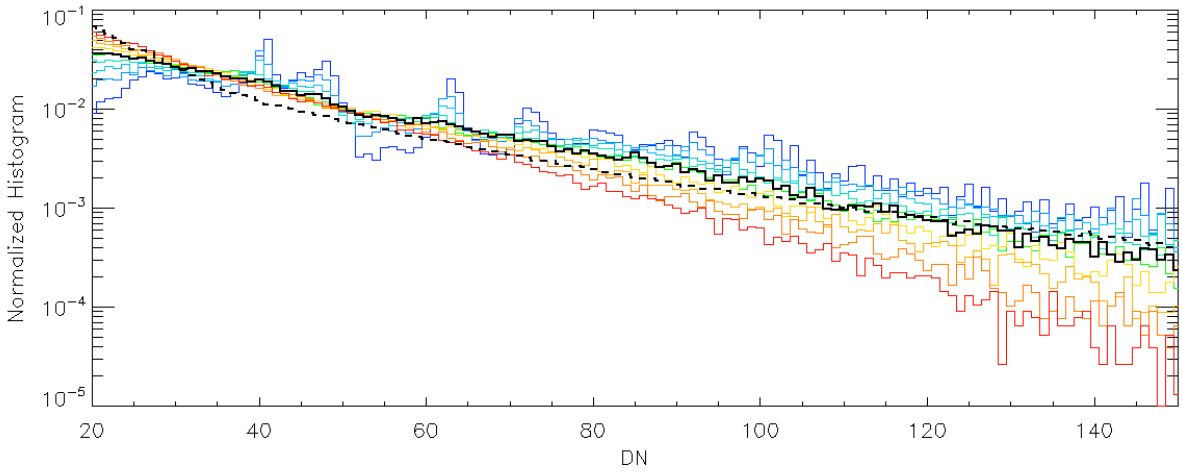

Figure 4.15. Normalized DN histograms of the simulation images result from made-up photons with fixed (color) and randomly varying (black solid) full-width-at-half-maximum (FWHM) of the impact areas. Nine fixed FWHM scenarios are simulated, with FWHM from 0.1 (blue) to 0.9 (red) pixels increasing 0.1 pixel at a time. Normalized DN histogram of the SAM measurements is also shown (black dash).

The agreement between the simulation and observation histograms is a good start. In the simulation, the locations that photons are injected on are generated by a random number generator. More simulation images should be created with a greater group of seeds. Further including limb brightening by purposely placing more photons around the Sun's circumference should also be included for more realistic simulation. The PED algorithm can then be applied to these simulation images. Size, shape, and total DN of the extracted photon events should be investigated. Statistically meaningful behavior of photon pileups and uncertainties of separating photons and particles may be better determined from the difference between the extracted and original spectra.

Beside the simulation result, the PED algorithm is also performed on the dark image (Figure 3.3). A probability distribution is obtained via the events that are extracted from dark and passing filters as photons to indicate the likelihood random data counts forming photon-like features. A dark spectrum resulting from unanticipated contamination can be defined as the probability distribution multiplied by total number of photon events in light and subtracted from the light spectrum.

4.8 Summary and Conclusions

The development of the PED algorithm on the SAM images is reviewed in this chapter. Two methods are presented for event detection. Defining events by monotonically decreasing edges often leaves out off-axis pixels and includes partial energy from photons. Algorithm based on the nearest neighbor search extracts events of any shape and enables filtering particles by their spatial characteristics. Standard deviation of the active component, from the BB results, informs

the PED procedure if the current date of analysis is an active day. APPLE provides the active region information for PED to ensure proper registration of the AR photons. PED extracts events, separates photons from particles, and makes photon lists. Higher-resolution images are demonstrated possible with the extracted SAM photons. Though efforts were made to eliminate particle contamination, photon pileups occur inevitably at active regions, at limb brightening, and due to persistent out-of-band spectral lines. These further add ambiguity to distinguishing in-band photons from particles. Simulation is carried out to address photon pileups and to assist conversion from photon events to spectral irradiance. On the other hand, as in the BB approach, PED is performed on both light and dark images. The dark spectrum resulting from unanticipated contamination can then be subtracted from the light spectrum.

References

Arya, S., D. M. Mount, N. S. Netanyahu, R. Silverman, and A. Y. Wu, "An optimal algorithm for approximate nearest neighbor searching in fixed dimensions," Jour. of ACM, 45, 1998

Aschwanden, M. J., "2D Feature Recognition and 3D Reconstruction in Solar EUV Images," Solar Phys., 2005

Ballet J., "Pile-up on X-ray CCD instruments," Astron. Astrophys. Suppl. Ser., 135, 1999

Canny, J., "A Computational Approach to Edge Detection," IEEE Transactions on Pattern Analysis and Machine Intelligence, PAMI-8, 6, 1986

Cerruti A. P., P. M. Kintner Jr., D. E. Gary, A. J. Mannucci, R. F. Meyer, P. Doherty, and A. J. Coster, "Effect of intense December 2006 solar radio bursts on GPS receivers," Space Weather, 6, 2008

Chen Z., Y. Gao, and Z. Liu, "Evaluation of solar radio bursts effect on GPS receiver signal tracking within International GPS Service network," Radio Science, 40, 2005

Chamberlin, P. C., R. O. Milligan, and T. N. Woods, "Thermal evolution and radiative output of solar flares observed by the EUV Variability Experiment," Solar Phys., 2012

Cliver E. W., “Solar flare nomenclature,” Solar Physics, 157, 1995

Davis, J. E., “Event pileup in charge-coupled devices,” The Astrophysical Journal, 2001

Fayyad U. M., “Data mining and knowledge discovery in databases: applications in astronomy and planetary science,” AAAI-96 Proceedings, 1996

Fletcher, L., B.R. Dennis, H.S. Hudson, S. Krucker, K. Phillips, A. Veronig, M. Battaglia, L. Bone, A. Caspi, Q. Chen, P. Gallagher, P.T. Grigis, H. Ji, W. Liu, R.O. Milligan, and M. Temmer, “An observational overview of solar flares,” Space Science Review, 159, 2011

Hathaway, D. H., “The solar cycle,” Living Rev. Solar Phys., 7, 2010

Hock R. A., D. Woodraska, and T. N. Woods, “Using SDO EVE data as a proxy for GOES XRS B 1–8 angstrom,” Space Weather, 11, 2013

Inglis, A. R. and H. R. Gilbert, “Hard X-ray and ultraviolet emission during the 2011 June 7 solar flare,” The Astrophysical Journal, 777, 2013

Lites, B. W., “Magnetic flux ropes in the solar photosphere the vector magnetic field under active region filaments,” The Astrophysical Journal, 2005

Liu K., J. Zhang, Y. Wang, and X. Cheng, “On the origin of the extreme-ultraviolet late phase of solar flares,” The Astrophysical Journal, 150, 2013

Lockheed Martin Solar and Astrophysics Laboratory, The Sun Today, http://sdowww.lmsal.com/suntoday/, Jul, 2014

Nitta N. V. and H. S. Hudson, “Recurrent flare/CME events from an emerging flux region,” Geophys. Res. Lett., 28, 2001

Teske, R. G. and E. B. Mayfield, “Thermodynamic history of a solar active region observed in X-rays,” The Astrophysical Journal, 1976

Tian, L. and D. Alexander, “Role of sunspot and sunspot-group rotation in driving sigmoidal active region eruptions,” Solar Phys., 2006

Tsunemi, H., J. Hiraga, K., Yoshita, and K. Hayashida, “Measurement of the charge cloud shape produced by an X-ray photon inside the CCD using a mesh experiment,” Nuclear Instruments and Methods in Physics Research, 421, 1999

Woods, T. N., P. C. Chamberlin, J. W. Harder, R. A. Hock, M. Snow, F. G. Eparvier, J. Fontenla, W. E. McClintock, and E. C. Richard, “Solar Irradiance Reference Spectra (SIRS) for the 2008 Whole Heliosphere Interval (WHI),” Geophysical Research Letters, Vol. 36, 2009

CHAPTER 5 Summary and Conclusions

Solar soft X-ray and EUV irradiance drives variability of ionized and neutral species in the ionospheric and thermospheric system. As a result, the response of terrestrial atmosphere corresponds to solar cycles and solar activities on the Earth-facing side. Absorbed mostly at 100-150 km, soft X-ray irradiance is crucial to lower thermospheric photochemical balance [Solomon et al., 2005]. NO has the lowest ionization potential and NO^+, the terminal ion, dominates the electron density in the E-region of the ionosphere. NO also serves as one of the major cooling mechanisms. Therefore, its concentrations are indicative of energy deposition in the atmosphere.

The retrieval of NO abundance from level 0 limb scanned data sets in the lower thermosphere is demonstrated in Chapter 2 and the local-time variation between 120–150 km is derived from the retrieved vertical profiles. With the latest photochemistry updated in the NOx1D [Yonker, 2013], the comparison between the RAIDS measurements and the modeled densities shows good agreement within 50%. At 150 km, NO density increases as soon as the tangential points viewed from the spacecraft entering the sunlit hemisphere. At 120 km there is a delay of about 2 to 4 hours before an increase in NO abundance. The solar optically thin FUV radiation penetrates to and is absorbed at the lower altitudes at large solar zenith angles and leads to photodissociation of NO after sunrise. Going toward noon, the decrease of solar zenith angle allows the optically thick solar XUV irradiance to deposit at the lower altitude where it rapidly produces $N(^2D)$ and NO. The production due to XUV reaches its maximum from around local noon to 2 PM. As solar zenith angle starts increasing, the NO production and its abundance decreases in the afternoon.

Though soft X-ray irradiance is critical to all the constituents in both ionosphere and the thermosphere and is key to driving various atmospheric models, it is not yet well known. Great uncertainties exist among all the existing solar measurements in these wavelengths. As a pinhole camera, SAM projects solar disk in soft X-ray wavelengths to a dim corner of the MEGS-A CCD. The original idea of obtaining spectra became challenging as contamination from out-of-band photons and particles overwhelms the solar signal. While one minute of dark measurement a day is insufficient for the full-day calibration, several techniques have been developed and presented in this dissertation to address these issues.

In the BB approach, the difference between light and dark histograms is divided into fifteen narrow bands. The shorter-wavelength bands have high correlation with the GOES irradiance while the longer-wavelength bands correlates better with F10.7. The variability of the shorter-wavelength bands dominates that of the broadband irradiance. In the one-component method bands 1–6 at the highest-energy end are selected to represent the variability of the particle term and in addition bands 6–8 are selected to characterize the active component in the two-component method. The inclusion of band 6 in both active and particle terms allows it to contribute as a particle channel but preserve its accountability for solar photons during flares. The amount of particle contribution to be removed from broadband irradiance is estimated by obtaining maximal correlation between the solar components (the quiet component in two-component case) and F10.7 and by reserving their products with the coefficients *A* and *B*. It has been shown that the one-component (two-component) method provides better broadband estimate at lower (higher) activities. A hybrid method is therefore adopted that the one-component estimate is generally provided but the two-component estimate is employed when certain condition indicating possible flaring is reached. For

the first four years of the SDO operation from 2010 to 2013 the ratio of the SAM to ESP irradiance has a mean of 1.07 and a standard deviation of 0.28. The goal is to use these coefficients and criteria established based on a good amount of samples so that future broadband irradiance may be obtained solely from the SAM images without any proxy or prior information from other measurements. These coefficients and criteria are tested to the 2014 images and the results show the procedure has successfully identified the flaring days and properly applies a better set of the coefficients for irradiance estimate. The 2014 reported broadband irradiance is within 25% of agreement with ESP. About 35,000 hours of broadband irradiance are reported by the BB procedures from 2010 to 2014 and the mean of its ratio to ESP is close to unity. The agreement is encouraging compared to the early discrepancies among solar soft X-ray measurements. Clearly SAM is a valid soft X-ray monitor.

PED is pursued as the next step toward spectral irradiance and its procedures are outlined in Figure 4.2. Two techniques are developed for event detection: one defining events by monochromatically decreasing edges and one adopting the concept of nearest neighbor search. The former approach often leaves out off-axis pixels and includes partial energy from photons; the latter extracts events of any shape and enables filtering particles by their spatial characteristics. The filtering rules separating photons from particles are based on studies of the particle appearance on the raw images. Each of the four rules tabulated in Table 4.1 is customizable to be switched on or off upon running the PED algorithm. Applying all of the rules often results in missing 50% photons at around active regions; if otherwise, it often leaves a noisier background. This suggests that rules are to be adopted differently depending on where events are detected such as looser rules at active regions and more strict rules for quiet atmosphere.

APPLE is a separate procedure for studying the evolution of irradiance in up to two active regions starting by tracking the two brightest separated pixels from image to image. It creates two masks with radii of 5 and 25 pixels respectively around the brightest pixels and tracks the total DN in the masked areas for each image. Though locations of two brightest pixels may change during the day, alignment is performed on results from over 8,000 images and provides locations of two active regions every day.

An automated system is set up so that from data reduction to final data product is performed every day. The SAM images are truncated down to the size as in Figure 3.3 at the LASP server and transferred back to the Space@VT server. As soon as the local server received the data sets, the BB and APPLE algorithms are performed in parallel. Standard deviation of the active component, from the BB results, informs the PED procedure if the current date of analysis is an active day. If the chance for flares is high, APPLE provides the active region information for PED to ensure proper registration of the AR photons. PED extracts events, separates photons from particles, and creates photon lists. Higher-resolution images are demonstrated possible with the extracted SAM photons. On a quad-core personal computer with 8 GB of RAM, averagely it takes about 6 minutes to complete the PED run for one-hour data and about 2.5 hours on 8,000+ images for one day. The BB and APPLE procedures both take only about 5% of the PED process time. Overall, it is fairly manageable for a modern PC to analyze the SAM images and retrieve soft X-ray broadband irradiance and photon lists.

Though efforts were made to eliminate particle contamination, photon pileups occur inevitably at active regions, at limb brightening, and due to persistent out-of-band spectral lines.

These further add ambiguity to distinguishing in-band photons from particles. Simulation is carried out to address photon pileups and to assist conversion from photon events to spectral irradiance. The agreement between the simulation and observation histograms is a good start. More simulation should be performed to include a greater group of random number seeds and limb brightening. The PED algorithm can then be applied to these simulation images. Size, shape, and total DN of the extracted photon events should be investigated. Statistically meaningful behavior of photon pileups and uncertainties of separating photons and particles may be better determined from the difference between the extracted and original spectra. Beside the simulation result, the PED algorithm is also performed on the dark image (Figure 3.3). A probability distribution is obtained via the events that are extracted from dark and passing filters as photons to indicate the likelihood random data counts forming photon-like features. A dark spectrum resulting from unanticipated contamination can be defined as the probability distribution multiplied by total number of photon events in light and subtracted from the light spectrum. Though primary spectral results was once obtained utilizing the methods discussed at the end of Chapter 4, satisfying solar soft X-ray spectral irradiance between 0.1–7 nm was not yet reached and is still left as an active project.

On May 27, 2014, the failure of a capacitor on the MEGS-A CCD resulted in discontinuity in the data production of the MEGS-A and SAM channels on EVE and no more SAM images can be obtained to this date the dissertation is completed. Regardless of this unfortunate incident, SAM has provided the solar and aeronomy communities great assets for more than five years. Its data sets will continue improving our understanding of the Sun and its coupling to the terrestrial atmosphere.

References

Solomon S. C. and L. Qian, “Solar extreme-ultraviolet irradiance for general circulation models,” Journal of Geophysical Research, Vol. 110, 2005

Yonker, J. D., “Contribution of the First Electronically Excited State of Molecular Nitrogen to Thermospheric Nitric Oxide,” PhD dissertation, 2013